



Universidade Estadual de Campinas  
Instituto de Física "Gleb Wataghin"

Gabriela Vitti Stenico

NEUTRINO PHENOMENOLOGY IN  
SHORT-BASELINE EXPERIMENTS

FENOMENOLOGIA DE NEUTRINOS EM  
EXPERIMENTOS DE *SHORT-BASELINE*

CAMPINAS  
2021

Gabriela Vitti Stenico

NEUTRINO PHENOMENOLOGY IN SHORT-BASELINE  
EXPERIMENTS

FENOMENOLOGIA DE NEUTRINOS EM EXPERIMENTOS  
DE *SHORT-BASELINE*

Tese apresentada ao Instituto de Física "Gleb Wataghin" da Universidade Estadual de Campinas como parte dos requisitos para a obtenção do título de Doutora em Ciências.

Thesis presented to the "Gleb Wataghin" Institute of Physics of the University of Campinas in partial fulfillment of the requirements for the degree of Doctor in Science.

**Advisor/Orientador: Prof. Dr. Orlando Luis Goulart Peres**  
**Co-supervisor/Coorientador: Prof. Dr. Ernesto Kemp**

Este exemplar corresponde à versão final da Tese defendida por Gabriela Vitti Stenico e orientada pelo Prof. Dr. Orlando Luis Goulart Peres.

CAMPINAS  
2021

Ficha catalográfica  
Universidade Estadual de Campinas  
Biblioteca do Instituto de Física Gleb Wataghin  
Lucimeire de Oliveira Silva da Rocha - CRB 8/9174

St42n Stenico, Gabriela Vitti, 1991-  
Neutrino phenomenology in short-baseline experiments / Gabriela Vitti  
Stenico. – Campinas, SP : [s.n.], 2021.

Orientador: Orlando Luís Goulart Peres.

Coorientador: Ernesto Kemp.

Tese (doutorado) – Universidade Estadual de Campinas, Instituto de Física  
Gleb Wataghin.

1. Oscilações de neutrinos. 2. Grandes dimensões extras. 3. Decaimento de  
neutrinos. I. Peres, Orlando Luís Goulart, 1969-. II. Kemp, Ernesto, 1965-. III.  
Universidade Estadual de Campinas. Instituto de Física Gleb Wataghin. IV.  
Título.

Informações para Biblioteca Digital

**Título em outro idioma:** Fenomenologia de neutrinos em experimentos de short-baseline

**Palavras-chave em inglês:**

Neutrinos oscillations

Large extra dimensions

Neutrino decay

**Área de concentração:** Física

**Titulação:** Doutora em Ciências

**Banca examinadora:**

Orlando Luís Goulart Peres [Orientador]

Alberto Martin Gago Medina

Célio Adrega de Moura Júnior

Pedro Cunha de Holanda

Ettore Segreto

**Data de defesa:** 24-05-2021

**Programa de Pós-Graduação:** Física

**Identificação e informações acadêmicas do(a) aluno(a)**

- ORCID do autor: <https://orcid.org/0000-0001-7821-4218>

- Currículo Lattes do autor: <http://lattes.cnpq.br/7294674213956674>



MEMBROS DA COMISSÃO JULGADORA DA TESE DE DOUTORADO DE GABRIELA VITTI STÊNICO – RA 150049 APRESENTADA E APROVADA AO INSTITUTO DE FÍSICA “GLEB WATAGHIN”, DA UNIVERSIDADE ESTADUAL DE CAMPINAS, EM 24 / 05 / 2021.

COMISSÃO JULGADORA:

- Prof. Dr. Orlando Luis Goulart Peres – Orientador – DRCC/IFGW/UNICAMP
- Prof. Dr. Alberto Martin Gago Medina – PUC – del Peru
- Prof. Dr. Célio Adrega de Moura Júnior – UFABC
- Prof. Dr. Pedro Cunha de Holanda - DRCC/IFGW/UNICAMP
- Prof. Dr. Ettore Segreto - DRCC/IFGW/UNICAMP

**OBS.:** Ata da defesa com as respectivas assinaturas dos membros encontra-se no SIGA/Sistema de Fluxo de Dissertação/Tese e na Secretaria do Programa da Unidade.

CAMPINAS

2021

# Dedication

To Davi, Gabriel, Clara, Mariana and Antônio. You are the future, make it bright!

*Have no fear of perfection;  
you will never reach it.*

(Marie Curie)

# Acknowledgements

This thesis could not be completed without the support and encouragement of my advisor, Orlando Peres. Prof., thank you for all the great ideas and all the possibilities to grow in my scientific career. I am incredibly grateful you have never lost your faith in me. You are a fantastic person and an extraordinary physicist!

I wish to thank André de Gouvêa for the valuable discussions while I was in Northwestern and Fermilab. I have learned a lot from you, Professor! Many thanks to Ernesto Kemp for introducing me to the amazing SBND Collaboration, where I could see up close how fantastic a neutrino experiment is. Also, I cannot express how grateful I am to Ornella Palamara for her leadership, encouragement, and for all the useful discussions about physics in SBND!

I am thankful to all my collaborators: David Vanegas, Suprabh Prakash, and Kevin Kelly, for the execution of exciting works! Thank you to my colleagues from SBND Collaboration: Vincent Basque, Dom Barker, Marco Del Tutto, and Mônica Nunes for helping me with LarSoft! I also wish to especially thank the GEFAN group in Brazil for the excellent meetings and discussions. I had a lot of fun with you, guys! Finally and most important: Pedro Pasquini, you are a spectacular physicist and an incredible person. Thank you for all the academic and emotional support during my Ph.D.!

Thank you, my family and friends (worldwide!), for the love and motivation you have always given to me. Those feelings were essential to keep me sane all these years. I owe this thesis to you!

I must express my gratitude to Professors and employees from the Universidade Estadual de Campinas (UNICAMP), which provided an excellent academic environment to develop my research and didactic skills. Many thanks to all of you!

Finally, I truly appreciate the financial support of the Fundação de Amparo à Pesquisa do Estado de São Paulo (FAPESP) funding Grant no. 2016/00272-9, no. 2017/12904-2 and no. 2014/19164-6, which allowed the execution of this Ph.D. The works were also financed in part by the Coordenação de Aperfeiçoamento de Pessoal de Nível Superior-Brasil (CAPES) - Finance Code 001 - and by the FAPEX funding grant 2925/19. To complete the acknowledgments of the vital financial support I have received during my Ph.D., I am grateful for the Fermilab-UNICAMP exchange agreement's partial support.

# Resumo

No contexto de oscilações de neutrinos e física de neutrinos, visamos estudar implicações fenomenológicas em experimentos de neutrinos produzidos em aceleradores e detectados a curta distância, de modo que a razão da distância percorrida pela energia do neutrino fique em torno de  $1 \text{ km/GeV}$  (ou  $1 \text{ m/MeV}$ ). Especificamente, escolhemos dois tópicos de trabalho: neutrinos em Grandes Dimensões Extras (LED) e decaimento de neutrinos pesados. Analisamos os efeitos do modelo LED no futuro experimento *Short-Baseline Neutrino Program*. Mostramos que o experimento tem sensibilidade competitiva à manifestação de dimensões extra e tem potencial de discriminar sinais da hipótese de LED daqueles do modelo  $3+1$ . Em se tratando de decaimento de neutrinos, mostramos que o modelo escolhido acomoda razoavelmente os resultados da chamada Anomalia do *Short-baseline*, conduzida pelos experimentos LSND e MiniBooNE, e evade vínculos fortes da busca pelo sinal de desaparecimento de neutrinos muônicos em experimentos com neutrinos de aceleradores detectados a curta distância.

**Palavras-chave:** grandes dimensões extras, decaimento de neutrinos, oscilação de neutrinos

# Abstract

In the context of neutrino oscillations and neutrino physics, we aimed to study phenomenological implications in short-baseline neutrino experiments. Specifically, we chose two work subjects: neutrinos in Large Extra Dimensions (LED) and heavy neutrino decay. We analyzed the effects of the LED model in the future Short-Baseline Neutrino Program experiment. We showed that the experiment has a competitive sensitivity to LED manifestation and can discriminate LED hypothesis from the  $3+1$  oscillation model. Regarding the studies with neutrino decay, we showed that the chosen model reasonably accommodates the short-baseline anomaly, led by LSND and MiniBooNE results, and evades strong constraints from muon neutrino disappearance searches in short-baseline.

**Key-words:** large extra dimensions, neutrino decay, neutrino oscillations

# Publication List

1. A. de Gouvêa, O. L. G. Peres, S. Prakash and G. V. Stenico, “On The Decaying-Sterile Neutrino Solution to the Electron (Anti)Neutrino Appearance Anomalies,” JHEP **07**, 141 (2020) doi:10.1007/JHEP07(2020)141 [arXiv:1911.01447 [hep-ph]];
2. A. De Gouvêa, K. J. Kelly, G. V. Stenico and P. Pasquini, “Physics with Beam Tau-Neutrino Appearance at DUNE,” Phys. Rev. D **100**, no.1, 016004 (2019) doi:10.1103/PhysRevD.100.016004 [arXiv:1904.07265 [hep-ph]];
3. G. V. Stenico, D. V. Forero and O. L. G. Peres, “A Short Travel for Neutrinos in Large Extra Dimensions,” JHEP **11**, 155 (2018) doi:10.1007/JHEP11(2018)155 [arXiv:1808.05450 [hep-ph]];

## **With Short-Baseline Near Detector (SBND) Collaboration:**

4. R. Acciarri *et al.* [SBND], “Cosmic Background Removal with Deep Neural Networks in SBND,” [arXiv:2012.01301 [physics.data-an]];
5. R. Acciarri *et al.* [SBND], “Construction of precision wire readout planes for the Short-Baseline Near Detector (SBND),” JINST **15**, no.06, P06033 (2020) doi:10.1088/1748-0221/15/06/P06033 [arXiv:2002.08424 [physics.ins-det]].

# List of Figures

1.1	The elementary particles of the Standard Model. . . . .	18
1.2	Feynman diagrams describing the coherent charged-current (mediated by $W^-$ ) and neutral (mediated by $Z^0$ ) current neutrino scattering and the coherent charged-current antineutrino scattering. $N$ represents the nucleons. . . . .	19
1.3	$P_{\bar{\nu}_e \rightarrow \bar{\nu}_e}$ in function of KamLAND energy and averaged baseline. . . . .	24
1.4	Two options for the neutrino mass ordering. . . . .	26
2.1	Masses of the Standard Model fermions. . . . .	32
2.2	Standard Model particles confined in the 4-dimensional “brane” embed in a $(4 + d)$ -dimensional “bulk”, where gravitons and bulk neutrinos $\Psi^\alpha$ can freely propagate. Here, $d$ is the number of the extra dimensions. . . . .	33
2.3	The behavior of the $S_{0n}^1$ as a function of $m_1^D$ , assuming $R_{\text{ED}} = 0.5 \text{ eV}^{-1}$ . Considering the terms of order $n = 0$ as the most active states, the higher orders of the Kaluza-Klein modes will considerably affect the mixing when $m_1^D R_{\text{ED}} \approx 1$ . . . . .	38
2.4	The three most active neutrino masses $\lambda_i^{(0)}$ in function of Dirac mass $m_1^D$ , with $R_{\text{ED}} = 0.5 \text{ eV}^{-1}$ for the normal mass ordering. When $m_1^D R_{\text{ED}} \approx 1$ , the mass values become degenerated. . . . .	39
2.5	SBN layout with the three liquid Argon detectors placed along the central axis of BNB complex plus the event display of electron or muon interaction inside the liquid Argon. . . . .	41
2.6	Probability regions for different values of LED parameters, $m_0$ and $R_{\text{ED}}$ . . . . .	42
2.7	Left (Right) panel: Sensitivity limits for the LED parameters, $R_{\text{ED}}$ and $m_0$ , considering normal (inverted) ordering of neutrino masses. . . . .	47
2.8	Left (right) panel: Allowed regions for the ‘true’ LED parameters $m_0 = 0.05 \text{ eV}$ and $1/R_{\text{ED}} = 0.398 \text{ eV}$ and assuming as test model the LED scenario for normal (inverted) ordering. All the other oscillation parameters were fixed to their best fit values. . . . .	48
2.9	Left (Right) panel: Sensitivity limit at 90% of C.L. for the 3+1 model for the muon neutrino disappearance channel (electron neutrino appearance channel), in the parameter space which depends on $\sin^2 2\theta_{\mu\mu}$ ( $\sin^2 2\theta_{\mu e}$ ) and $\Delta m_{41}^2$ . . . . .	50
2.10	Left (Right) panel: Allowed Regions considering the ‘true’ neutrino event spectrum given by the 3 + 1 model with the values $\sin^2 2\theta_{\mu\mu} = 0.02$ and $\Delta m_{41}^2 = 1 \text{ eV}^2$ ( $\sin^2 2\theta_{\mu e} = 0.01$ and $\Delta m_{41}^2 = 1 \text{ eV}^2$ ) in the muon neutrino disappearance channel (the electron neutrino appearance channel). . . . .	51

2.11	Left panel, sensitivity results fitting the 3+1 model parameters assuming the ‘true’ LED parameters $m_0 = 0.05$ eV and $1/R_{\text{ED}} = 0.398$ eV, for normal ordering. Right panel, sensitivity results fitting the LED parameters for the ‘true’ 3+1 parameters $\sin^2 2\theta_{\mu\mu} = 0.1$ and $\Delta m_{41}^2 = 0.5$ eV <sup>2</sup> , also for normal ordering. . . . .	52
3.1	Behavior of the energy distribution functions described in $G_{\pm}^{\text{Majorana}}$ . The helicity-conserving process (left panel) is described by $G_+^{\text{Majorana}}$ , while helicity-flipping process (right panel) is described by $G_-^{\text{Majorana}}$ . . . . .	62
3.2	Layout of LSND and scheme of the neutrino beam production and the expected $\bar{\nu}_e$ event signal from flavor transition mechanism inside the detector. . . . .	65
3.3	Best-fit $\bar{\nu}_e$ spectra at LSND as a function of $L/E_\nu$ for the oscillation hypothesis and for the different heavy-decaying-neutrino scenarios discussed here. . . . .	67
3.4	Allowed regions of the $( U_{\mu 4} ^2, gm_4)$ parameter space when the heavy-neutrino decay hypothesis is matched against the LSND data assuming Majorana (left) or Dirac neutrinos (right). The dots indicate the best-fit-point and the lines represent the 99% (solid), 95% (dashed) and 68% (dotted) confidence level (C.L.) curves. . . . .	68
3.5	Illustration of neutrino production in BNB facility for <i>neutrino mode</i> configuration and event topologies inside MiniBooNE detector. . . . .	70
3.6	Color scheme to collapse the matrix $\mathcal{M}^{\text{sys+stat}}$ (left) into the matrix $\mathcal{M}$ (right) by overlapping blocks with the same color. Observe that the final matrix $\mathcal{M}$ is divided in the sub-blocks $\mathcal{M}_{ee}$ , $\mathcal{M}_{\mu\mu}$ , $\mathcal{M}_{e\mu}$ and $\mathcal{M}_{\mu e}$ , which will be useful in the performance of electron neutrino appearance analysis. . . . .	73
3.7	Best-fit $\nu_e$ spectra at MiniBooNE, neutrino-mode, as a function of $E_\nu$ for the oscillation hypothesis and for the different heavy-neutrino decay scenarios discussed here. . . . .	75
3.8	Allowed regions of the $( U_{\mu 4} ^2, gm_4)$ parameter space when the heavy-neutrino decay hypothesis is matched against the MiniBooNE neutrino-mode data assuming Majorana (left) or Dirac neutrinos (right). . . . .	76
3.9	Allowed regions of the $( U_{\mu 4} ^2, gm_4)$ parameter space when the heavy-neutrino decay hypothesis is matched against the MiniBooNE antineutrino-mode data assuming Majorana (left) or Dirac neutrinos (right). The dots indicate the best-fit-point and the lines represent the 99% (solid), 95% (dashed) and 68% (dotted) C.L. curves . . . . .	77
3.10	Allowed regions of the $( U_{\mu 4} ^2, gm_4)$ parameter space when the heavy-neutrino decay hypothesis is matched against the combined MiniBooNE neutrino-mode and antineutrino-mode data assuming Majorana (left) or Dirac neutrinos (right). The dots indicate the best-fit-point and the lines represent the 99% (solid), 95% (dashed) and 68% (dotted) C.L. curves. . . . .	78
3.11	Allowed regions at 99% (lighter purple), 95% (medium purple) and 68% (darker purple) C.L. of the $( U_{\mu 4} ^2, gm_4)$ parameter space when the heavy-neutrino decay hypothesis is matched against the combined LSND data and MiniBooNE neutrino-mode and antineutrino-mode data assuming Majorana (left) or Dirac neutrinos (right). . . . .	79

3.12	Allowed regions at 99% (lighter purple), 95% (medium purple) and 68% (darker purple) C.L. of the $( U_{\mu 4} ^2, gm_4)$ parameter space when the heavy-neutrino decay hypothesis is matched against the combined LSND, Mini-BooNE and KARMEN data and MINOS constrains assuming Majorana (left) or Dirac neutrinos (right). The dots indicate the best-fit-point. In the same context, the orange regions indicate the sensitivity of the SBN Program at 99% (solid line), 95% (dashed line) and 68% (dotted line) C.L. for Majorana (left) and Dirac neutrinos (right). . . . .	80
3.13	SBN allowed regions for non-zero decay scenario parameters $( U_{\mu 4} ^2, gm_4)$ at 99% (solid line), 95% (dashed line) and 68% (dotted line) C.L. for Majorana (left) and Dirac neutrinos (right). The dots indicate the best-fit-point from the LSND, MiniBooNE, KARMEN and MINOS combined analysis. . . . .	81

# List of Tables

1.1	Neutrino flavors associated to their charged-lepton partners. . . . .	16
1.2	Values of $L$ and $E$ for neutrino experiments with different sources and the ranges of the $\Delta m^2$ eV <sup>2</sup> which they can be most sensitive to oscillations in vacuum. . . . .	28
2.1	SBN detector active masses and distances from the local of the neutrino production. . . . .	40
2.2	Energy range and energy bin size of the electron and muon sample used in this analysis. . . . .	45
2.3	Discrimination power of SBN facility for 3+1 model and LED model. . . .	53
3.1	LSND antineutrino neutrino events data and background expectation. . . .	66

# Contents

<b>1</b>	<b>Introduction to Neutrinos</b>	<b>16</b>
1.1	Neutrinos in the Standard Model . . . . .	17
1.2	Neutrino Oscillations . . . . .	20
1.2.1	The Three Neutrino Oscillation Scenario . . . . .	20
1.3	The Short-Baseline Anomalies . . . . .	28
1.3.1	Adding an Extra Neutrino in the Mixing: the 3+1 Model . . . . .	29
<b>2</b>	<b>Large Extra Dimensions</b>	<b>32</b>
2.1	Formalism . . . . .	34
2.2	The Short-Baseline Neutrino Program . . . . .	40
2.3	Results . . . . .	46
2.3.1	Sensitivity to a non-zero LED oscillation effect on SBN . . . . .	48
2.3.2	3+1 scenario at SBN: sensitivity and accuracy of the measurement .	49
2.3.3	Discrimination power between LED scenario and the 3+1 scenario	50
2.4	Conclusions . . . . .	53
<b>3</b>	<b>A Heavy Neutrino Decay</b>	<b>55</b>
3.1	Formalism . . . . .	56
3.2	Heavy-Decay versus 3+1 Model . . . . .	62
3.2.1	Constraints on New Neutrinos and Neutrino–Scalar Interactions . .	63
3.3	Simulations and Results . . . . .	64
3.3.1	LSND . . . . .	64
3.3.2	MiniBooNE . . . . .	69
3.3.3	LSND and MiniBooNE Combined . . . . .	76
3.3.4	Disappearance searches: KARMEN and MINOS/MINOS+ . . . . .	76
3.3.5	SBN . . . . .	80
3.4	Conclusions . . . . .	81
<b>4</b>	<b>Final Conclusions</b>	<b>83</b>
	<b>Bibliography</b>	<b>84</b>

# Chapter 1

## Introduction to Neutrinos

Neutrinos are neutral elementary particles produced via weak interactions by the unstable particle and radioactive element decays. They belong to the lepton class, fermions that do not interact via strong force and - as far as we know - there are three different neutrino types, or “flavors”, each one associated with a charged lepton as shown in Table (1.1) [1].

Neutrino was first postulated in 1930 by Wolfgang Pauli to address an explanation to the beta decay energy spectrum [2]. In a letter to the Physical Institute of the Federal Institute of Technology, Zurich [3], Pauli proposed that a neutral, very light, and spin-half particle was carrying away the missing energy and angular momentum of the particles in the nuclear reaction. Incorporating Pauli’s neutrino hypothesis, Enrico Fermi formulated in 1934 the mathematical theory of weak interactions, in which a neutron converts into a proton and simultaneously creates an electron and an antineutrino.

Neutrino	Charged Lepton
$\nu_e$	Electron ( $e$ )
$\nu_\mu$	Muon ( $\mu$ )
$\nu_\tau$	Tau ( $\tau$ )

Table 1.1: Neutrino flavors associated to their charged-lepton partners.

Besides successfully predicted the correct shape of the energy spectrum of the emitted electrons in beta decay, Fermi’s theory of the weak force also suggested a reaction by which a free neutrino would interact with matter producing detectable products: the inverse beta decay process. However, due to the interaction’s weak character, neutrino’s first experimental detection occurred twenty-five years later its postulation. In 1956, Reines and Cowan reported in Ref. [4] the preliminary observation of neutrino inverse beta decay reactions in a liquid scintillator detector. “For the detection of the neutrino”, Reines won the Nobel prize in 1995.

In 1962, Leon M. Lederman, Melvin Schwartz, and Jack Steinberger reported the existence of a second neutrino type with the first detection of the muon neutrino ( $\nu_\mu$ ) [5]. When the tau lepton ( $\tau$ ) was discovered in 1975 [6] in the Stanford Linear Accelerator (SLAC), it was expected that there would be a third type of neutrino associated with tau. The first evidence of tau neutrino came from observations of the initial and final particles’ energy and momentum differences in the tau decay - similar to the beta one. The tau

neutrino detection was announced in the summer of 2000 by the DONUT collaboration at Fermi National Accelerator Laboratory (Fermilab) [7].

The idea of neutrino masses and oscillations was suggested by Bruno Pontecorvo in 1957 [8] using as an analogy the neutral kaons system. In 1967, he generalized the oscillation formalism employing the hypothesis of Z. Maki, M. Nakagawa, and S. Sakata [9] that the states of flavors  $\nu_e$  and  $\nu_\mu$  (the  $\nu_\tau$  had not yet been discovered) were mixtures of two states of neutrino masses. Neutrino oscillation is essential because it directly implies non-zero neutrino masses and lepton number violation, both phenomena not contemplated by the Standard Model of particle physics.

In 1985, Stanislav Mikheyev and Alexei Y. Smirnov expanded the Lincoln Wolfenstein work from 1978 [10] by remarking that flavor oscillation could be modified when neutrinos propagate through matter [11]. This effect, called *MSW*, is important to study neutrinos that cross the earth layers (for example, in MINOS [12], Super-Kamiokande [13] and DUNE [14] experiments) and electron neutrinos that are produced and oscillate inside the dense sun interior to reach the earth eventually. The deficit of electron neutrinos coming from the sun was reported by many experiments [15, 16, 17] until being addressed as the neutrino oscillation phenomenon by the Sudbury Neutrino Observatory (SNO) experiment [18, 19] in 2002. In 2015, Arthur McDonald, the director of SNO, won the Nobel Prize “for the discovery of neutrino oscillations, which shows that neutrinos have mass”.

In 1994, LSND (Liquid Scintillator Neutrino Detector) Collaboration reported the evidence of anomalous neutrino oscillation in short-baseline regime [20]. Only in 1998, the Super-Kamiokande experiment detected neutrino oscillations for the first time with great statistical significance [13], making use of atmospheric neutrino data. T. Kajita, scientific leader of Super-Kamiokande, shared the Nobel Prize with McDonald in 2015. Reactor neutrino experiments as Double Chooz [21], Daya Bay [22] and RENO [23], together with Super-Kamiokande, completed the three neutrino oscillation framework by showing that all oscillation channels are possible:  $\nu_e, \nu_\mu, \nu_\tau \rightarrow \nu_e, \nu_\mu, \nu_\tau$ . All the information brought by the mentioned experiments showed, for the first time, experimental evidence that the Standard Model of elementary particles [24, 25, 26] could not predict: neutrino oscillations.

## 1.1 Neutrinos in the Standard Model

Although the Standard Model does not contemplate the neutrino oscillations, some of the neutrino properties are well described by this gauge theory. Figure 1.1 shows the particles that compose the Standard Model, along with their masses<sup>1</sup>, electric charges and spins. The fermions of the Standard Model are subdivided into quarks and leptons. They are allocated in three generations or families, where particles in the same row share identical properties, except for the masses. The gauge bosons intermediate the strong (gluon),

---

<sup>1</sup>It is important to mention that quark mass measurements are related with hadron properties, once quarks do not exist as free particles. Neutrino masses limits are given by charged lepton decays and cosmology.

Three generations of matter (fermions)			Interactions / force carriers (bosons)		
	I	II	III		
mass	$\approx 2.2 \text{ MeV}/c^2$	$\approx 1.28 \text{ GeV}/c^2$	$\approx 173.1 \text{ GeV}/c^2$	0	$\approx 124.97 \text{ GeV}/c^2$
charge	2/3	2/3	2/3	0	0
spin	1/2	1/2	1/2	1	0
	<b>u</b> up	<b>c</b> charm	<b>t</b> top	<b>g</b> gluon	<b>H</b> higgs
	$\approx 4.7 \text{ MeV}/c^2$	$\approx 96 \text{ MeV}/c^2$	$\approx 4.18 \text{ GeV}/c^2$	0	
	-1/3	-1/3	-1/3	0	
	1/2	1/2	1/2	1	
	<b>d</b> down	<b>s</b> strange	<b>b</b> bottom	<b><math>\gamma</math></b> photon	
	$\approx 0.511 \text{ MeV}/c^2$	$\approx 105.66 \text{ MeV}/c^2$	$\approx 1.777 \text{ GeV}/c^2$	$\approx 91.19 \text{ GeV}/c^2$	
	-1	-1	-1	0	
	1/2	1/2	1/2	1	
	<b>e</b> electron	<b><math>\mu</math></b> muon	<b><math>\tau</math></b> tau	<b>Z</b> Z boson	
	$< 1.0 \text{ eV}/c^2$	$< 0.17 \text{ MeV}/c^2$	$< 18.2 \text{ MeV}/c^2$	$\approx 80.39 \text{ GeV}/c^2$	
	0	0	0	$\pm 1$	
	1/2	1/2	1/2	1	
	<b><math>\nu_e</math></b> neutrino	<b><math>\nu_\mu</math></b> neutrino	<b><math>\nu_\tau</math></b> neutrino	<b>W</b> W boson	

QUARKS (rows 1-3)  
LEPTONS (rows 4-6)  
GAUGE BOSONS (rows 7-9)  
SCALAR BOSON (row 5)

Figure 1.1: The elementary particles of the Standard Model. The fermions in the same position of each generation share the same properties, except the masses. Observe the mass values grown hierarchically with the generation. Gauge bosons mediate the fundamental forces (except the gravity), and the Higgs boson is related to the elementary particle masses. Particle masses, electric charge, and spin were taken from Ref. [27]. Figure based on Ref. [28].

weak ( $Z^0$  and  $W^\pm$ ), and electromagnetic (photon) interactions, while the Higgs boson is responsible for the Yukawa couplings that give mass to the particles.

Neutrinos are found in the lepton category in the Standard Model. As they are neutral particles, they can only interact via weak forces. The component of the Electroweak Lagrangian that concerns neutrinos is:

$$\mathcal{L}^\nu = \sum_{\alpha=e,\mu,\tau} i\bar{\nu}_{\alpha L}\not{\partial}\nu_{\alpha L} - \frac{g_W}{\sqrt{2}} \sum_{\alpha=e,\mu,\tau} \bar{\nu}_{\alpha L}\gamma^\mu l_{\alpha L}W_\mu + \text{H.c.} - \frac{g_W}{2\cos\theta_w} \sum_{\alpha=e,\mu,\tau} \bar{\nu}_{\alpha L}\gamma^\mu\nu_{\alpha L}Z_\mu \quad (1.1)$$

where  $\bar{\nu} \equiv \nu^\dagger\gamma^0$ ,  $g_W$  is the coupling constant of the weak interaction and  $\theta_w$  is the Weinberg angle. The first term of the Lagrangian in the Eq. 1.1 describes the kinetic terms of the neutrino fields; the second one denotes the charged-current interaction of the neutrino  $\nu_\alpha$ , its charged-lepton partner  $l_\alpha$ , and the boson  $W$ . The third term is the neutral-current interaction among neutrinos and the  $Z$  boson.

The weak interactions are the key point to describe neutrino production, like beta decay ( $n \rightarrow p^+ + e^- + \bar{\nu}_e$ ), and neutrino interaction, like the inverse beta decay ( $\bar{\nu}_e + p \rightarrow n + e^+$ ), for example. Also, the terms in Eq. 1.1 lead the neutrino coherent charged- and neutral-current scattering processes as illustrated in Figure 1.2. These interactions are

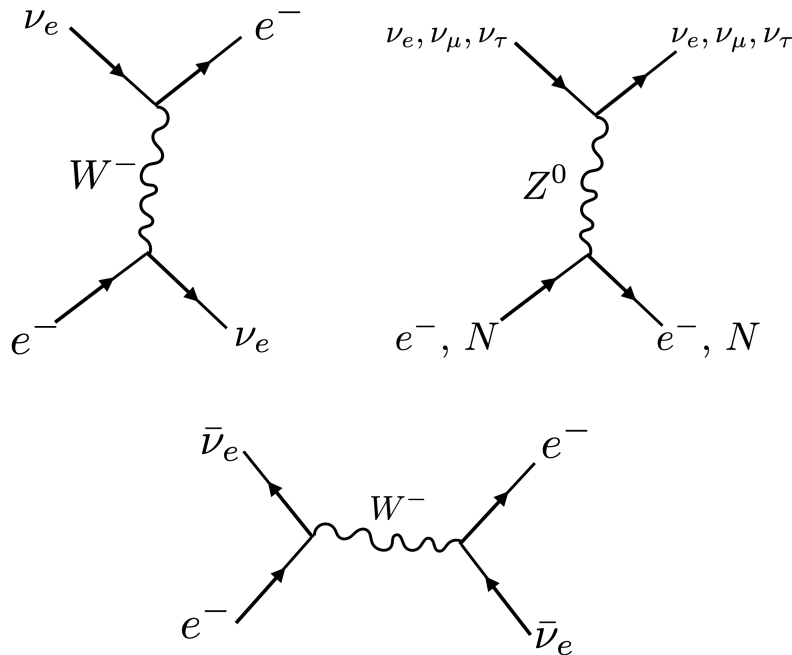


Figure 1.2: Feynman diagrams describing the coherent charged-current (mediated by  $W^-$ ) and neutral (mediated by  $Z^0$ ) current neutrino scattering and the coherent charged-current antineutrino scattering.  $N$  represents the nucleons.

fundamental in the description of the neutrino propagation in the matter.

In the Standard Model, the fermion mass terms are built through Yukawa couplings of the left- and right-handed fermion fields with a scalar doublet via Higgs mechanism [29, 30, 31]. Strictly, neutrinos do not have mass in the Standard Model once its right-handed component  $\nu_R$  is not included. If we want to build neutrino mass terms in a similar way, assuming neutrinos are Dirac particles, we can introduce the  $\nu_R$  field and write the neutrino Yukawa coupling with the neutral scalar boson through the Lagrangian

$$\mathcal{L}_{\text{mass}}^\nu = - \sum_{\alpha, \beta=e, \mu, \tau} \bar{\nu}_{\alpha L} M^{\alpha\beta} \nu_{\beta R} + \text{H.c.} \quad (1.2)$$

where  $M^{\alpha\beta}$  are the neutrino mass matrix elements in the flavor basis. In the case of the charged-leptons, we assumed the mass matrix is already diagonal and can be written as  $\text{diag}\{m_e, m_\mu, m_\tau\}$ , respectively, with the electron, muon, and tau masses. For neutrinos, we rewrite the flavor states on a basis where  $M$  matrix is diagonal. In this way, we introduce two unitary matrices  $U_L$  and  $U_R$  such as

$$\nu_{\alpha L(R)} = \sum_{i=1}^3 U_{L(R)}^{\alpha i} \nu_{iL(R)}, \quad (1.3)$$

where  $U_L^\dagger M U_R = \text{diag}\{m_1, m_2, m_3\}$  and  $m_i$  ( $i = 1, 2, 3$ ) are the neutrino masses. If we plug the term in Eq. 1.3 in the second term of the Eq. 1.1, we obtain the following

$$\mathcal{L}^{CC} = -\frac{g_W}{\sqrt{2}} \sum_{\alpha=e, \mu, \tau} \left( \sum_{i=1}^3 U_{\alpha i L}^* \bar{\nu}_{iL} \gamma^\mu l_{\alpha L} W_\mu + U_{\alpha i L} \bar{l}_{\alpha L} \gamma^\mu \nu_{iL} W_\mu^\dagger \right). \quad (1.4)$$

The Eq. 1.4 says that in the charged-current processes, superposition of the neutrino mass eigenstates is produced with the charged-lepton. We will see how these states evolve with the neutrino propagation in the Sec. 1.2. Notice that neutral-current processes are not sensitive to neutrino mixing. Just a reminder that the Standard Model does not contemplate the neutrino mass term in the Lagrangian in Eq. 1.2.

Since neutrinos are neutral, they can also be Majorana particles. In this case, the neutrino mass terms are given through the Lagrangian

$$\mathcal{L}_{\text{mass}}^{\text{Maj}} = -\frac{m_M}{2}(\overline{\nu_L^c}\nu_L + \overline{\nu_L}\nu_L^c), \quad (1.5)$$

where  $\nu^c \equiv C\gamma^{0T}\nu^*$ ,  $C$  being the operator of charge conjugation and  $m_M$  the Majorana mass. Majorana neutrinos follow the condition  $\nu = \nu^c$ , which implies that chiral fields obey the relation  $\nu_R = \nu_L^c$ . To generate the Majorana mass terms in Eq. 1.5, it is necessary to introduce new couplings that are not contemplated by the Standard Model, like the SU(2) doublets with at least one scalar triplet.

## 1.2 Neutrino Oscillations

Flavor neutrinos are produced via weak interaction processes as a superposition of the mass eigenstates, each one with a specific mass eigenvalue<sup>2</sup>. Because of the tiny mass differences, the mass eigenstates will propagate coherently, leading to flavor oscillations. In this way, an electron neutrino can transmute in a muon neutrino, for example, after traveling a certain distance. Each mass state's contribution in the neutrino's flavor composition is proportional to the element of a unitary matrix  $U$ , which connects both mass and flavor states. In this Section, we will revise the standard oscillation scenario with three - massive and flavored - neutrinos and the efforts of some neutrino experiments in measuring the oscillation parameters.

### 1.2.1 The Three Neutrino Oscillation Scenario

We will proceed with the derivation of the standard theory of neutrino oscillations [32, 33, 34]. The unitary matrix  $U$  is introduced in the charged-current interactions of the lepton doublets and associates flavor neutrinos with massive neutrinos states. The three neutrino oscillation scenario involves the mixing among the three SM flavor neutrinos with three mass eigenstates as

$$|\nu_\alpha\rangle = \sum_{i=1}^3 U_{\alpha i}^* |\nu_i\rangle \quad (\alpha = e, \mu, \tau; \quad UU^\dagger = \mathbb{1}) \quad (1.6)$$

or

$$|\nu_i\rangle = \sum_{\alpha=e,\mu,\tau} U_{\alpha i} |\nu_\alpha\rangle, \quad (i = 1, 2, 3) \quad (1.7)$$

---

<sup>2</sup>This superposition of mass states is due to the energy and momentum uncertainties of the particles that participate in the neutrino production process.

where  $\nu_\alpha$  are the neutrinos flavor eigenstates and  $\nu_i$  are the neutrino mass eigenstates. Both flavor and mass eigenstates establish an orthogonal basis. If we consider the antineutrinos, we need to change  $U \rightarrow U^*$  in both Eq. 1.6 and Eq. 1.7. The matrix  $U$ , also called PMNS (Pontecorvo-Maki-Nakagawa-Sakata) matrix in this scenario, can be parameterized as [35]

$$\begin{aligned}
U &= \begin{pmatrix} U_{e1} & U_{e2} & U_{e3} \\ U_{\mu1} & U_{\mu2} & U_{\mu3} \\ U_{\tau1} & U_{\tau2} & U_{\tau3} \end{pmatrix} \\
&= \begin{pmatrix} 1 & 0 & 0 \\ 0 & c_{23} & s_{23} \\ 0 & -s_{23} & c_{23} \end{pmatrix} \begin{pmatrix} c_{13} & 0 & s_{13}e^{-i\delta} \\ 0 & 1 & 0 \\ -s_{13}e^{-i\delta} & 0 & c_{13} \end{pmatrix} \begin{pmatrix} c_{12} & s_{12} & 0 \\ -s_{12} & c_{12} & 0 \\ 0 & 0 & 1 \end{pmatrix} \begin{pmatrix} e^{i\alpha_1/2} & 0 & 0 \\ 0 & e^{i\alpha_2/2} & 0 \\ 0 & 0 & 1 \end{pmatrix} \\
&= \begin{pmatrix} c_{12}c_{13} & s_{12}c_{13} & s_{13}e^{-i\delta} \\ -s_{12}c_{23} - c_{12}s_{23}s_{13}e^{i\delta} & c_{12}c_{23} - s_{12}s_{23}s_{13}e^{i\delta} & s_{23}c_{13} \\ s_{12}s_{23} - c_{12}c_{23}s_{13}e^{i\delta} & -c_{12}s_{23} - s_{12}c_{23}s_{13}e^{i\delta} & c_{23}c_{13} \end{pmatrix} \begin{pmatrix} e^{i\alpha_1/2} & 0 & 0 \\ 0 & e^{i\alpha_2/2} & 0 \\ 0 & 0 & 1 \end{pmatrix},
\end{aligned} \tag{1.8}$$

where  $c_{ij} = \cos\theta_{ij}$  and  $s_{ij} = \sin\theta_{ij}$ , and  $\theta_{ij}$  is the mixing angle between the mass eigenstates  $i$  and  $j$  ( $i, j = 1, 2, 3$  and  $i \neq j$ ). The phase factor  $\delta$  measures the violation of the charge-parity (CP) symmetry, i.e. the difference between the particle and antiparticle behaviors in production and propagation. If neutrinos are Majorana particles, the phases  $\alpha_1$  and  $\alpha_2$  contribute in CP violation, although here they represent a global phase and do not interfere in the oscillation phenomenon.

The mass neutrino states  $|\nu_i\rangle$ , in vacuum, are eigenstates of the Hamiltonian

$$\mathcal{H}|\nu_i\rangle = E_i|\nu_i\rangle \tag{1.9}$$

with the energy eigenvalues given by

$$E_i = \sqrt{|\vec{p}_i|^2 + m_i^2} \tag{1.10}$$

where  $\vec{p}_i$  is the three-component momenta and  $m_i$  is the mass of the neutrino state  $|\nu_i\rangle$ . The evolution of the mass states in time is described by Schrodinger's Equation

$$\mathcal{H}|\nu_i(t)\rangle = i\frac{d}{dt}|\nu_i(t)\rangle, \tag{1.11}$$

which the solution are plane waves

$$|\nu_i(t)\rangle = e^{-iE_it}|\nu_i\rangle, \tag{1.12}$$

and we consider  $|\nu_i\rangle = |\nu_i(t=0)\rangle$ . Applying the relations in Eq. 1.7 on the mass states in the right side of Eq. 1.12 and making use of the Eq. 1.6, the time evolution of the neutrino flavor state  $|\nu_\alpha(t)\rangle$  is given by

$$|\nu_\alpha(t)\rangle = \sum_i U_{\alpha i}^* e^{-iE_it} \sum_{\beta=e,\mu,\tau} U_{\beta i} |\nu_\beta\rangle. \tag{1.13}$$

The expression in Eq. 1.13 says that the time evolution of a neutrino flavor state, which is pure  $|\nu_\beta\rangle$  in  $t = 0$ , is a superposition of different flavor states at time  $t > 0$ . In this way, to compute the transition probability of a neutrino  $\nu_\beta$  being detected as a *specific* neutrino  $\nu_\alpha$ , after travelling a time  $t > 0$ , we evaluate

$$P_{\nu_\beta \rightarrow \nu_\alpha}(t) = |\langle \nu_\alpha(t) | \nu_\beta \rangle|^2 = \sum_{ij} U_{\alpha i} U_{\beta i}^* U_{\alpha j}^* U_{\beta j} e^{-i(E_j - E_i)t}. \quad (1.14)$$

For ultrarelativistic neutrinos, we can approximate the energy eigenvalues in Eq. 1.10 as

$$E_i \simeq E + \frac{m_i^2}{2E} \quad (1.15)$$

and

$$E_j - E_i \simeq \frac{m_j^2 - m_i^2}{2E}. \quad (1.16)$$

where  $E = |\vec{p}|$ . The approximation in Eq. 1.16 says that all the mass eigenstates are produced and travel with the same energy  $E$ . Also, in the ultrarelativistic limit, we can approximate  $t = L$ . We do not have access to the time when the neutrinos are produced, but the distance they propagate from the neutrino source to the detector. Therefore, the time-dependent oscillation probability in Eq. 1.14 finally becomes

$$P_{\nu_\beta \rightarrow \nu_\alpha}(E, L) = |\langle \nu_\alpha(L) | \nu_\beta \rangle|^2 = \sum_{ij} U_{\alpha i} U_{\beta i}^* U_{\alpha j}^* U_{\beta j} e^{-i \frac{m_j^2 - m_i^2}{2E} L}. \quad (1.17)$$

We can expand the Eq. 1.17 in a more explicit form as follows:

$$\begin{aligned} P_{\nu_\beta \rightarrow \nu_\alpha}(E, L) &= \sum_{ij} U_{\alpha i} U_{\beta i}^* U_{\alpha j}^* U_{\beta j} e^{-i \frac{m_j^2 - m_i^2}{2E} L} \\ &= \sum_{ij} U_{\alpha i} U_{\beta i}^* U_{\alpha j}^* U_{\beta j} \left( e^{-i \frac{m_j^2 - m_i^2}{2E} L} + 1 - 1 \right) \\ &= \sum_{ij} U_{\alpha i} U_{\beta i}^* U_{\alpha j}^* U_{\beta j} \left( e^{-i \frac{m_j^2 - m_i^2}{2E} L} - 1 \right) + \sum_{ij} U_{\alpha i} U_{\beta i}^* U_{\alpha j}^* U_{\beta j} \\ &= \left( \sum_{i < j} + \sum_{i > j} \right) U_{\alpha i} U_{\beta i}^* U_{\alpha j}^* U_{\beta j} \left( e^{-i \frac{m_j^2 - m_i^2}{2E} L} - 1 \right) + \sum_i U_{\alpha i} U_{\beta i}^* \sum_j U_{\alpha j}^* U_{\beta j} \\ &= \sum_{i > j} U_{\alpha i} U_{\beta i}^* U_{\alpha j}^* U_{\beta j} \left( e^{-i \frac{m_j^2 - m_i^2}{2E} L} - 1 \right) + \sum_{i > j} U_{\alpha i}^* U_{\beta i} U_{\alpha j} U_{\beta j}^* \left( e^{i \frac{m_j^2 - m_i^2}{2E} L} - 1 \right) \\ &\quad + \delta_{\alpha\beta} \delta_{\alpha\beta} \end{aligned}$$

$$\begin{aligned}
&= \sum_{i>j} (U_{\alpha i} U_{\beta i}^* U_{\alpha j}^* U_{\beta j} + U_{\alpha i}^* U_{\beta i} U_{\alpha j} U_{\beta j}^*) \left[ \cos \left( \frac{m_j^2 - m_i^2}{2E} L \right) - 1 \right] \\
&- \sum_{i>j} (U_{\alpha i} U_{\beta i}^* U_{\alpha j} U_{\beta j} - U_{\alpha i}^* U_{\beta i} U_{\alpha j} U_{\beta j}^*) \left[ i \sin \left( \frac{m_j^2 - m_i^2}{2E} L \right) \right] + \delta_{\alpha\beta} \\
&= \delta_{\alpha\beta} - 4 \sum_{i>j} \text{Re} (U_{\alpha i} U_{\beta i}^* U_{\alpha j}^* U_{\beta j}) \sin^2 \left( \frac{m_j^2 - m_i^2}{4E} L \right) \\
&+ 2 \sum_{i>j} \text{Im} (U_{\alpha i} U_{\beta i}^* U_{\alpha j}^* U_{\beta j}) \sin \left( \frac{m_j^2 - m_i^2}{2E} L \right)
\end{aligned} \tag{1.18}$$

The oscillation phase in Eq. 1.18 can be expressed as (reinserting  $c e \hbar^3$ )

$$\begin{aligned}
\frac{(m_j^2 - m_i^2) c^4 L}{4 \hbar c E} &= \frac{1}{4 \hbar c} \times \frac{\Delta m_{ji}^2 c^4 L \text{ MeV}}{\text{eV}^2 \text{ m } E} \times \frac{1 \text{ eV}^2 1 \text{ m}}{1 \text{ MeV}} \\
&= \frac{1}{4 (197.327) \text{ MeV fm}} \times \frac{10^{-12} \text{ MeV}^2 10^{15} \text{ fm}}{1 \text{ MeV}} \times \frac{\Delta m_{ij}^2 c^4 L \text{ MeV}}{\text{eV}^2 \text{ m } E} \\
&\simeq 1.27 \times \frac{\Delta m_{ij}^2 c^4 L \text{ MeV}}{\text{eV}^2 \text{ m } E}
\end{aligned} \tag{1.19}$$

where  $\hbar c = 197.327 \text{ MeV fm}$  and  $(m_j^2 - m_i^2) \equiv \Delta m_{ji}^2$ . When the oscillation phase in Eq. 1.19 is equal  $\pi$ , the terms dependent of sines in Eq. 1.18 vanish and the probability is 1. We have in this situation, the first oscillation peak where the neutrino is again in its initial flavor  $\nu_\alpha$ . Hence, we can define the oscillation length  $L_{\text{osc}}$  as

$$L_{\text{osc}} = \frac{\pi E}{1.27 \Delta m_{ji}^2}. \tag{1.20}$$

Many neutrino experiments with different designs were set to measure the parameters of the three neutrino oscillation scenario. They made use of the oscillation length and other features in the oscillation probability to reach the best sensitivities to some of these parameters. We will point some of the neutrino experiment aspects to observe the aimed oscillation parameters.

### Three Neutrino Oscillation Parameter Measurements

The current values of the oscillation parameters considering the three neutrino scenario are compiled in the Particle Data Group (PDG) latest review [27]. We will divide them by sectors and briefly comment about each one as follows:

1)  $\Delta m_{21}^2$  and  $\sin^2 \theta_{12}$ : The values of these parameters are obtained substantially with ex-

---

<sup>3</sup>All the expressions we have employed in this thesis are in natural units ( $c = \hbar = 1$ ). We applied  $c e \hbar$  in Eq. 1.19 to justify the units of energy  $E$ , baseline  $L$  and the mass-squared differences  $m_j^2 - m_i^2$  in the oscillation phase.

periments that detect solar neutrino and the KamLAND (Kamioka Liquid Scintillator Antineutrino Detector) experiment, which records reactor neutrinos. In the sun, electron neutrinos are mainly produced via proton-proton collisions and travel through dense solar environment until they reach earth detectors. These experiments, which include Super-Kamiokande [36, 37, 38], SNO [39], Borexino [40, 41, 42], search for electron neutrino disappearance ( $P_{\nu_e \rightarrow \nu_e}$ ) due to electron neutrino oscillation to muon or tau neutrinos. KamLAND experiment detects electron antineutrinos from nuclear reactions, mainly Uranium and Plutonium fission chains, occurring in the power reactor units surrounding the detector. Kamland searches for electron antineutrino disappearance ( $P_{\bar{\nu}_e \rightarrow \bar{\nu}_e}$ ). The current values of  $\Delta m_{21}^2$  and  $\sin^2 \theta_{12}$  are

$$\sin^2 \theta_{12} = 0.307_{-0.012}^{+0.013} \text{ Ref. [43]} \quad \Delta m_{21}^2 = 7.53 \pm 0.18 \times 10^{-5} \text{ eV}^2 \text{ Ref. [44]}.$$

For illustrative purposes, let's consider the averaged baseline of KamLAND  $L \approx 180$  km and the energy window with range  $E = [1, 8]$  MeV. Figure 1.3 shows the probability of electron antineutrino disappearance ( $P_{\bar{\nu}_e \rightarrow \bar{\nu}_e}$ ) in function of KamLAND energy and baseline. The other oscillation parameters were obtained from Nu-FIT 5.0 in Ref. [45]. Observe that for this configuration, the mass-squared difference  $\Delta m_{31}^2$  (magenta curve) leads to fast oscillations, which cannot be solved by the detector resolution and is averaged-out ( $\sin^2(\Delta m_{31}^2 L/4E) \rightarrow 0.5$ ). Only the oscillation ruled by  $\Delta m_{21}^2$  (black curve) appears to be relevant to KamLAND energy and baseline.

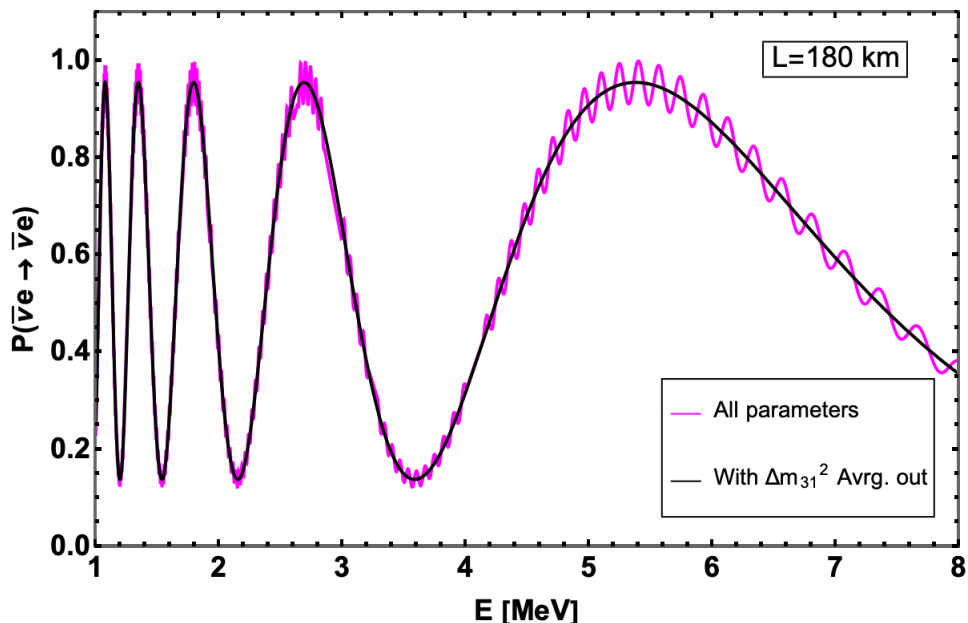


Figure 1.3:  $P_{\bar{\nu}_e \rightarrow \bar{\nu}_e}$  in function of KamLAND energy and averaged baseline. In the magenta curve, all the oscillation parameters contribute, while in the black curve the mass-squared difference  $\Delta m_{31}^2$  was averaged-out. The oscillation parameters were obtained from Nu-FIT 5.0 in Ref. [45].

In addition, the oscillation probability of the electron neutrino disappearance when

we average-out the fast oscillations driven by  $\Delta m_{31}^2$  is approximately

$$P_{\bar{\nu}_e \rightarrow \bar{\nu}_e}^{\text{avg-out}} \simeq 1 - \cos^4 \theta_{13} \sin^2 2\theta_{12} \sin^2 \left( 1.27 \frac{\Delta m_{21}^2 L}{E} \right) - \frac{1}{2} \sin^2 2\theta_{13}, \quad (1.21)$$

which means that the survival probability also depends on  $\theta_{13}$  parameter. This angle, on the other hand, is better constrained by other experiments as we can see in the following.

**2)  $\sin^2 \theta_{13}$ :** The value of the  $\theta_{13}$  comes mainly from the reactor neutrino experiments with baseline  $L \simeq 1$  km and energies of units of MeV. These experiments also search for electron antineutrino disappearance ( $P_{\bar{\nu}_e \rightarrow \bar{\nu}_e}$ ), but the energy and baseline are now relevant for oscillations driven by  $\Delta m_{31}^2$  and the combination  $|\Delta m_{32}^2| \equiv |\Delta m_{31}^2 - \Delta m_{21}^2|$ , both dependent of  $\sin^2 2\theta_{13}$ . The data from the Daya-Bay [46], Double-Chooz [47] and RENO [48] experiments constraints  $\theta_{13}$  value in the form

$$\sin^2 \theta_{13} = 2.18 \pm 0.07 \times 10^{-2} \quad (\text{PDG average}). \quad (1.22)$$

**3)  $\sin^2 \theta_{23}$ ,  $\Delta m_{32}^2$  and  $\delta$ :** Currently, this sector attracts more attention from the point of view of the three neutrino oscillation phenomenology, once their measurements can give us hints about open questions inside neutrino physics: among them, the correct neutrino mass ordering and CP-violation in the leptonic sector.

There are two options for the neutrino mass ordering: normal and inverted as we can see in Figure 1.4. The mass-squared difference  $\Delta m_{21}^2 > 0$  is a positive number due to solar neutrino results. If  $\Delta m_{32}^2 > 0$ , we have the normal mass ordering which means that:  $m_3 > m_2 > m_1$ . If  $\Delta m_{32}^2 < 0$ , we have the inverted mass ordering and  $m_2 > m_1 > m_3$ . Each neutrino mass ordering is associated with theories that provide neutrino masses. Determining the correct one is an important contribution in the studies of the elementary interactions. From the point of view of neutrino oscillations, the neutrino mass ordering can be obtained by measuring the true sign of  $\Delta m_{32}^2$ .

The CP-violation phase  $\delta$  determines the different behaviors between neutrino and antineutrino probabilities. If  $\delta = 0$  or  $\delta = \pi$ , then  $P_{\nu_\alpha \rightarrow \nu_\beta} = P_{\bar{\nu}_\alpha \rightarrow \bar{\nu}_\beta}$ . In this way, a good way to establish the CP-violation parameter is comparing the performance of the neutrino and antineutrino oscillations.

Accelerator and atmospheric neutrino experiments made meaningful progress in determining the neutrino mass ordering and the CP-violation phase  $\delta$ . Atmospheric neutrino experiments like IceCube [50] and Super-Kamiokande [51] detected neutrinos produced from cosmic ray interactions in the earth's atmosphere. The baseline for atmospheric neutrinos varies from dozens to thousands of kilometers if we consider the neutrinos produced on the other side of the earth, that cross its inner layers and reach up-going the detector. Typical energies of atmospheric neutrinos cover hundreds of MeV to dozens of GeV.

The accelerator neutrino experiments, like NO $\nu$ A [52], T2K [53] and MINOS [54, 55], detect neutrinos produced in particle accelerator complexes. Usually, protons are accelerated and impinge in a target, producing unstable particles that decay into neutrinos. These neutrinos have energies from dozens of MeV to units of GeV. The required baseline to study the parameters of this sector is from hundreds to thousands of kilometers.

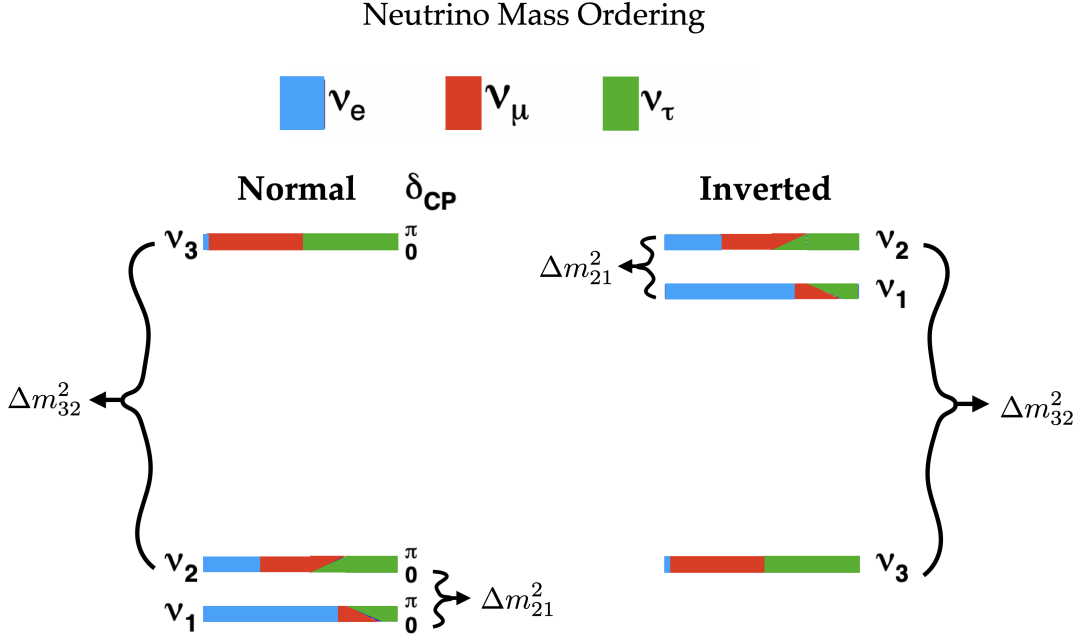


Figure 1.4: Two options for the neutrino mass ordering. Normal:  $\Delta m_{32}^2 > 0$  and Inverted:  $\Delta m_{32}^2 < 0$ . Observe that the contributions of  $\nu_\mu$  and  $\nu_\tau$  neutrinos in  $\nu_1$  and  $\nu_2$  depend on the value of the  $\delta$ . Figure taken from Ref. [49] with modifications.

The oscillation probability channels that atmospheric and accelerator experiments mainly search are:

$$P_{\nu_\mu \rightarrow \nu_\mu}^{(-)} \quad P_{\nu_\mu \rightarrow \nu_e}^{(-)} \quad P_{\nu_e \rightarrow \nu_\mu}^{(-)}$$

For the mentioned energy and baseline configurations, the experiments cannot solve the oscillation phase leading by  $\Delta m_{21}^2$ , which means that  $(1.27\Delta m_{21}^2 L/E) < 1$ . In this way, the oscillation probability for the channels above are, approximately

$$P_{\nu_\mu \rightarrow \nu_\mu}^{(-)} \simeq 1 - 4 \cos^2 \theta_{13} \sin^2 \theta_{23} (1 - \cos^2 \theta_{23} \sin^2 \theta_{13}) \sin^2 \left( \frac{1.27\Delta m_{32}^2 L}{E} \right) \quad (1.23)$$

$$P_{\nu_\mu \leftrightarrow \nu_e}^{(-)} \simeq \sin^2 2\theta_{13} \sin^2 \theta_{23} \sin^2 \left( \frac{1.27\Delta m_{32}^2 L}{E} \right) \mp \left( \frac{1.27\Delta m_{21}^2 L}{E} \right) \cos \theta_{13} \sin^2 2\theta_{12} \sin^2 2\theta_{23} \sin^2 2\theta_{13} \sin \delta \sin^2 \left( \frac{1.27\Delta m_{32}^2 L}{E} \right) \quad (1.24)$$

where in the Eq. 1.24, we expand  $P_{\nu_\mu \leftrightarrow \nu_e}^{(-)}$  in the first order of  $(1.27\Delta m_{21}^2 L/E)$ . Also, the  $\mp$  sign that goes along with the CP-violation term  $\delta$  in Eq. 1.24 indicates the difference between neutrino and antineutrino probabilities: the sign is negative for neutrinos and positive for antineutrinos. Thus, the capability of studying neutrino and antineutrino probabilities enable to these experiments, mainly the accelerator ones, the measurement of the CP-violation phase  $\delta$ .

We also can see that the probabilities in Eq. 1.23 and Eq. 1.24 are dependent of  $\sin^2 \theta_{23}$  for atmospheric and accelerator experiments. However, once they cannot solve  $\Delta m_{21}^2$ , the change of the sign of  $\Delta m_{32}^2$  on the oscillation phases does not modify the probabilities in the Eq. 1.23 and Eq. 1.24. So, how to determine the neutrino mass ordering? Via modifications in the oscillation probabilities due to *matter effects*.

Neutrinos that travel through the sun, the earth's crust or the entire planet experience matter effects. Matter effects are given by the presence of electrons, neutrons, and protons as the components of matter. Due to charged and neutral current interactions of the neutrinos and antineutrinos with electrons and nucleons (see Sec. 1.1), we need to add terms that define the potential of these interactions in the neutrino Hamiltonian from Eq. 1.11. The energy eigenvalues, as well as the neutrino mass eigenstates, change because of the new Hamiltonian diagonalization. In this way, the new oscillation amplitude and phase have dependency with the matter potential and this dependency is sensitive to the mass ordering. For example, the leading order term in Eq. 1.24 becomes, in the presence of matter effects and constant density,

$$P_{\nu_{\mu}^{(-)} \leftrightarrow \nu_e^{(-)}} \simeq \sin^2 2\theta_{13}^M \sin^2 \theta_{23} \sin^2 \left( \frac{1.27 \Delta m_{32,M}^2 L}{E} \right), \quad (1.25)$$

where

$$\sin^2 2\theta_{13}^M = \frac{\sin^2 2\theta_{13}}{\sin^2 2\theta_{13} + (A - \cos 2\theta_{13})^2}, \quad (1.26)$$

$$\Delta m_{32,M}^2 = \Delta m_{32}^2 \sqrt{\sin^2 2\theta_{13} + (A - \cos 2\theta_{13})^2}, \quad (1.27)$$

and

$$A = \pm \frac{\sqrt{2} G_F N_e E}{\Delta m_{32}^2}, \quad (1.28)$$

where  $G_F$  is the Fermi's constant and  $N_e$  is the electron density. The  $+(-)$  sign in Eq. 1.28 is for neutrinos (antineutrinos). Notice now that a change of the  $\Delta m_{32}^2$  sign in Eq. 1.26 and Eq. 1.27 will modify the oscillation probability and this effect can be solved by the mentioned atmospheric and accelerator neutrino experiments.

The current values of the  $\sin^2 \theta_{23}$ ,  $\Delta m_{23}^2$  and  $\delta$  are given by IceCube [50], Super-Kamiokande [51], NO $\nu$ A [52], T2K [53] and MINOS [54, 55] analysis:

$$\begin{aligned} \sin^2 \theta_{23} &= 0.545 \pm 0.021 \quad \text{for normal ordering} \\ &= 0.547 \pm 0.021 \quad \text{for inverted ordering} \\ \Delta m_{32}^2 &= 2.453 \pm 0.034 \times 10^{-3} \text{ eV}^2 \quad \text{for normal ordering} \\ &= -2.546_{-0.040}^{+0.034} \times 10^{-3} \text{ eV}^2 \quad \text{for inverted ordering} \\ \delta &= 1.36 \pm 0.17 \pi. \end{aligned}$$

The future accelerator and atmospheric neutrino experiments DUNE [56] and Hyper-

Kamiokande [57] come to improve the measurements on this sector. With their high statistics, it is expected from both to give a final answer about the still opened questions inside the three neutrino scenario parameters. Also,

In the end, we summarize in Table 1.2 the characteristic baseline  $L$  and neutrino energy  $E$  for the mentioned experiments with different neutrino sources. Also, the mass-squared differences in which the experimental configuration has the most sensitive are also shown.

Experiment	$L$ (m)	$E$ (MeV)	$\Delta m^2$ eV <sup>2</sup>
Atmospheric	$10^4 - 10^7$	$10^2 - 10^5$	$10^{-1} - 10^{-4}$
Reactor	$10^2 - 10^3$ or $10^4 - 10^5$	1	$10^{-2} - 10^{-3}$ or $10^{-4} - 10^{-5}$
Accelerator	$10^5 - 10^6$	$10^3 - 10^4$	$10^{-2} - 10^{-3}$

Table 1.2: Values of  $L$  and  $E$  for neutrino experiments with different sources and the ranges of the  $\Delta m^2$  eV<sup>2</sup> which they can be most sensitive to oscillations in vacuum. Table taken from Ref. [58].

### 1.3 The Short-Baseline Anomalies

As we could see in the previous Subsection 1.2.1, the neutrino experiments can be designed in terms of the neutrino source and the baseline to observe oscillation parameters leaded by a specific oscillation frequency, that depends on  $\Delta m^2$ . Essentially, the two independent mass-squared differences,  $\Delta m_{21}^2 \simeq 7.5 \times 10^{-5}$  eV<sup>2</sup> and  $|\Delta m_{32}^2| \simeq 2.5 \times 10^{-3}$  eV<sup>2</sup>, from the *three neutrino scenario* develop oscillations when the phase is

$$1.27 \frac{(\Delta m_{ij}^2 / \text{eV}^2)(L/\text{m})}{(E/\text{MeV})} \sim \mathcal{O}(1). \quad (1.29)$$

In this context, experiments that operate in the  $L/E \simeq 1$  m/MeV (or km/GeV) regime should not expect signals of flavor transitions due to three neutrino oscillation mechanisms. These neutrino experiments are so-called *short-baseline experiments* and were designed to search for oscillations driven by a mass-squared splitting of  $\Delta m^2 \simeq 1$  eV<sup>2</sup> or larger. Hence, the short-baseline experimental results that cannot be accommodated in the three neutrino scenario define the *short-baseline anomalies*. Some of them are in the following:

1. the **positive signal** or **excess** of electron (anti)neutrino candidates in the LSND [20] and MiniBooNE [59, 60, 61] experiments. Both experiments that collect neutrinos produced in accelerators reported signals of electron neutrino appearance above the expected background. We will come back to these results in Chapter 3;
2. the **deficit** of detected electron neutrinos in Gallium-based experiments, like GALLEX [62, 63, 64] and SAGE [65, 66, 67, 68]. These neutrino experiment have Gallium in their target composition. Nuclear sources that emit electron neutrinos with well-defined decay branching ratios were used to calibrated SAGE and GALLEX detectors. When electron neutrinos interact with Gallium, Germanium is produced and is measurable. Nevertheless, the observed Germanium rate production is around

15% lower if compared with the expectation rate. This deficit is so-called *Gallium anomaly* [69, 70].

3. the **deficit** of detected electron antineutrinos in short-baseline reactor experiments, like ILL [71], Gösgen [72], Krasnoyarsk [73, 74, 75], Rovno [76, 77], Bugey-3/-4 [78, 79], SRP [80], NEOS [81] and DANSS [82]. The expected flux of electron antineutrinos is computed in the studies of the Uranium and Plutonium decay chains inside the nuclear reactors. The observed number of electron antineutrino events in these reactors if compared with the predictions is in average 6% lower. This deficit is so-called *Reactor anomalies* [83].

In the context of neutrino oscillations, a way to address these unexpected results is to add an extra neutrino mass state along with an extra neutrino non-flavored state that could participate in oscillations, but without weak interactions, i.e. a sterile neutrino<sup>4</sup>. We will introduce this new model, named 3+1, in the next Subsection.

### 1.3.1 Adding an Extra Neutrino in the Mixing: the 3+1 Model

Following the same procedure as done in Subsection 1.2.1, in the 3+1 model, we add a fourth neutrino  $\nu_s$  that does not interact via weak forces, but participate in the neutrino mixing. Also, we add a fourth neutrino mass state  $\nu_4$  so that

$$|\nu_\gamma\rangle = \sum_{m=1}^4 U'_{\gamma m} |\nu_m\rangle \quad (\gamma = e, \mu, \tau, s; \quad U'U'^\dagger = \mathbb{1}) \quad (1.30)$$

or

$$|\nu_m\rangle = \sum_{\gamma=e,\mu,\tau,s} U'_{\gamma m} |\nu_\gamma\rangle, \quad (m = 1, 2, 3, 4) \quad (1.31)$$

and the unitary mixing matrix  $U'$ <sup>5</sup> will be parameterized with six mixing angles  $\omega_{mn}$ , ( $m, n = 1, 2, 3, 4$  and  $m \neq n$ ) and three Dirac CP-violation phases  $\epsilon_i$  ( $i = 1, 2, 3$ )<sup>6</sup>. One choice to explicitly write  $U'$  is shown in Eq. 1.32.

---

<sup>4</sup>The mandatory sterile characteristic of the extra neutrinos in the neutrino mixing comes from experimental bounds due to Z boson decay width in the LEP Collider at CERN. The number of neutrinos that participate in the weak interaction was constrained to three [84, 27]. Hence, the three Standard Model neutrinos are so-called “active neutrinos”

<sup>5</sup>We will use the  $U'$  to denote the  $4 \times 4$  unitary matrix to distinguish it of the three neutrino scenario  $U_{\text{PMNS}}$  one. In the next Chapters, we will write the matrix  $U'$  as  $U$ .

<sup>6</sup>For Majorana neutrinos, we will also have three Majorana phases in the mixing, but once they do not participate in the oscillations, we will not explicit them here.

$$\begin{aligned}
U' &= \begin{pmatrix} U'_{e1} & U'_{e2} & U'_{e3} & U'_{e4} \\ U'_{\mu1} & U'_{\mu2} & U'_{\mu3} & U'_{\mu4} \\ U'_{\tau1} & U'_{\tau2} & U'_{\tau3} & U'_{\tau4} \\ U'_{s1} & U'_{s2} & U'_{s3} & U'_{s4} \end{pmatrix} \tag{1.32} \\
&= \begin{pmatrix} 1 & 0 & 0 & 0 \\ 0 & 1 & 0 & 0 \\ 0 & 0 & \cos \omega_{34} & \sin \omega_{34} \\ 0 & 0 & -\sin \omega_{34} & \cos \omega_{34} \end{pmatrix} \begin{pmatrix} 1 & 0 & 0 & 0 \\ 0 & \cos \omega_{24} & 0 & \sin \omega_{24} \\ 0 & 0 & 1 & 0 \\ 0 & -\sin \omega_{24} & 0 & \cos \omega_{24} \end{pmatrix} \times \\
&\times \begin{pmatrix} \cos \omega_{14} & 0 & 0 & \sin \omega_{14} e^{-i\epsilon_3} \\ 0 & 1 & 0 & 0 \\ 0 & 0 & 1 & 0 \\ -\sin \omega_{14} e^{i\epsilon_3} & 0 & 0 & \cos \omega_{14} \end{pmatrix} \begin{pmatrix} 1 & 0 & 0 & 0 \\ 0 & \cos \omega_{23} & \sin \omega_{23} & 0 \\ 0 & -\sin \omega_{23} & \cos \omega_{23} & 0 \\ 0 & 0 & 0 & 1 \end{pmatrix} \times \\
&\times \begin{pmatrix} \cos \omega_{13} & 0 & \sin \omega_{13} e^{-i\epsilon_2} & 0 \\ 0 & 1 & 0 & 0 \\ -\sin \omega_{13} e^{i\epsilon_2} & 0 & \cos \omega_{13} & 0 \\ 0 & 0 & 0 & 1 \end{pmatrix} \begin{pmatrix} \cos \omega_{12} & \sin \omega_{12} e^{-i\epsilon_1} & 0 & 0 \\ -\sin \omega_{12} e^{i\epsilon_1} & \cos \omega_{12} & 0 & 0 \\ 0 & 0 & 1 & 0 \\ 0 & 0 & 0 & 1 \end{pmatrix}
\end{aligned}$$

Equivalently the Eq. 1.18, the probability of a neutrino produced with energy  $E$  and an initial flavor  $\nu_\rho$  be detected as a neutrino  $\nu_\gamma$  after traveling a distance  $L$  is

$$\begin{aligned}
P_{\nu_\rho \rightarrow \nu_\gamma}(E, L) &= \delta_{\gamma\rho} - 4 \sum_{m>n} \text{Re} (U'_{\gamma m} U'_{\rho m}{}^* U'_{\gamma n}{}^* U'_{\rho n}) \sin^2 \left( \frac{m_n^2 - m_m^2 L}{4E} \right) \tag{1.33} \\
&+ 2 \sum_{m>n} \text{Im} (U'_{\gamma m} U'_{\rho m}{}^* U'_{\gamma n}{}^* U'_{\rho n}) \sin \left( \frac{m_n^2 - m_m^2 L}{2E} \right).
\end{aligned}$$

In the short-baseline configuration, as we discussed before, the oscillation frequencies driven by  $\Delta m_{21}^2$  and  $|\Delta m_{32}^2|$  do not develop significant oscillations, i.e.,  $1.27(\Delta m_{21}^2 L/E) < 1$  and  $(1.27|\Delta m_{32}^2|L/E) < 1$ , and can be ignored. This is known as the *short-baseline approximation*. In this regime, the oscillation probability in Eq. 1.33 is dramatically reduced in

$$P_{\nu_\rho \rightarrow \nu_\rho}^{\text{SB}}(E, L) = 1 - 4|U'_{\rho 4}|^2(1 - |U'_{\rho 4}|^2) \sin^2 \left( \frac{m_4^2 - m_1^2 L}{4E} \right) \quad (\rho = \gamma) \tag{1.34}$$

$$P_{\nu_\rho \rightarrow \nu_\gamma}^{\text{SB}}(E, L) = 4|U'_{\rho 4}|^2|U'_{\gamma 4}|^2 \sin^2 \left( \frac{m_4^2 - m_1^2 L}{4E} \right) \quad (\rho \neq \gamma) \tag{1.35}$$

where the new oscillation phase should be driven by  $\Delta m_{41}^2 \simeq 1 \text{ eV}^2$  or larger. We will go back to the Eq. 1.34 and Eq. 1.34 again in Chapter 2 and Chapter 3. The addition of the new, larger oscillation frequency can induce flavor transition in both appearance and disappearance channels in short-baseline experiments. In the 3+1 model, the short-baseline anomalies described in Sec. 1.3 may be explained in terms of muon (anti)neutrino

conversion to electron (anti)neutrino ( $P_{\nu_{\mu} \rightarrow \nu_e}^{\text{SB}(-)}$ ) - explaining the excess of events observed in LSND and MiniBooNE - and the electron (anti)neutrino disappearance ( $P_{\nu_e \rightarrow \bar{\nu}_e}^{\text{SB}(-)}$ ) - accounting for the Gallium and reactor anomalies. Taking a look at these oscillation probabilities, we have

$$P_{\nu_{\mu} \rightarrow \nu_e}^{\text{SB}(-)}(E, L) = 4|U'_{\mu 4}|^2|U'_{e 4}|^2 \sin^2(1.27\Delta m_{41}^2 L/E) \quad (1.36)$$

$$P_{\nu_e \rightarrow \nu_e}^{\text{SB}(-)}(E, L) = 1 - 4|U'_{e 4}|^2(1 - |U'_{e 4}|^2) \sin^2(1.27\Delta m_{41}^2 L/E) \quad (1.37)$$

$$P_{\nu_{\mu} \rightarrow \nu_{\mu}}^{\text{SB}(-)}(E, L) = 1 - 4|U'_{\mu 4}|^2(1 - |U'_{\mu 4}|^2) \sin^2(1.27\Delta m_{41}^2 L/E). \quad (1.38)$$

If we have  $\nu_{\mu} \rightarrow \nu_e$  appearance at short baselines, it implies both nonzero  $U'_{\mu 4}$  and  $U'_{e 4}$  values to explain the flavor transition. In addition,  $U'_{\mu 4}$  and  $U'_{e 4}$  also control electron and muon neutrino disappearance. Hence, 3+1 model also expects to have muon and electron neutrino disappearance at short-baseline. The reactor and Gallium anomalies can handle electron neutrino disappearance [85], but what about muon neutrino disappearance?

Currently, there are no significant signals to muon neutrino disappearance in the short-baseline regime. In particular, the data from MINOS/MINOS+ [86], IceCube [87] and the Super-Kamiokande [88, 89] experiments put severe constraints in  $U'_{\mu 4}$ , provoking a strong tension between appearance and disappearance measurements in the 3+1 framework [90].

In this manner, we introduced the main topic of this Thesis: the neutrino phenomenology in the short-baseline experiments. Motivated by the short-baseline anomalies, we will explore two new physics scenarios involving sterile neutrinos:

1. The manifestation of Large Extra Dimensions (LED) in the neutrino mixing that leads to new, infinite oscillation frequencies. We studied the capability of the future Short-Baseline Neutrino Program experiment to discriminate the effects of the LED model parameters in Chapter 2;
2. An alternative solution to the short-baseline anomalies is given by introducing the neutrino decay phenomenon. We reevaluate the LSND and MiniBooNE data from the point of view of the decay model as well as the constraints from muon neutrino disappearance in short-baseline. In addition, the sensitivity of the Short-Baseline Neutrino Program was also estimated. This study is in Chapter 3.

Finally, we make our final conclusions in Chapter 4.

## Chapter 2

# Large Extra Dimensions

Neutrino oscillations successfully explain the flavor transitions observed in neutrinos produced in natural sources like the sun's center and the earth's atmosphere and human-made sources like reactors and accelerators. These oscillations are driven by two mass-squared differences,  $\Delta m_{21}^2$  and  $\Delta m_{32}^2$ , at the sub-eV scale. However, longstanding anomalies at short-baselines might imply the existence of new oscillation frequencies at the eV-scale (see Subsec. 1.3.1) and the possibility of this sterile state(s) to mix with the three active neutrinos. One of the many future neutrino programs that are expected to provide a final word on this issue is the Short-Baseline Neutrino (SBN) Program at Fermilab.

In this Chapter, we will describe the main results of our work involving a specific model of Large Extra Dimensions (LED) and its phenomenological consequences in the SBN Program [91]. Large Extra Dimensions arise as an elegant solution to the hierarchy problem [92, 93] and later as a natural explanation of the smallness of neutrino masses if compared to the other Standard Model (SM) fermions.

The hierarchy problem consists of the large discrepancy between aspects of the Electroweak energy scale  $M_{EW} \sim 10^3$  GeV and the Planck scale  $M_{Pl} \sim 10^{19}$  GeV, where gravitational force start being relevant. In other words, there is no consensus why gravity is much weaker than Strong, Weak and Electromagnetic forces. The LED model assumes only the existence of one energy scale  $M_{EW}$ , where gravity would have the same intensity

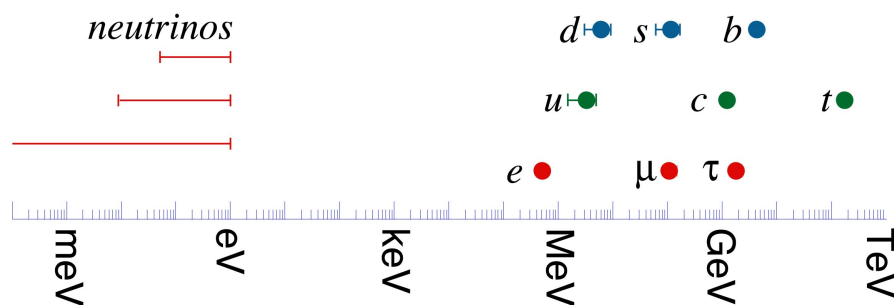


Figure 2.1: Masses of the Standard Model fermions. There is a disparity from six to twelve orders of magnitude between the neutrino and the other fermion masses. LED model arises to address an explanation for the smallness of neutrino masses. Figure taken from Ref. [94].

than the other forces, but it would be suppressed by the presence of extra dimensions. Unlike other particles of the SM, the supposed graviton (mediator of gravitational force) is not constrained in the usual four dimensions space but can freely propagate in these extra dimensions, provoking a dilution of gravity strength.

In analogy to what happens with gravity, we can use the LED model to naturally explain the smallness of neutrinos masses if compared to the other fermions in the SM [95, 96, 97, 98] (Figure 2.1). As already mentioned about the LED model, we have particles with SM gauge symmetries which are associated with a “charge” that needs to be conserved in four dimensions. One example is the electric charge. Hence, these particles: charged leptons, active neutrinos, quarks, gauge bosons and Higgs are confined in a four-dimensional “brane”, which is part of a  $(4 + d)$  - dimensional space, where  $d$  is the number of the (closed, or compacted) extra dimensions. We will refer to the  $(4 + d)$  space as “bulk”. Singlets under this symmetry group do not depend on charge conservation and, therefore, can propagate freely through the bulk. They are: the graviton (weakness of gravity) and, now, three bulk neutrinos without mass, each coupling to a flavor of the active neutrinos (see Figure 2.2).

Moving to context of neutrinos, we will consider the LED model from Ref. [99] (which is based on previous works in Refs. [96, 98, 100]). In summary, the Yukawa couplings between the right-handed bulk neutrinos and the active ones are suppressed by the radius of the extra dimension and neutrinos acquire a Dirac mass that is naturally small. We will

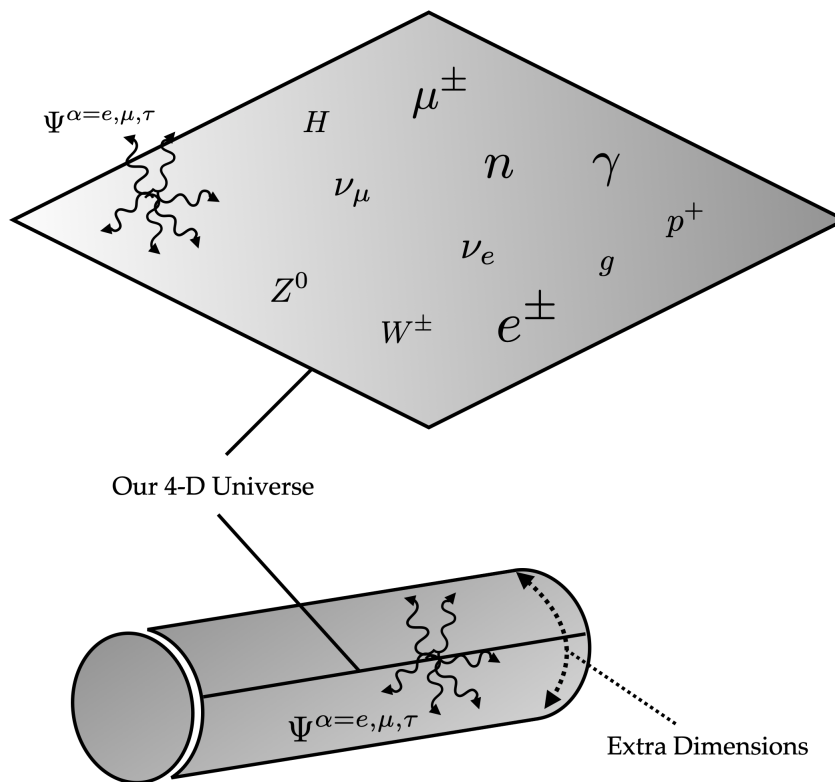


Figure 2.2: Standard Model particles confined in the 4-dimensional “brane” embed in a  $(4 + d)$ -dimensional “bulk”, where gravitons and bulk neutrinos  $\Psi^\alpha$  can freely propagate. Here,  $d$  is the number of the extra dimensions.

describe the formalism of this process in Sec. 2.1. The phenomenological consequence of the extra dimension compactification is the manifestation of infinite neutrino mass states that are connected with flavor states via neutrino mixing (see Sec. 1.2.1). Thus, Large Extra Dimensions would interfere in neutrino oscillations and we can test its effects with neutrino experiments. Previous works were done in this circumstances in the Refs. [101, 102, 103, 104, 105, 106, 107].

Our goal is to establish the sensitivity of the SBN program to neutrino oscillations in the LED model. We started re-creating sensitivity analyses for sterile neutrinos in the 3+1 scenario (see Subsec. 1.3.1), previously done by the SBN collaboration, by simulating neutrino events in the three SBN detectors for both muon neutrino disappearance and electron neutrino appearance. Then, we implemented neutrino oscillations as predicted in the LED model and also we have performed sensitivity analysis to the LED parameters. Finally, we studied the SBN power of discriminating between the two models, the 3+1 and the LED. We have found that SBN is sensitive to the oscillations predicted in the LED model and have the potential to constrain the LED parameter space better than any other oscillation experiment for  $m_1^D < 0.1$  eV. In case SBN observes a departure from the three active neutrino framework (see Subsec. 1.2.1), it also has the power of discriminating between sterile oscillations predicted in the 3+1 framework and the LED ones.

## 2.1 Formalism

In general, it is assumed the bulk neutrinos [99] can propagate in more than four dimensions while the active, left-handed neutrino  $\nu_L$  and the SM Higgs  $H$  are confined to the four-dimensional brane. It is also assumed an asymmetric space where one of the extra dimensions is larger than the others so that effectively it is enough to consider five dimensions in total [98, 96, 99]. We will follow the model with three bulk neutrinos  $\Psi^\alpha$  ( $\alpha = e, \mu, \tau$ ) couple via Yukawa interactions to the three active brane neutrinos, the so-called (3, 3) model in Ref. [99]. The action in the (3, 3) model is given by:

$$\begin{aligned}
S = & \int d^4x dy \bar{\Psi}^\alpha(x, y) \Gamma^A i \partial_A \Psi^\alpha(x, y) \\
& + \int d^4x dy \lambda_{\alpha\beta} \bar{L}^\alpha(x) \tilde{\Phi}(x) \psi_R^\beta(x, y) \delta(y) \\
& + \int d^4x dy \bar{\nu}_L^\alpha(x) \gamma^\mu i \partial_\mu \nu_L^\alpha(x) \delta(y) + \text{H.c.}
\end{aligned} \tag{2.1}$$

where  $y$  is the coordinate of the extra dimension,  $\Gamma^A$  are the five-dimensional Dirac matrices for  $A = 0, \dots, 4$ , which  $\Gamma^4 = i\gamma^5$  and  $\partial_4 = \partial_y$ .  $\lambda_{\alpha\beta}$  are the Yukawa couplings,  $\bar{L}^\alpha(x) = (\bar{\nu}_L^\alpha(x) \quad \bar{\alpha}_L(x))$  are left-handed doublets and  $\tilde{\Phi}(x)$  is the Higgs doublet. The Dirac fermion  $\Psi^\alpha$  in five dimensions is a four-component spinor which can be decomposed in two component spinors (Weyl fermions),  $\psi_L^\alpha$  and  $\psi_R^\alpha$ , where

$$\Psi^\alpha(x, y) = \psi_L^\alpha(x, y) + \psi_R^\alpha(x, y). \tag{2.2}$$

To avoid implications in Newton constant  $G_N$ , which is the gravity coupling we do observe, it is imposed that the extra spatial dimension should be closed or compactified. In our case, we assume that the extra dimension is limited in a circle of radius  $R_{\text{ED}}$ . In this way, the bulk fields (as well as the decomposed Weyl fields) have a periodicity  $\Psi^\alpha(x, y) = \Psi^\alpha(x, y + 2\pi R_{\text{ED}})$  and can be expanded in Fourier series:

$$\Psi(x, y) = \frac{1}{\sqrt{2\pi R_{\text{ED}}}} \psi_0(x) + \frac{1}{\sqrt{\pi R_{\text{ED}}}} \sum_{n=1}^{\infty} \left[ \psi_n(x) \cos\left(\frac{ny}{R_{\text{ED}}}\right) + \hat{\psi}_n(x) \sin\left(\frac{ny}{R_{\text{ED}}}\right) \right] \quad (2.3)$$

The modes  $\psi_n(x)$  and  $\hat{\psi}_n(x)$  in Eq. 2.3 are called Kaluza-Klein (KK) modes. In order to evaluate the effects of the bulk fields in four dimensions, we integrate the action in Eq. 2.1 in the 5-th component  $dy$ . This process is called *dimensional reduction* and brings important LED consequences, which can be summarized in the following:

1. First term of Eq. 2.1, the **bulk kinetic term**: decomposing the bulk field  $\Psi^\alpha(x, y)$  in Weyl components  $\psi_L^\alpha(x, y)$  and  $\psi_R^\alpha(x, y)$  (Eq. 2.2), expand them in Fourier series of Eq. 2.3 and integrate in  $dy$ , we will obtain

$$\int d^4x \left[ \text{KK kinetic terms} + \left( \sum_{n=1}^{\infty} \frac{n}{R_{\text{ED}}} \overline{\psi_{n,L}^\alpha(x)} \psi_{n,R}^\alpha(x) + \text{H.c.} \right) \right], \quad (2.4)$$

where we consider that the KK modes from even and odd fermionic fields from Fourier expansion are not distinguishable:  $\psi_n(x) = \hat{\psi}_n(x)$ . The second term of Eq. 2.4 has the form of Dirac masses of the excited modes. So the first consequence of LED manifestation is the creation of infinite neutrino mass states in our 4-dimensional world;

2. Second term of Eq. 2.1, the **Yukawa interaction between bulk and active neutrinos**: notice that the active neutrinos from the left-handed doublet  $L^\alpha(x)$  only couples with right-handed Weyl component  $\psi_R^\alpha(x, y)$  of the bulk neutrinos. Performing the dimensional reduction and considering the Higgs doublet in the unitary gauge

$$\tilde{\Phi}(x) = \frac{1}{\sqrt{2}} \begin{pmatrix} v + H(x) \\ 0 \end{pmatrix} \quad (2.5)$$

where  $v$  is vacuum expected value (VEV), the second term of Eq. 2.1 becomes

$$\int d^4x \frac{(v + H(x))}{\sqrt{2}} \frac{\lambda_{\alpha\beta}}{\sqrt{2\pi R_{\text{ED}}}} \overline{\nu_L^\alpha(x)} \left( \psi_{0,R}^\beta(x) + \sqrt{2} \sum_{n=1}^{\infty} \psi_{n,R}^\beta(x) \right) + \text{H.c.} \quad (2.6)$$

In this interaction, the Yukawa coupling  $\lambda_{\alpha\beta}$  has dimension of energy $^{-1/2}$ . To ensure the dimensionless Yukawa coupling, we introduce the quantity  $h_{\alpha\beta} = \lambda_{\alpha\beta} \sqrt{M_{\text{EW}}}$  in

function of the only mass scale  $M_{\text{EW}}$  in the LED model. Finally, the Dirac mass terms arising from the interaction between bulk and active neutrinos are:

$$\int d^4x m_{\alpha\beta}^D \bar{\nu}_L^\alpha(x) \left( \psi_{0,R}^\beta(x) + \sqrt{2} \sum_{n=1}^{\infty} \psi_{n,R}^\beta(x) \right) + \text{H.c.} \quad (2.7)$$

where the coupling  $m_{\alpha\beta}^D = \frac{v}{\sqrt{2}} \frac{h_{\alpha\beta}}{\sqrt{2\pi R_{\text{ED}} M_{\text{EW}}}}$  are the Dirac neutrino masses (in flavor basis). Notice another important result from LED model: both the mass terms from Eq. 2.7 and Eq. 2.4 are suppressed by the radius of the extra dimension  $R_{\text{ED}}$ ;

3. Third term of Eq. 2.1, the **active neutrino kinetic term**: as active neutrinos only populate the brane, we obtain the usual kinetic term by performing the dimensional reduction:

$$\int d^4x \bar{\nu}_L^\alpha(x) \gamma^\mu i \partial_\mu \nu_L^\alpha(x) + \text{H.c.} \quad (2.8)$$

Therefore, the Lagrangian mass terms that result from Eq. 2.1 are given by:

$$\mathcal{L}_{\text{mass}} = \sum_{n=1}^{\infty} \frac{n}{R_{\text{ED}}} \overline{\psi_{n,L}^\alpha} \psi_{n,R}^\alpha + m_{\alpha\beta}^D \bar{\nu}_L^\alpha \left( \psi_{0,R}^\beta + \sqrt{2} \sum_{n=1}^{\infty} \psi_{n,R}^\beta \right) + \text{H.c.} \quad (2.9)$$

Notice that the mass Lagrangian in Eq. 2.9 is not diagonal, which means that we will need to find the true neutrino mass states from LED model. We will proceed in two steps: first, we consider a basis in which the Dirac mass is diagonal [99]  $U^\dagger m^D r = \text{diag}\{m_i^D\}$  by defining the following transformations

$$\nu_L^\alpha = U^{\alpha i} \nu_L^i \quad (2.10)$$

$$\psi_{n,L}^\alpha = r^{\alpha i} \psi_{n,L}^i, \quad n = 1, \dots, \infty \quad (2.11)$$

$$\psi_{n,R}^\alpha = r^{\alpha i} \psi_{n,R}^i, \quad n = 0, 1, \dots, \infty \quad (2.12)$$

where  $U$  and  $r$  are unitary matrices and ( $i = 1, 2, 3$ ). Notice that in Eq. 2.10 we have the standard neutrino mixing among flavor and mass states, i.e.,  $U \equiv U_{\text{PMNS}}$  (see Sec. 1.2.1). Hence, the Lagrangian in Eq. 2.9 becomes

$$\begin{aligned} \mathcal{L}_{\text{mass}} = & \sum_{n=1}^{\infty} \frac{n}{R_{\text{ED}}} \overline{\psi_{n,L}^i} \left[ (r^\dagger)^{i\alpha} r^{\alpha j} \right] \psi_{n,R}^j \\ & + \bar{\nu}_L^i \left[ (U^\dagger)^{i\alpha} m_{\alpha\beta}^D r^{\beta j} \right] \left( \psi_{0,R}^j + \sqrt{2} \sum_{n=1}^{\infty} \psi_{n,R}^j \right) + \text{H.c.}, \end{aligned} \quad (2.13)$$

in which we have  $\left[ (r^\dagger)^{i\alpha} r^{\alpha j} \right] = \delta_{ij}$  and  $\left[ (U^\dagger)^{i\alpha} m_{\alpha\beta}^D r^{\beta j} \right] = m_i^D \delta_{ij}$ . Second, we organize the resulting states from Eq. 2.13 in the matricidal form  $\bar{\nu}_R^i M^i \nu_L^i$  (plus H.c.), where

$$\nu_R^i = (\psi_{0,R}^i \quad \psi_{1,R}^i \quad \psi_{2,R}^i \quad \dots)^T \quad (2.14)$$

$$\nu_L^i = (\nu_L^i \quad \psi_{1,L}^i \quad \psi_{2,L}^i \quad \dots)^T \quad (2.15)$$

$$M^i = \begin{pmatrix} m_i^D & \sqrt{2}m_i^D & \sqrt{2}m_i^D & \sqrt{2}m_i^D & \dots \\ 0 & 1/R_{\text{ED}} & 0 & 0 & \dots \\ 0 & 0 & 2/R_{\text{ED}} & 0 & \dots \\ \vdots & \vdots & \vdots & \vdots & \ddots \end{pmatrix}. \quad (2.16)$$

Obviously, the states we just defined  $\nu_{nR}^i, \nu_{nL}^i$  ( $n = 0, 1, \dots, \infty$ ) are not the true neutrino mass states in the LED model. However, this ‘‘pseudo’’ mass basis is directly related with neutrino flavor basis, in which neutrino experiments can search for mechanisms of flavor transition. If we rewrite Eq. 2.10 (with explicit sum)

$$\nu_L^\alpha = \sum_{i=1}^3 U^{\alpha i} \nu_{0L}^i \quad (2.17)$$

it is possible to express the flavor states in terms of the true, KK neutrinos masses. To do this, we will define the following linear combination

$$\nu_{kL}^i = \sum_{n=0}^{\infty} S_{kn}^i \mathcal{N}_{nL}^i \quad (2.18)$$

where  $\mathcal{N}_{nL}^i$  are the KK neutrino mass eigenstates predicted by the LED model and  $S^i$  is an unitary matrix. We can find the true mass eigenvalues by diagonalizing  $M^i M^{i\dagger}$  in the form  $S^i M^i M^{i\dagger} S^{i\dagger}$ . Appealing for linear algebra, the characteristic equation obtained in the determinant calculation  $\det[M^i M^{i\dagger} - (\lambda_i/R_{\text{ED}})^2] = 0$  is [97]

$$\lambda_i^{(n)} - \pi (R_{\text{ED}} m_i^D)^2 \cot(\pi \lambda_i^{(n)}) = 0, \quad (2.19)$$

where  $\lambda_i^{(n)}/R_{\text{ED}}$  ( $n = 0, 1, \dots, \infty$ ) are the mass eigenvalues. The roots  $\lambda_i^{(n)}$  from Eq. 2.19 are constrained such that they belong to the range  $[n, n + 1/2]$  [96]. We can obtain the elements of  $S^i$  matrix by calculating

$$\sum_{k'=1}^{\infty} \sum_{m'=1}^{\infty} \sum_{n'=1}^{\infty} (S^i)_{kk'} (M^i)_{k'm'} (M^{i\dagger})_{m'n'} (S^{i\dagger})_{n'n} = \frac{\lambda_i^{(k)}}{R_{\text{ED}}} \delta_{kn} \quad (2.20)$$

and comparing each element of the left-side matrix to the eigenvalues in the diagonal of the right-side matrix. We find the subsequent relations

$$(S_{0n}^i)^2 = \frac{2}{1 + \pi^2 (R_{\text{ED}} m_i^D)^2 + \left[ \lambda_i^{(n)} / (R_{\text{ED}} m_i^D) \right]^2} \quad (2.21)$$

$$S_{kn}^i = \frac{k\sqrt{2}R_{\text{ED}}m_i^D}{(\lambda_i^{(n)})^2 - k^2} S_{0n}^i. \quad (2.22)$$

Effectively, the active neutrino flavor states can be finally written in terms of the mass eigenstates (as composed of the KK  $n$ -modes of the fermion field), as follows:

$$\nu_L^\alpha = \sum_{i=1}^3 U^{\alpha i} \nu_{0L}^i = \sum_{i=1}^3 \sum_{n=0}^{\infty} U^{\alpha i} S_{0n}^i \mathcal{N}_{nL}^i \quad (2.23)$$

In order to make a physical sense of the formalism, one should assume that *the most active state is obtained for  $n = 0$* . Additionally, if we go to the limit  $R_{\text{ED}} m_i^D \ll 1$  then  $\lambda_i^{(0)}/R_{\text{ED}} \rightarrow m_i^D$ , and following Eq. (2.21)  $S_{00}^i \rightarrow 1$ , therefore recovering the standard result in Eq. 2.10 where  $U^{\alpha i}$  is the lepton mixing matrix that is usually parametrized by three rotations, through the three mixing angles  $\theta_{ij}$ , and the Dirac CP phase  $\delta$  (see Sec. 1.2.1). The Figure 2.3 illustrates the behavior of the  $S_{0n}^1$  in function of  $m_1^D$  with  $R_{\text{ED}}$  fixed in  $0.5 \text{ eV}^{-1}$ : for values of  $m_1^D R_{\text{ED}} \ll 1$ , the flavor transition effects depend mostly of the usual active states. When  $m_1^D R_{\text{ED}} \approx 1$ , the higher-order states affect the mixing democratically.

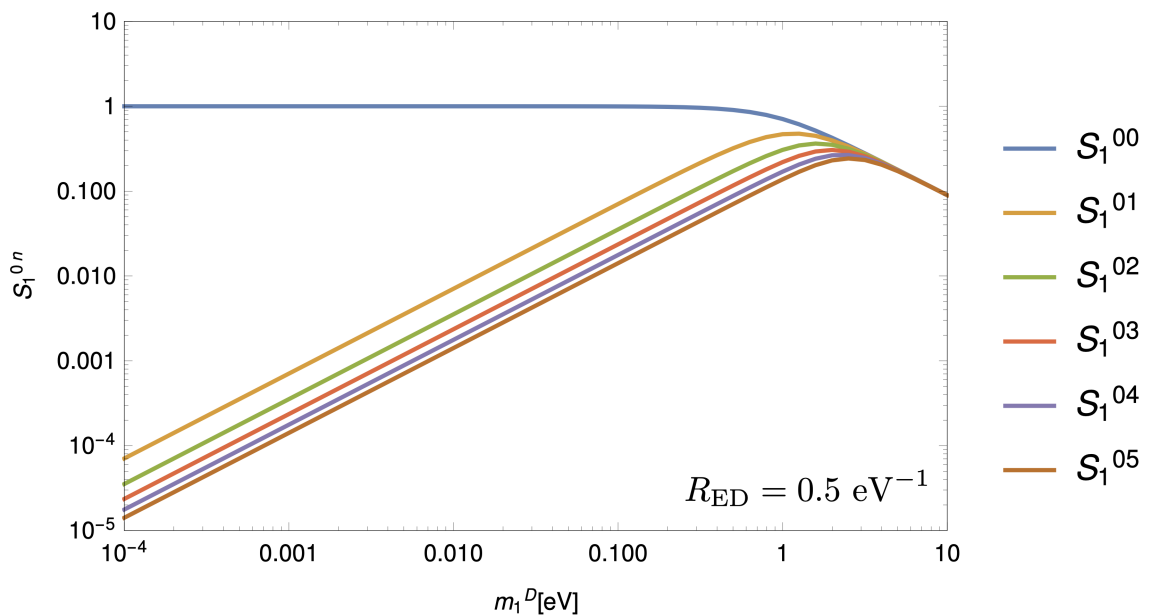


Figure 2.3: The behavior of the  $S_{0n}^1$  as a function of  $m_1^D$ , assuming  $R_{\text{ED}} = 0.5 \text{ eV}^{-1}$ . Considering the terms of order  $n = 0$  as the most active states, the higher orders of the Kaluza-Klein modes will considerably affect the mixing when  $m_1^D R_{\text{ED}} \approx 1$ .

Assuming the mostly active mass state is related to the lightest mass state in the KK-tower, it implies a relation among the eigenvalues of this LED framework, obtained by Eq. 2.19, with the mass-squared differences obtained in the three-neutrino case. This relation can be written, considering the normal mass ordering, as:

$$\frac{\left(\lambda_k^{(0)}\right)^2 - \left(\lambda_1^{(0)}\right)^2}{R_{\text{ED}}^2} = \Delta m_{k1}^2 \quad (2.24)$$

with  $\Delta m_{k1}^2$  ( $k = 2, 3$ ) the mass-squared differences. Therefore, the existing values on the

mass-squared differences of the active neutrino mass eigenstates  $\Delta m_{k1}^2$ , Ref. [108, 109], constrain the parameter space  $(m_1^D, R_{\text{ED}}^{-1})$  of the LED model. Thus, a good strategy is to use this information before scanning the parameter space. Basically,  $\lambda_1^{(0)}$  is fixed by the  $m_1^D$  in Eq. 2.19, and using Eq. 2.24 for  $k=2,3$  we determine  $\lambda_k^{(0)}$  and with this last result  $m_k^D$  is determined, from the use of Eq. 2.19, while compatible with Eq. 2.24 as done in Ref. [103]. With these constraints, we have now only two independent parameters  $m_1^D$  and  $R_{\text{ED}}$  that we will rename from now on as  $m_1^D \rightarrow m_0$  for normal mass ordering. Figure 2.4 illustrates the three most active neutrino masses  $\lambda_i^{(0)}$  in function of Dirac mass  $m_1^D$ , with  $R_{\text{ED}} = 0.5 \text{ eV}^{-1}$ . Notice that when  $m_1^D R_{\text{ED}} \approx 1$ , the masses become degenerated. Similarly, one can follow the same procedure for the inverted mass ordering, and this case, the two independent parameters are  $m_3^D \rightarrow m_0$  and  $R_{\text{ED}}$ . In the cases where the condition in Eq. 2.24 is not fulfilled by the  $(m_0, R_{\text{ED}}^{-1})$  combination, we quoted the excluded region as *excluded by mass-squared differences constraints*. We will come back to this point in Section 2.2.

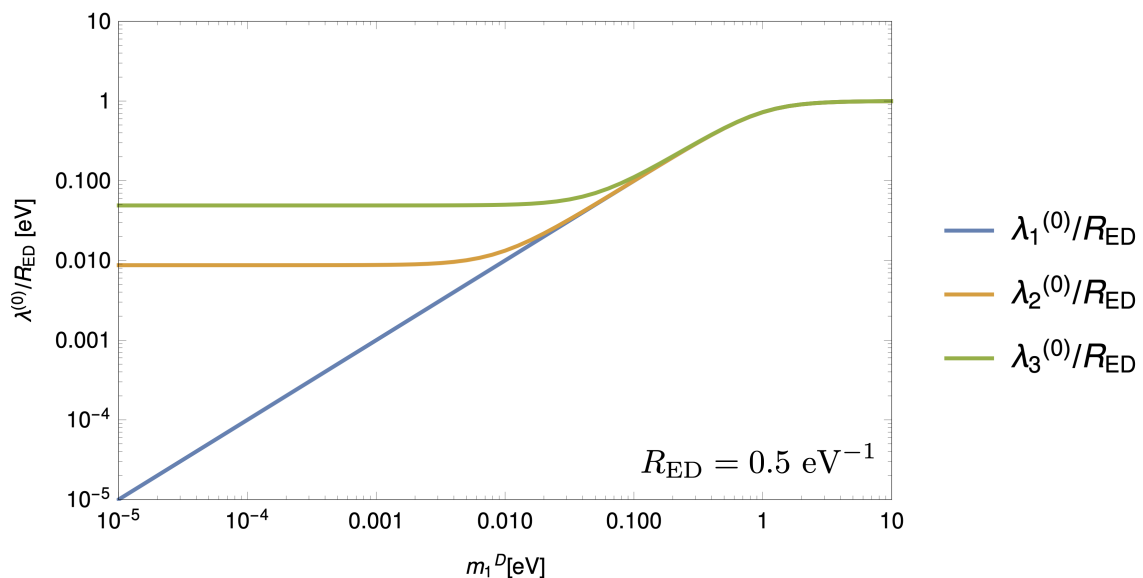


Figure 2.4: The three most active neutrino masses  $\lambda_i^{(0)}$  in function of Dirac mass  $m_1^D$ , with  $R_{\text{ED}} = 0.5 \text{ eV}^{-1}$  for the normal mass ordering. When  $m_1^D R_{\text{ED}} \approx 1$ , the mass values become degenerated.

In the LED framework the neutrino mixing matrix elements  $U^{\alpha i} S_{0n}^i$ , as defined in Eq. 2.23, is in general different to the standard three neutrino mixing matrix  $U^{\text{PMNS}}$ . To avoid spoiling the neutrino oscillations observations, condensed in part as constraints on the mixing angles  $\theta_{ij}$  ( $i, j = 1, 2, 3$ ) in *scenario of three-neutrino scheme* (with values in Ref. [110, 108, 109]), the mixing angles in the LED framework have to be redefined. Following the procedure from Ref. [106] we have defined *new* mixing angles  $\phi_{ij}$  ( $i, j = 1, 2, 3$ ) in the LED scenario such that the lowest mass state in KK tower,  $n = 0$ , have the  $U^{\alpha i} S_{00}^i$  amplitude equal to the numerical value of the standard PMNS matrix elements (see Sec. 1.2.1). From this relation we can get the mixing angles in the LED framework,  $\phi_{ij}$ , related with the mixing angles,  $\theta_{ij}$ . Explicitly, we have used the mixing matrix

elements  $|U_{e2}^{\text{PMNS}}|$ ,  $|U_{e3}^{\text{PMNS}}|$  and  $|U_{\mu 3}^{\text{PMNS}}|$  such that

$$\begin{aligned} \sin \phi_{13} &= \frac{\sin \theta_{13}}{(L_3^{00})} & \cos \phi_{13} \sin \phi_{12} &= \frac{\cos \theta_{13} \sin \theta_{12}}{(L_2^{00})} \\ \cos \phi_{13} \sin \phi_{23} &= \frac{\cos \theta_{13} \sin \theta_{23}}{(L_3^{00})}. \end{aligned} \quad (2.25)$$

From now on, the mixing angles  $\phi_{ij}$  in the LED formalism are given by the values in Eq. 2.25. For some values of  $m_i^D$  and  $R_{\text{ED}}$  the  $S_{00}^i$  value can be smaller than the numerator in Eq. 2.25 such that  $\sin \phi_{ij} > 1$  and thus unphysical. In this way, values of  $m_i^D$  and  $R_{\text{ED}}$  that result in this unphysical  $\phi_{ij}$  will be disregarded and we have quoted them as *excluded by mixing angle constraints*. We will come back to this point in Section 2.2.

In the presence of LED, the relations in Eq. 2.24 and Eq. 2.25 give the mass-squared differences and the mixing angles in terms of the standard oscillation parameters. When simulating neutrino event rates to perform the different studies along this Chapter, we used the best-fit values for the oscillation parameters in the standard three-neutrino framework presented in Nu-Fit 3.2 (2018) [108, 109]. Despite the complex formalism, the LED model has only two extra parameters that control the mixing among all the infinite mass states. They are the lightest neutrino mass  $m_0$  (for normal ordering  $m_0 = m_1^D$  while for inverted ordering  $m_0 = m_3^D$ ) and the radius of extra dimension  $R_{\text{ED}}$ .

## 2.2 The Short-Baseline Neutrino Program

The Short-Baseline Neutrino Program, or SBN, experimental proposal will align three liquid Argon detectors in the central axis of the Booster Neutrino Beam (BNB), located at Fermilab [111]. Table 2.1 gives the SBN detector names, active masses, and their distances from BNB target. The neutrino detection occurs via charged-current (CC) interactions with liquid Argon, where charged particles ( $\mu^\pm$  and  $e^\pm$ ) and scintillation light are produced. Such charged particles ionize the argon, and the created charges are drifted by an uniform electric field to the anode plaques and collected by wire planes. Depending on the time of arrival of the charges to the wires, and the amount of charge produced in liquid Argon along the path of  $\mu^\pm$  and  $e^\pm$ , it is possible to reconstruct the topological profile of the interactions generated by the neutrinos, i.e., it is possible to recognize which particles participate in such interactions. Figure 2.5 illustrates the SBN layout and the event display from an electron ‘shower’ or a muon ‘track’ inside the detectors.

Detector	Active Mass	Distance from BNB target
SBND	112 t	110 m
MicroBooNE	89 t	470 m
ICARUS-T600	476 t	600 m

Table 2.1: SBN detector active masses and distances from the local of the neutrino production.

Muon-like events have ‘track’ topology because they are massive enough to not suffer considerable deflections during the liquid Argon ionization process. Electron-like events, on the other hand, suffer multiple deflections and form the ‘shower’ pattern. Photons produced as the result of neutrino neutral-current interactions also hold the shower topology. These photons constitute the main source of the neutrino events’ background. To select electron-like events among all the induced showers in the target, the SBN detectors are capable to record the energy deposition of the particles and discriminate them via calorimetric analysis.

According to the proposal [111], the SBN Program is designed to address several anomalies in neutrino physics and will test, with the most sensitivity, the oscillation-interpretation to LSND and MiniBooNE data (see Subsec. 1.3 and Sec. 3.3). SBN will start taking data on its full configuration (MicroBooNE is an active detector and ICARUS installation is already completed) on late 2021/beginning of 2022. Based on that, we want to investigate the potential of SBN to search for hints of flavor oscillation leaded by the KK mass modes from LED model. Therefore, considering the mixing among the neutrino flavor states and KK mass states from Eq. 2.23, the probability of a neutrino  $\alpha$ -flavored  $\nu_\alpha$  with energy  $E_\nu$  be detected as a neutrino  $\beta$   $\nu_\beta$ , ( $\alpha, \beta = e, \mu, \tau$ ) after travels a distance  $L$  is given by

$$P_{\nu_\alpha \rightarrow \nu_\beta}^{\text{LED}} = |\langle \nu_\beta(L) | \nu_\alpha \rangle|^2 = \left| \sum_{i=1}^3 U^{\alpha i} U^{\beta i*} \sum_{n=0}^{\infty} (S_{0n}^i)^2 \exp \left[ i \frac{\lambda_i^{(n)2} L}{2E_\nu R_{\text{ED}}^2} \right] \right|^2 \quad (2.26)$$

In Figure 2.6, the behavior of the oscillation probability for different  $m_0$  and  $R_{\text{ED}}$  values is shown, considering an  $L/E_\nu$  of 1.2 km/GeV in both appearance and disappearance

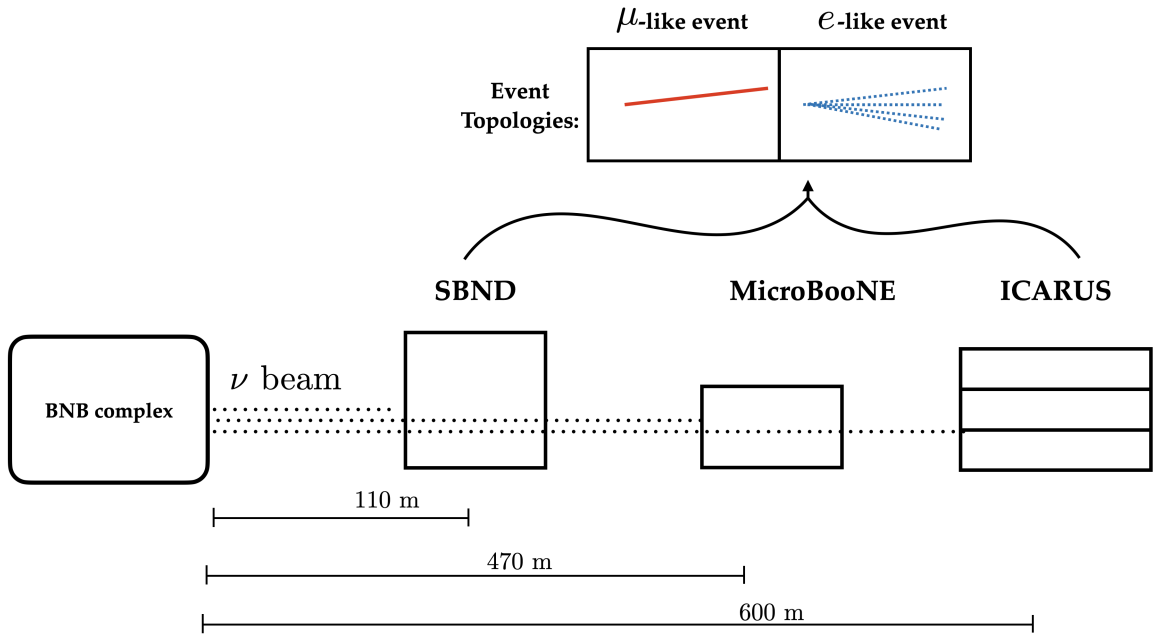


Figure 2.5: SBN layout with the three liquid Argon detectors placed along the central axis of BNB complex plus the event display of electron or muon interaction inside the liquid Argon.

channels for both normal and inverted neutrino mass ordering. The  $L/E_\nu$  value was calculated using the ICARUS baseline  $L = 0.6$  km and the energy  $E_\nu = 0.5$  GeV, which corresponds to the region in the neutrino energy spectrum where most of the events are expected [111]. We noticed that for all LED parameters in the  $R_{\text{ED}}^{-1} - m_0$  plane, the appearance probability is not larger than  $10^{-3}$  and almost all survival probability is larger than 0.9. The gray shaded region is excluded by neutrino oscillation data, with the relations Eq. 2.24 and Eq. 2.25, as described in Section 2.1.

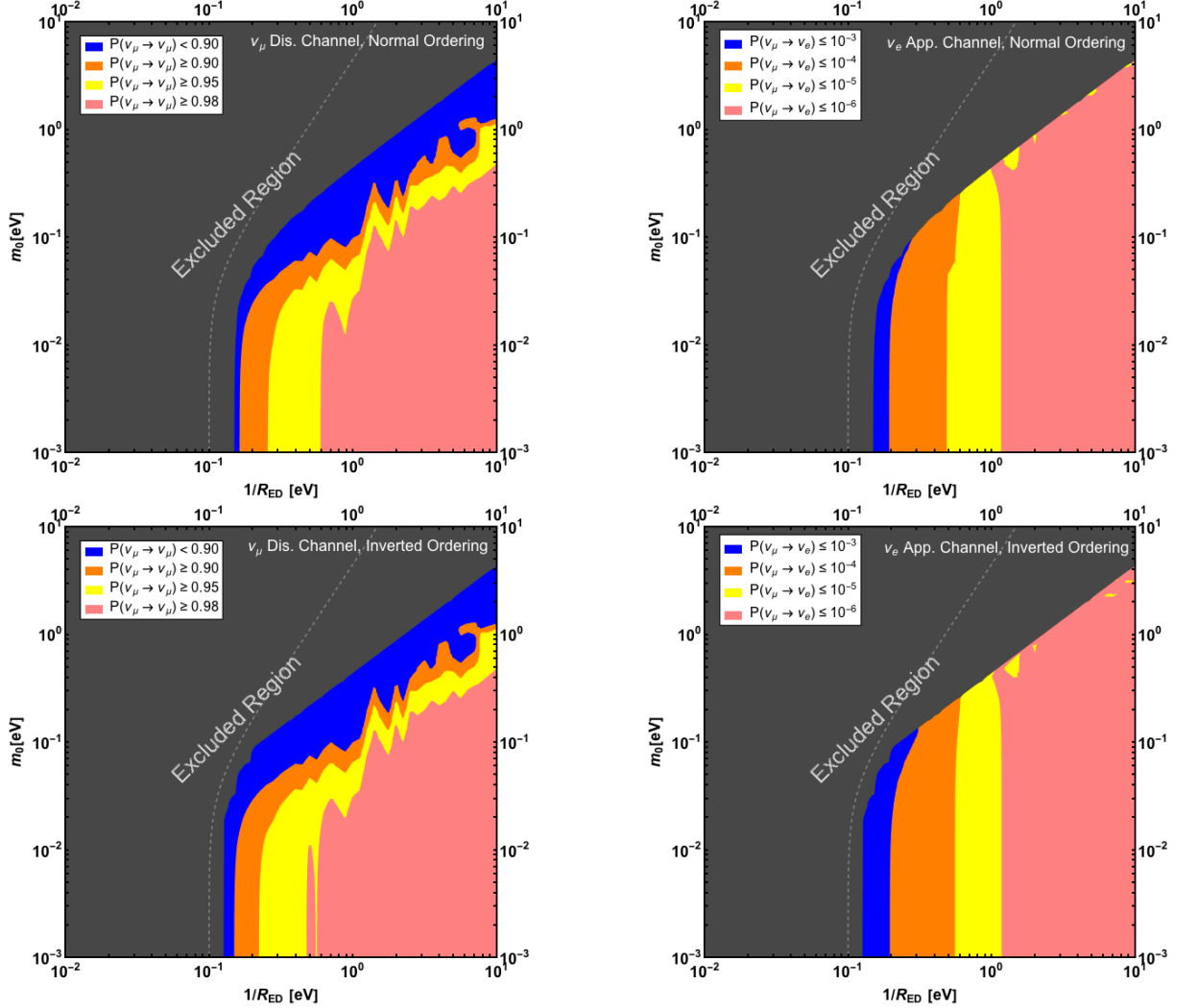


Figure 2.6: Probability regions for different values of LED parameters,  $m_0$  and  $R_{\text{ED}}$ . In the left (right) panels we have  $\nu_\mu \rightarrow \nu_\mu$  ( $\nu_\mu \rightarrow \nu_e$ ). In the top (bottom) panel we show the normal (inverted) ordering. We chose here a typical short-baseline  $L/E_\nu$  of 1.2 km/GeV, see text for details, and we compute probabilities using the first 40 KK modes. The gray shaded region is excluded due to neutrino oscillation data (see Sec.2.1).

In order to perform the SBN sensitivity analysis under LED assumption, we computed the expected number of events at the SBN facility by implementing the detectors in the GLOBES [112, 113] c-library, following the proposal description. In this way, consider a neutrino experiment that searches for flavor transition mechanism in a channel  $c$  ( $\nu_\mu \rightarrow \nu_e$  or  $\nu_\mu \rightarrow \nu_\mu$ , for example) and the energy range of data acquisition of this experiment is

divided (or binned) in  $\eta$  intervals or *bins*. The number of neutrino events per energy bin  $a$  ( $a = 1, \dots, \eta$ ) in channel  $c$  is given by:

$$n_a^c = N \epsilon_a^c \int_{E_a - \Delta E_a/2}^{E_a + \Delta E_a/2} dE' \int_0^\infty dE \phi^c(E) P^c(E) \sigma^c(E) R^c(E, E'), \quad (2.27)$$

where  $E$  is the true neutrino energy,  $E'$  is the reconstructed neutrino energy by the detector,  $N$  is a normalization factor related to unit conversions,  $\epsilon_a^c$  is the bin energy efficiency,  $\phi^c(E)$  is the predicted neutrino flux of the initial flavor at the detector,  $P^c(E)$  is the model dependent neutrino flavor transition probability,  $\sigma^c(E)$  is the total cross-section of the neutrino interaction with the detector target material,  $R^c(E, E')$  describes the energy response of the detector. It is also called *energy resolution function* and  $E_a$  is the central value of the  $a$ th energy bin and  $\Delta E_a$  is the bin size.

The SBN facility will search for oscillations in two channels: 1) *electron neutrino appearance* from muon neutrino conversion ( $\nu_\mu \rightarrow \nu_e$ ) and 2) *muon neutrino disappearance* ( $\nu_\mu \rightarrow \nu_\mu$ ) from muon neutrino survival. We will define the components of Eq. 2.27 for each one of the SBN oscillation channels as follows:

### 1. Muon neutrino disappearance channel:

- *Signal*: Survival of muon neutrinos ( $\nu_\mu \rightarrow \nu_\mu$ ) from the beam which interact with liquid argon through weak CC producing muons in the detectors. The event rate for this channel sign is given by

$$n_a^{\nu_\mu \rightarrow \nu_\mu} = N_\mu \epsilon_a^{\nu_\mu} \int_{E_a - \Delta E_a/2}^{E_a + \Delta E_a/2} dE' \int_0^\infty dE \phi_{\nu_\mu}(E) P_{\nu_\mu \rightarrow \nu_\mu}^{\text{LED}}(E) \times \sigma_{\nu_\mu \rightarrow \text{Ar}}(E) R^\mu(E, E') \quad (2.28)$$

where ( $a = 1, \dots, 19$ ), the fluxes  $\phi_{\nu_\mu}(E)$  for the three detectors was taken from Ref. [114] and the neutrino-argon cross section  $\sigma_{\nu_\mu \rightarrow \text{Ar}}(E)$  was taken from inputs to GLOBES prepared for Deep Underground Neutrino Experiment (DUNE) simulation [115], with the cross section inputs originally generated using GENIE 2.8.4 [116].  $P_{\nu_\mu \rightarrow \nu_\mu}^{\text{LED}}(E)$  is given in Eq. 2.26 and the energy resolution function  $R^\mu(E, E')$  is a Gaussian in the form

$$R^\mu(E, E') = \frac{1}{\sigma'(E)\sqrt{2\pi}} e^{-\frac{(E-E')^2}{2\sigma'^2(E)}} \quad (2.29)$$

with width of  $\sigma'(E) = 6\%/\sqrt{E[\text{GeV}]}$ , according to Ref. [117]. The energy range for the neutrino event reconstruction extends from 0.2 GeV to 3 GeV where each channel has different bin widths, as described in the Table 2.2. After event reconstruction, we included an efficiency factor for each bin in order to mimic event rates from the SBN technical draft [111] as following

Detector	SBND	MicroBooNE	ICARUS-T600
$N_\mu$	$5.39 \times 10^{-5}$	$4.39 \times 10^{-4}$	$1.61 \times 10^{-3}$
$\epsilon^{\nu_\mu}$	[0.17, 0.13, 0.12, 0.10, 0.09, 0.08, 0.08, 0.07, 0.06, 0.06, 0.05, 0.05, 0.04, 0.04, 0.04, 0.03, 0.03, 0.03]	[0.06, 0.05, 0.04, 0.04, 0.03, 0.03, 0.03, 0.03, 0.02, 0.02, 0.02, 0.02, 0.02, 0.02, 0.02, 0.01, 0.01, 0.02, 0.02]	[0.05, 0.04, 0.03, 0.03, 0.03, 0.03, 0.02, 0.02, 0.02, 0.02, 0.02, 0.02, 0.02, 0.02, 0.01, 0.01, 0.01, 0.01, 0.02]

- *Background:* The only background contribution considered by the collaboration comes from neutral-current (NC) charged pion production, where the pion interacts with argon and can be mistaken for a muon [111]. This contribution is small due to the track length cutting imposed in the event selections and we did not consider it in our simulations.

## 2. Electron neutrino appearance channel:

- *Signal:* electron neutrinos coming from muon neutrino conversion ( $\nu_\mu \rightarrow \nu_e$ ) which interacts through CC producing electrons in the detectors. The event rate for this channel sign is given by

$$n_a^{\nu_\mu \rightarrow \nu_e} = N_e \epsilon_a^{\nu_e} \int_{E_a - \Delta E_a/2}^{E_a + \Delta E_a/2} dE' \int_0^\infty dE \phi_{\nu_\mu}(E) P_{\nu_\mu \rightarrow \nu_e}^{\text{LED}}(E) \times \sigma_{\nu_e \rightarrow \text{Ar}}(E) R^e(E, E'), \quad (2.30)$$

where ( $a = 1, \dots, 11$ ), the fluxes are the same as muon disappearance channel and the neutrino-argon cross section  $\sigma_{\nu_e \rightarrow \text{Ar}}(E)$  was also taken from Ref. [115].  $P_{\nu_\mu \rightarrow \nu_e}^{\text{LED}}(E)$  is given in Eq. 2.26, now with  $\beta = e$  and the energy resolution function  $R^e(E, E')$  is the Gaussian from Eq 2.29 with width of  $\sigma'(E) = 15\%/\sqrt{E[\text{GeV}]}$ , following to Ref. [117]. The energy range for the neutrino event reconstruction are in the Table 2.2. After event reconstruction, the efficiency parameters are as follows

Detector	SBND	MicroBooNE	ICARUS-T600
$N_e$	$5.39 \times 10^{-5}$	$4.39 \times 10^{-4}$	$1.61 \times 10^{-3}$
$\epsilon^{\nu_e}$	0.042	0.0159	0.0163

- *Background:* The main background contribution comes from the survival of intrinsic electron neutrinos ( $\nu_e \rightarrow \nu_e$ ) in the beam, i.e. beam contamination. The event rates for this background component have the same form as Eq. 2.30, with the changes  $\phi_{\nu_\mu}(E) \rightarrow \phi_{\nu_e}(E)$  (from same reference) and  $P_{\nu_\mu \rightarrow \nu_e}^{\text{LED}}(E) \rightarrow P_{\nu_e \rightarrow \nu_e}^{\text{LED}}(E)$ . The post-reconstruction efficiencies are the following

Detector	SBND	MicroBooNE	ICARUS-T600
$\epsilon^{\nu_e}$	0.029	0.0156	0.0122

We also considered muons (muon neutrinos from the CC interaction), which can be mistaken for electrons. NC photon emission, cosmic particles, and dirty events were not considered in our simulation, which correspond to a background reduction of 8.4% for Lar1-ND, 14% for MicroBooNE and 13% for

Electron Neutrino Appearance Channel		Muon Neutrino Disappearance Channel	
Energy Bin Size (GeV)	Energy Range (GeV)	Energy Bin Size (GeV)	Energy Range (GeV)
0.15	0.2-1.10	0.10	0.2-0.4
0.20	1.10-1.50	0.05	0.4-1.0
0.25	1.50-2.00	0.25	1.0-1.5
1.00	2.00-3.00	0.50	1.5-3.0

Table 2.2: Energy range and energy bin size of the electron and muon sample used in this analysis.

ICARUS-T600, respect to the total number of background events expected by the collaboration in the electron neutrino channel [111].

The information on the neutrino fluxes, neutrino cross section, energy resolution of leptons and backgrounds used in the analysis were compiled to be used with the GLOBES c-library, in order to perform the different sensitivity analysis of SBN program at Fermilab. We simulated three years of operation for the neutrino beam in Lar1-ND and ICARUS-T600 detectors and six years in MicroBooNE detector. It is important to emphasize that the detectors do not make a distinction between neutrinos and anti-neutrinos, so neutrino and antineutrino events are added in our simulations.

In the presence of LED, the relations in Eq. 2.24 and Eq. 2.25 give the mass-squared differences and the mixing angles in terms of the standard oscillation parameters. When simulating neutrino event rates to perform the different studies along with this Chapter, we used the best-fit values for the oscillation parameters in the standard three-neutrino framework presented in Nu-Fit 3.2 (2018) [108, 109]. The LED parameters are the lightest neutrino mass  $m_0$  (for normal ordering  $m_0 = m_1^D$  while for inverted ordering  $m_0 = m_3^D$ ) and the radius of extra dimension  $R_{\text{ED}}$ .

We present results based on different sensitivity analysis in the following Sections, using both muon disappearance and electron appearance channels unless otherwise stated. We studied three cases assuming a given event energy spectrum for ‘data’ (or ‘true’ events) and we have performed a hypothesis testing based on a chi-squared  $\chi^2$  function for the different models: **1)** ‘data’ simulated assuming an energy spectrum defined by the three-neutrino case and testing the LED hypothesis, i.e., the usual sensitivity analysis, **2)** ‘data’ simulated assuming an energy spectrum distributed with the LED model and also testing the LED scenario. Here we investigated the SBN potential of measuring the LED parameters  $R_{\text{ED}}$  and  $m_0$ . Finally, **3)** ‘data’ simulated assuming an energy spectrum distributed with the 3+1 model (see Subsec. 1.3.1), where we evaluated the discrimination power of SBN to distinguish LED hypothesis from other models accommodating light sterile neutrino oscillations. We also performed sensitivity calculations for the 3+1 model in appearance and disappearance channels in order to explore relations between LED and 3+1 signatures. The results are shown in the next Section.

## 2.3 Results

As we mentioned before, we will develop three different analysis with the simulated SBN event rates. In order to perform the statistical test between the events we expected from LED model and the events from other hypothesis, we will perform a chi-squared  $\chi^2$  calculation. As SBN has *three* detectors that will record neutrino events, we will employ the following chi-squared function

$$\chi_{\text{SBND}}^2 = \sum_{d=1}^3 \sum_{a=1}^{11} \frac{(O_{a,d}^e - [(1+s)S_{a,d}^e + (1+b)B_{a,d}^e])^2}{O_{a,d}^e} + \frac{s^2}{\rho_s^2} + \frac{b^2}{\rho_b^2} \quad (2.31)$$

$$+ \sum_{a'=1}^{19} \frac{(O_{a',d}^\mu - [(1+s')S_{a',d}^\mu + (1+b')B_{a',d}^\mu])^2}{O_{a',d}^\mu} + \frac{s'^2}{\rho_{s'}^2} + \frac{b'^2}{\rho_{b'}^2} \quad (2.32)$$

where  $O_{a,d}^e$  represents the ‘true’ events in the  $a$ -th energy bin from the detector  $d$  in the electron neutrino appearance channel and  $O_{a',d}^\mu$  are the ‘true’ events in the  $a'$ -th energy bin from the detector  $d$  in the muon neutrino disappearance channel.  $S_{(a,a'),d}^{e,\mu}$  and  $B_{(a,a'),d}^{e,\mu}$  are, respectively, the simulated signal and background events for a chosen set of parameters from a *test* hypothesis. In case of LED hypothesis, the set of parameters would be  $(m_0, R_{\text{ED}})$ . The parameters  $s, s', b, b'$  are called nuisance parameters that would describe signal and background fluctuations due to systematic errors in the flux normalization, detector fiducial mass, etc. The  $\chi_{\text{SBND}}^2$  will be minimized over these nuisance parameters. Finally,  $\rho$  are the systematical errors.

In case of an experiment that already recorded real neutrino events, the entries of  $O$  would be filled with the real data in each bin for both channels. In our case, SBN has not recorded real data yet so we simulated ‘pseudo’ data and considered them as the observed events. For the analysis, the total normalization errors in signal and background ( $\rho_s, \rho'_s, \rho_b$  and  $\rho_{b'}$ ) were set to 10%, and all parameters that were not shown in the plots were fixed to their best-fit values. The first analysis we performed is the *sensitivity analysis*, i.e. the ‘true’ rates assume an energy spectrum defined by the three-neutrino case and the testing rates by the LED hypothesis. The aim of sensitivity analysis is to investigate in which set of parameters  $(m_0, R_{\text{ED}})$  SBN would produce significant signal that departs from the standard three neutrino scenario with considerable confidence level. We tested that our sensitivity results are independent of the  $\delta_{\text{CP}}$  value. For simplicity, we set  $\delta_{\text{CP}} = 234^\circ$  for normal ordering and  $\delta_{\text{CP}} = 278^\circ$  for inverted ordering, according to Ref. [109].

Figure 2.7 shows SBN sensitivity limit with 90% of confidence level (C. L.) in the green curve for normal (left panel) and inverted ordering (right panel), compared with other limits: Sensitivity limits at 95% of C. L. for DUNE experiment (black-dashed curve) presented in Ref. [106], as well as IceCube-40 data and IceCube-79 data (dot-dashed magenta and blue curves, respectively) from Ref. [104], and the combined analysis of T2K and Daya Bay data (dot-dashed gold curve) presented in Ref. [105] are shown. The preferred region (in pink) at 95% C. L. by Gallium and Reactor anomalies from the analysis in Ref. [102] is also included. Finally, sensitivity limits for KATRIN at 90% C. L. (dashed brown curve) due to kinematic limits in beta decay estimated in Ref. [103]

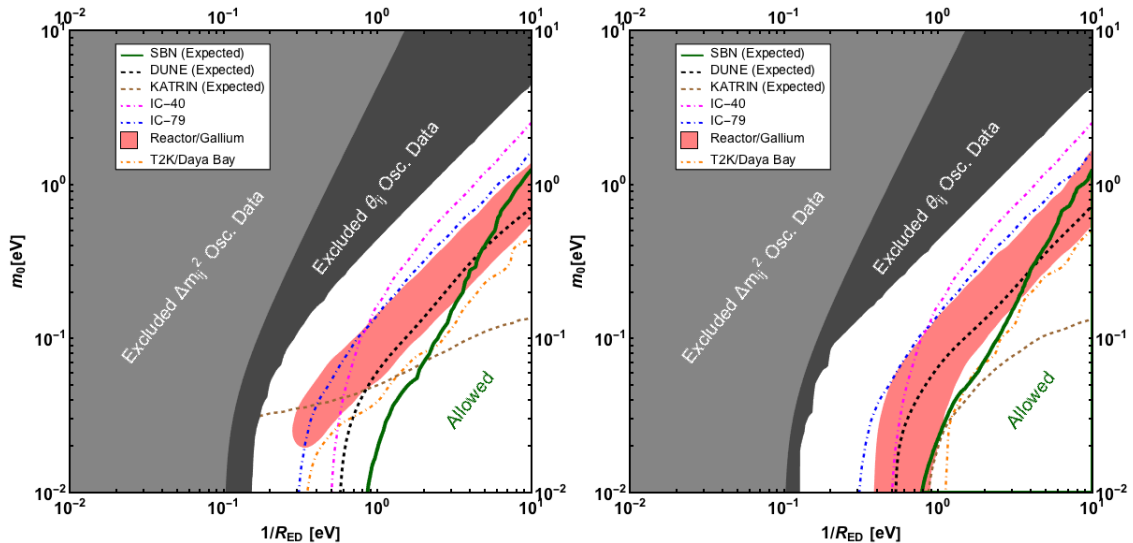


Figure 2.7: Left (Right) panel: Sensitivity limits for the LED parameters,  $R_{\text{ED}}$  and  $m_0$ , considering normal (inverted) ordering of neutrino masses. The regions for LED sensitivity, considering muon disappearance and electron appearance channels, are to the top-left of the curves. Here, we show our 90% C. L. line from SBN limit (green), the 95% C. L. lines from DUNE (black) [106], IceCube-40 (magenta) and IceCube-79 (blue) [104], and 95% C. L. from combined analysis of T2K and Daya Bay (gold) [105]. The 90% C. L. line from KATRIN sensitivity analysis is also shown (brown) [103] and the pink regions are preferred at 95% C. L. by the reactor and Gallium anomaly [102]. The light and dark gray regions are excluded due to neutrino oscillation data.

are shown. The gray shaded regions are the parameters excluded by measurements of the mass-squared differences  $\Delta m_{21}^2$  and  $\Delta m_{31}^2$  (light gray) and of mixing angles  $\theta_{12}$ ,  $\theta_{13}$  and  $\theta_{23}$  (dark gray). It is important to mention that the excluded region due to mixing angle measurements also covers excluded region due to mass-squared differences. An additional constraint to the LED parameters comes from MINOS analysis in Ref. [107] where a similar restriction curve to the one from IceCube was obtained. When  $m_0 \rightarrow 0$ , MINOS constrains  $R_{\text{ED}} < 0.45 \mu\text{m}$  (or  $R_{\text{ED}}^{-1} > 0.44 \text{ eV}$ ) for normal ordering.

We can see that the SBN program is sensitive to the LED parameters and this sensitivity is very competitive, respect to other facilities shown in the plot. This happens specifically for the lower  $m_0$  region and particularly for normal ordering. Compare to constraints from other experiments, the SBN sensitivity to the oscillations predicted by the LED mechanism is better than any other limits in the region when  $m_0 < 2 \times 10^{-1} \text{ eV}$  for normal ordering, and in this region, the maximum sensitivity of our analysis for  $R_{\text{ED}}$  is better than any other oscillation experiment which we trace to the fact that we are testing LED in a short-baseline experiment for the first time, all other sensitivity results corresponds to long-baseline experiments. Concerning the *reactor and gallium anomaly* allowed regions, the SBN program has the potential to ruled out completely this anomaly for any value of  $m_0 < 2 \times 10^{-1} \text{ eV}$ . For higher values of  $m_0$ , the DUNE experiment [106] have the potential to exclude the reactor and gallium anomaly allowed regions, complementing SBN.

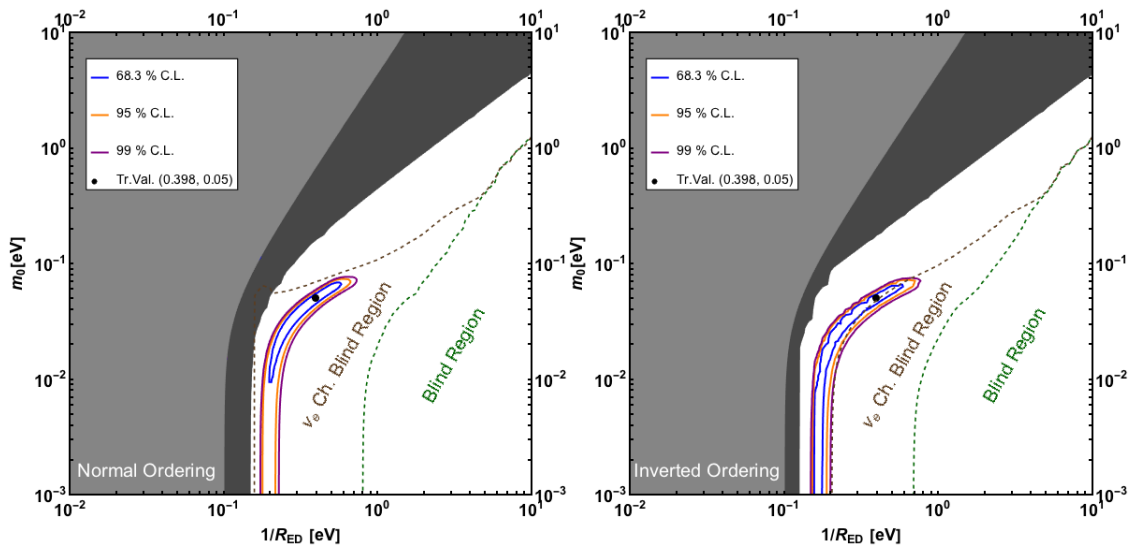


Figure 2.8: Left (right) panel: Allowed regions for the ‘true’ LED parameters  $m_0 = 0.05$  eV and  $1/R_{\text{ED}} = 0.398$  eV and assuming as test model the LED scenario for normal (inverted) ordering. All the other oscillation parameters were fixed to their best fit values. The dashed green (dashed brown) curve shows the SBN sensitivity to both muon disappearance and electron appearance channel (only electron appearance channel). The region denoted by *Blind region* ( $\nu_e$  Ch. *Blind region*) is the region with no sensitivity to the muon neutrino disappearance (electron neutrino appearance).

### 2.3.1 Sensitivity to a non-zero LED oscillation effect on SBN

In order to investigate the potential of SBN to measure the LED parameters, neutrino events were calculated in the same fashion than for the previous sensitivity analysis, but assuming now the LED model with  $m_0 = 0.05$  eV and  $1/R_{\text{ED}} = 0.398$  eV as the ‘true’ values, and testing the LED scenario. All the standard oscillation parameters (which are included in the LED parameters) were fixed to their best-fit values from Refs. [108, 109] as described in Section 2.1. Figure 2.8 shows the allowed regions consistent with the computed events with the true value (black dot) at 68.3% of C. L. (blue curve), 95% of C. L. (orange curve) and 99% of C. L. (purple curve) for both normal ordering (left panel) and inverted ordering (right panel).

We also included in Figure 2.8 the sensitivity result obtained in Figure 2.7 (dashed green line), which we called *Blind Region*, i.e., the region that agrees with the standard three-neutrino scenario, being in this way, ‘blind’ to LED effects. Any point inside the *Blind Region* will have a null result either for the muon disappearance channel or for the electron neutrino appearance channel. The  $\nu_e$  Ch. *Blind Region* presented in Figure 2.8 (dashed brown line) is the result of the sensitivity analysis performed *only* with the computed events from electron neutrino appearance channel. Any point inside the  $\nu_e$  Ch. *Blind Region* will have a null result for the electron neutrino appearance channel. The ‘true’ LED parameters were chosen around the  $\nu_e$  Ch. *Blind Region*, but outside the *Blind Region* for both mass orderings.

It is worth noticing that since the electron neutrino appearance probability is smaller than  $10^{-3}$  for LED, as shown in Figure 2.6, one might not expect a sensitivity exclusion

limit from the appearance channel, i.e., all the obtained sensitivity shown in Figure 2.7 would come from the muon disappearance channel. However, when we computed the sensitivity curve only considering electron appearance channel, we obtained the exclusion limit showed in Figure 2.8 (dashed brown line). In fact, we have a sensitivity curve from electron appearance channel when we consider changes in background profile due to LED effects. The electron neutrino survival probability induced by the LED parameters decreases the intrinsic electron neutrinos from the beam, which is the majority contribution to our background. In other words, we have sensitivity due to the decrease in the number of backgrounds and not by the increase in the signal. A similar effect was found in Ref. [117].

Although not shown in Figure 2.8, we repeated the same analysis with other LED *true values* located inside the exclusion region for both electron and muon neutrino channels (outside the *Blind Region* and the  $\nu_e$  *Ch. Blind Region*). In this case, we have a non-null result in *both* muon disappearance and electron neutrino appearance channels, and therefore the LED parameters that explain this results are unique. As a consequence of this, and due to the logarithmic scale in the plot, we obtained small and concentrated regions around the chosen ‘true’ values, which results in a precision of SBN experiment to the LED parameters below 1%.

### 2.3.2 3+1 scenario at SBN: sensitivity and accuracy of the measurement

In the standard three-neutrino scenario, we expect no oscillations in SBN due to its short-baseline regime. Now, if SBN ‘sees’ an oscillation, it will corresponds to a beyond the standard three-neutrino scenario signal that might be interpreted as an sterile neutrino oscillation. In the 3+1 scenario, the neutrino probabilities for short-baseline distances are given by [118]:

$$P_{\nu_\mu \rightarrow \nu_e}^{3+1} = \sin^2 2\theta_{\mu e} \sin^2 \left( \frac{\Delta m_{41}^2 L}{4E_\nu} \right), \quad (2.33)$$

$$P_{\nu_\mu \rightarrow \nu_\mu}^{3+1} = 1 - \sin^2 2\theta_{\mu\mu} \sin^2 \left( \frac{\Delta m_{41}^2 L}{4E_\nu} \right), \quad (2.34)$$

$$P_{\nu_e \rightarrow \nu_e}^{3+1} = 1 - \sin^2 2\theta_{ee} \sin^2 \left( \frac{\Delta m_{41}^2 L}{4E_\nu} \right), \quad (2.35)$$

where  $\sin^2 2\theta_{\alpha\alpha} \equiv 4(1 - |U_{\alpha 4}|^2)|U_{\alpha 4}|^2$ , with  $\alpha = e, \mu$  and  $\sin^2 2\theta_{\mu e} \equiv 4|U_{e4}|^2|U_{\mu 4}|^2$  are the oscillation amplitudes, defined by the elements of the  $4 \times 4$  generalized PMNS matrix elements  $U_{e4}$  and  $U_{\mu 4}$ , and  $\Delta m_{41}^2$  is the mass-squared difference between the fourth mass state  $m_4$  (which is dominantly made of the sterile component in the neutrino flavor basis) and the first mass state  $m_1$ . The probabilities in Eqs. 2.33, 2.34, 2.35 at short-baselines depend on the three parameters  $U_{e4}, U_{\mu 4}$ . and  $\Delta m_{41}^2$  [119].

We now test the two following cases in the 3+1 scenario:

1. Assuming the ‘true’ event energy distribution as compatible with the three-neutrino

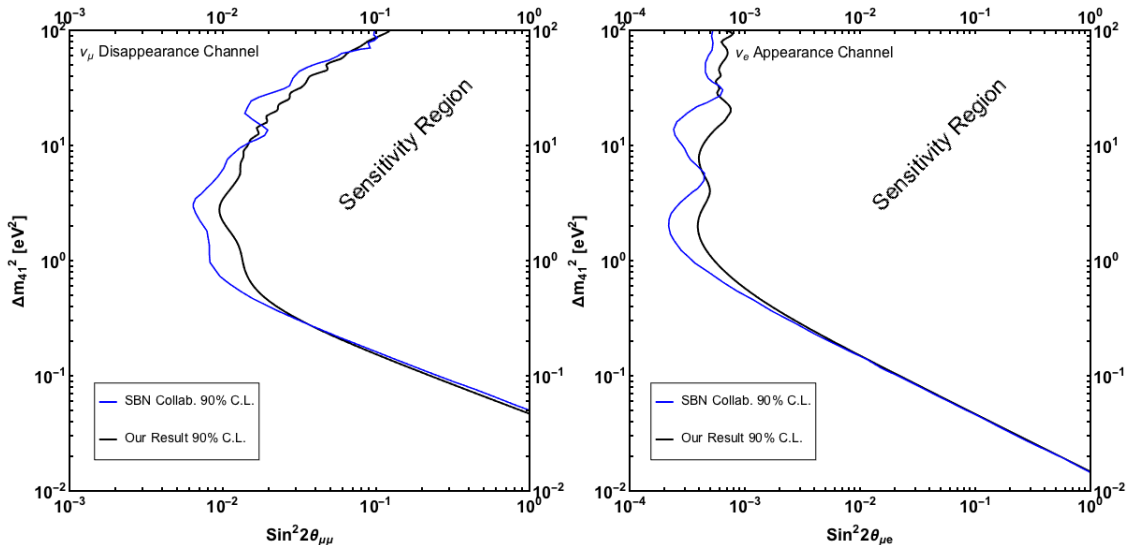


Figure 2.9: Left (Right) panel: Sensitivity limit at 90% of C.L. for the 3+1 model for the muon neutrino disappearance channel (electron neutrino appearance channel), in the parameter space which depends on  $\sin^2 2\theta_{\mu\mu}$  ( $\sin^2 2\theta_{\mu e}$ ) and  $\Delta m_{41}^2$ . Exclusion (sensitivity) regions are to top-right of the black dashed curves in both panels. The solid black curve (solid blue curve) shows our sensitivity (the SBN sensitivity was taken from Ref. [111]).

scenario and testing the 3+1 model. This gives the sensitivity of SBN to the 3+1 scenario that can be seen in Figure 2.9. Exclusion regions are to the right of the black curves for both appearance (right panel) and disappearance (left panel) channels. We have a very good agreement with the SBN sensitivity, comparing the blue and solid curves in Figure 2.9.

- Assuming as the ‘true’ event energy distribution as compatible with the 3+1 scenario and testing the 3+1 model. This will give the accuracy of SBN facility to the parameters of the 3+1 scenario that can be seen in Figure 2.10. For illustration purposes, we show the sensitivity as dashed black curves for the 3+1 model at the SBN from Figure 2.9. The allowed regions assuming the ‘true’ 3+1 parameters  $\sin^2 2\theta_{\mu\mu} = 0.02$ ,  $\sin^2 2\theta_{\mu e} = 0.01$  and  $\Delta m_{41}^2 = 1 \text{ eV}^2$  and also fitting 3+1 hypothesis. Notice that SBN is very sensitive to the mass-squared difference around  $1 \text{ eV}^2$  and the precision that we can get for this value is very good and below 1%. Even though not shown in the figure, large values of  $\sin^2 2\theta_{\mu\mu}$  and  $\sin^2 2\theta_{\mu e}$  gets more precise determined than the lower values shown in the plot. The fast oscillations  $\Delta m_{41}^2 > 10 \text{ eV}^2$  were handled assuming a low-pass filter in our analysis using GLoBES 3.2.17 [112, 113], otherwise we will have spurious results in our sensitivity for 3+1 model.

### 2.3.3 Discrimination power between LED scenario and the 3+1 scenario

One question that remains is that if SBN finds a departure from the three neutrino framework, is it possible to identify which of the two scenarios analyzed in this Chapter

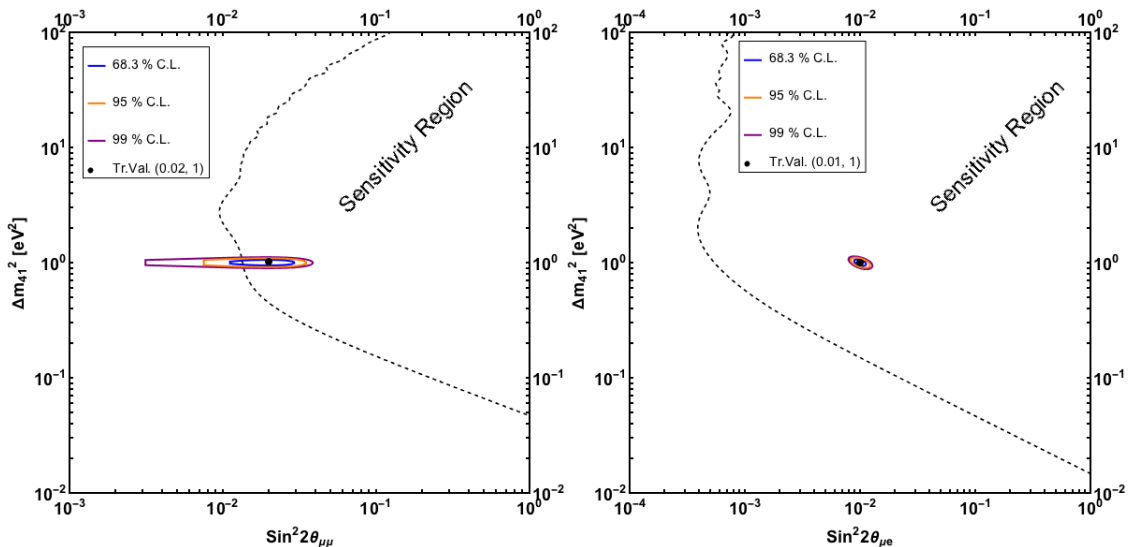


Figure 2.10: Left (Right) panel: Allowed Regions considering the ‘true’ neutrino event spectrum given by the 3 + 1 model with the values  $\sin^2 2\theta_{\mu\mu} = 0.02$  and  $\Delta m_{41}^2 = 1 \text{ eV}^2$  ( $\sin^2 2\theta_{\mu e} = 0.01$  and  $\Delta m_{41}^2 = 1 \text{ eV}^2$ ) in the muon neutrino disappearance channel (the electron neutrino appearance channel). The dashed curve in both plots is the sensitivity curve for the respective channels.

would be responsible for the new signal (assuming is not something else)? In the following, we analyze the discrimination power of the SBN experiment comparing both the LED and the 3+1 scenarios. Regarding the 3+1 fit to the LED scenario, we calculated events with the ‘true’ LED parameters  $m_0 = 0.05 \text{ eV}$  and  $1/R_{\text{ED}} = 0.398 \text{ eV}$  assuming normal ordering. With this ‘true’ events, both appearance and disappearance channels were fitted separately, fixing the parameters not shown in the plots. Figure 2.11 shows the result of the fit in the *disappearance channel*, i.e. the  $\chi$ -squared function will be only Eq. 2.32 (left panel) with allowed curves of 68.3% of C. L. (blue), 95% of C. L. (orange) and 99% of C. L. (purple). The number of degrees of freedom (d.o.f.) was equal to 17 (19 energy bins minus 2 free parameters). The best-fit of the test values is represented in the black dot and has values of  $\sin^2 2\theta_{\mu\mu} = 0.1$  and  $\Delta m_{41}^2 = 0.5 \text{ eV}^2$ . We have not found a good fit, where  $\Delta\chi^2 = \chi_{3+1}^2 - \chi_{\text{LED}}^2 = 8$  for the best-fit point, giving more than  $2\sigma$  of deviation between the two models.

We have also checked that when using the new set of parameters  $m_0 = 0.316 \text{ eV}$  and  $1/R_{\text{ED}} = 1 \text{ eV}$  for the muon disappearance case, we have obtained a  $\Delta\chi^2 \approx 104$  for the best-fit (of the test values) point, implying a bad fit. This result can be explained due to the fact that for some values of the LED parameters, as in this case, more KK states start to contribute in the oscillation probability and the 3+1 model cannot emulate the LED model.

Following a similar procedure, this time fitting the LED model for some ‘true’ values for the 3+1 parameters, we could not obtain good fits. The analysis is shown in the right panel of Figure 2.11. In fact, if we consider the amplitude  $\sin^2 2\theta_{\mu\mu} = 0.01$  and the same  $\Delta m_{41}^2 = 0.5 \text{ eV}^2$ , the allowed regions would be almost entirely inside the *Blind Region* (bottom-right part from the dashed green curve in the right panel of Figure 2.11). From

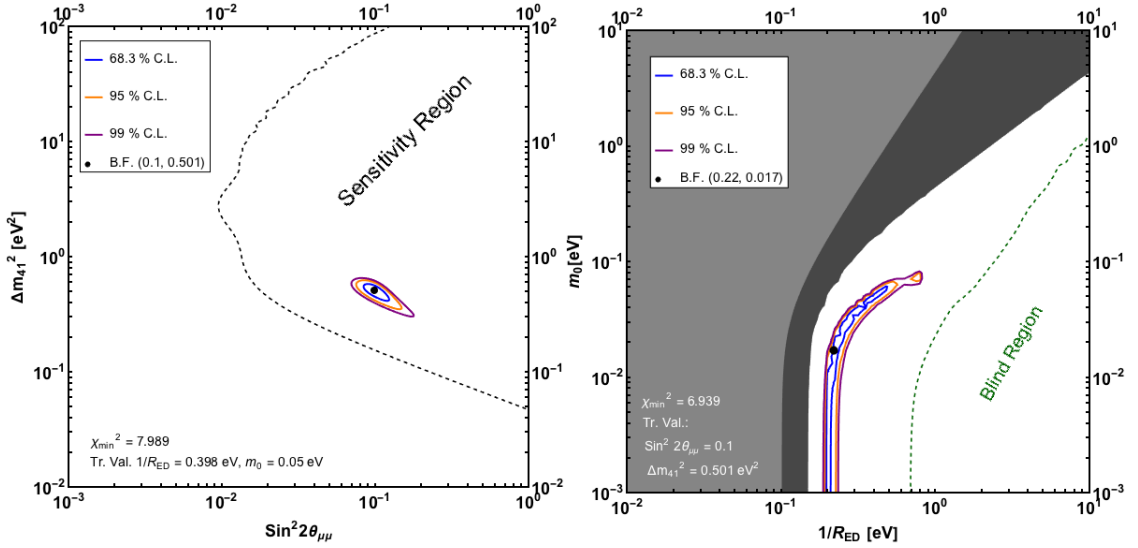


Figure 2.11: Left panel, sensitivity results fitting the 3+1 model parameters assuming the ‘true’ LED parameters  $m_0 = 0.05$  eV and  $1/R_{\text{ED}} = 0.398$  eV, for normal ordering. Right panel, sensitivity results fitting the LED parameters for the ‘true’ 3+1 parameters  $\sin^2 2\theta_{\mu\mu} = 0.1$  and  $\Delta m_{41}^2 = 0.5$  eV<sup>2</sup>, also for normal ordering. The allowed sensitivity regions correspond to the 68.3% of C. L. (blue), 95% of C. L. (orange) and 99% of C. L. (purple), the best-fit points appear as black dots.

this analysis, we obtained the value  $\Delta\chi^2 \approx 187$ . We also considered the case of larger mixing with true values  $\sin^2 2\theta_{\mu\mu} = 0.1$  and  $\Delta m_{41}^2 = 3$  eV<sup>2</sup> and we obtained the value  $\Delta\chi^2 \approx 149$  for the best-fit point.

In the case of the *electron neutrino appearance channel*, we repeated the same procedure done for the muon channel: we calculated events for a given ‘true’ values for the LED parameters and we fitted the electron neutrino appearance parameters in the 3+1 model using Eq. 2.31. The summary of the results are the following:

- For  $m_0 = 0.05$  eV and  $1/R_{\text{ED}} = 0.398$  eV, the best-fit and the allowed regions were located outside the Sensitivity Region with the value  $\Delta\chi^2 \approx 78.3$  for the best-fit point, implying a very poor fit.
- For  $m_0 = 0.316$  eV and  $1/R_{\text{ED}} = 1$  eV, the best-fit and allowed regions were located outside the sensitivity region, with  $\Delta\chi^2 \approx 538$  for the best-fit point, implying a very poor fit.

The previous results (for the electron appearance case) were somehow expected since we could only obtain LED sensitivity from electron neutrino channel in Figure 2.8 with effects of the LED parameters in the background. Then, we should not expect that the signal of the electron neutrino conversion can be fitted with the 3+1 parameters. In other words, evidence of electron appearance in short-baseline experiments as the recent MiniBooNE analysis in Ref. [120] are inconsistent with the LED hypothesis. Similar conclusion was made in Ref. [121].

The right panel of Figure 2.11 also shows the LED fit for a given set of ‘true’ parameters of the 3 + 1 model considering only muon disappearance. We fixed the 3+1 parameters

	$\nu_\mu$ Disappearance	$\nu_e$ Appearance
True hypothesis	LED ( $m_0, 1/R_{\text{ED}}$ )	LED ( $m_0, 1/R_{\text{ED}}$ )
Test model	LED ( $m_0, 1/R_{\text{ED}}$ )	LED ( $m_0, 1/R_{\text{ED}}$ )
3+1 ( $\sin^2 2\theta_{\mu\mu}$ or $\sin^2 2\theta_{\mu e}, \Delta m_{41}^2$ )	True: (0.05 eV, 0.398 eV) best-fit point: (0.1, 0.5 eV <sup>2</sup> ) $\Delta\chi^2 \approx 8$	True: (0.05 eV, 0.398 eV) - $\Delta\chi^2 \approx 78$
3+1 ( $\sin^2 2\theta_{\mu\mu}$ or $\sin^2 2\theta_{\mu e}, \Delta m_{41}^2$ )	True: (0.316 eV, 1 eV) - $\Delta\chi^2 \approx 104$	True: (0.316 eV, 1 eV) - $\Delta\chi^2 \approx 538$
True hypothesis	3+1 ( $\sin^2 2\theta_{\mu\mu}, \Delta m_{41}^2$ )	3+1 ( $\sin^2 2\theta_{\mu e}, \Delta m_{41}^2$ )
Test model	3+1 ( $\sin^2 2\theta_{\mu\mu}, \Delta m_{41}^2$ )	3+1 ( $\sin^2 2\theta_{\mu e}, \Delta m_{41}^2$ )
LED ( $m_0, 1/R_{\text{ED}}$ )	True: (0.1, 0.5 eV <sup>2</sup> ) best-fit point: (0.017 eV, 0.22 eV) $\Delta\chi^2 \approx 6.8$	*
LED ( $m_0, 1/R_{\text{ED}}$ )	True: (0.01, 0.5 eV <sup>2</sup> ) - $\Delta\chi^2 \approx 187$	*
LED ( $m_0, 1/R_{\text{ED}}$ )	True: (0.1, 3 eV <sup>2</sup> ) - $\Delta\chi^2 \approx 149$	*

( - ) The best-fit point is outside Exclusion Region, ( \* ) It is not expected a positive signal of  $\nu_e$  appearance in SBN within LED model.

Table 2.3: Discrimination power of SBN facility for 3+1 model and LED model.

$\sin^2 2\theta_{\mu\mu} = 0.1$  and  $\Delta m_{41}^2 = 0.5 \text{ eV}^2$  and fitted the LED parameters for normal ordering. The allowed curves corresponds to the 68.3% of C. L. (blue), 95% of C. L. (orange) and 99% of C. L. (purple). The best-fit point obtained was  $m_0 = 0.017 \text{ eV}$  and  $1/R_{\text{ED}} = 0.22 \text{ eV}$ . Following the same procedure, we found  $\Delta\chi^2 \approx 6.8$  for the best-fit point.

As we discussed in Section 2.3.1, with information of the electron neutrino appearance channel (and not the muon disappearance) one can discriminate the LED scenario from the standard three-neutrino case only if changes in the background (i.e. the electron neutrino disappearance from the intrinsic  $\nu_e$  of the beam) are considered. In this way, LED is not contributing to the *signal* ( $\nu_e$  conversion) in the electron neutrino channel. Therefore, when regarding the LED fit under 3+1 scenario on these conditions, we would not expect to accommodate LED parameters for any set of ‘true’ parameters of the 3 + 1 model considering only the signal of electron neutrino appearance channel.

Finally, all the results obtained for the discrimination power of LED and the 3+1 model are summarized in Table 2.3.

## 2.4 Conclusions

In the dawn of the new era of high precision neutrino experiments, the search for Beyond Standard Model (BSM) physics will bring an understanding of the mechanism beyond neutrino masses and neutrino mixing. The possibility to have in nature the presence of large extra dimension is intriguing and it has several consequences for the phenomenology of neutrino physics, such as the existence of infinite tower of Kaluza-Klein mass states of neutrinos. The Short-Baseline Neutrino Program SBN at Fermilab will fully test the presence of large extra dimension in neutrino oscillations.

We have developed GLoBES simulation files [122] that include the three detectors at SBN facility where information of the two main channels of SBN program, the  $\nu_\mu$  muon neutrino disappearance channel and the  $\nu_e$  electron neutrino appearance channel, are included. In the paradigm of three neutrino oscillation, we expect to see no oscillation in any of SBN detectors. With the assumption that we measure no oscillations in any of SBN detectors, we can put bounds on the LED scenario. In the LED scenario, the non-standard oscillations are accounted for with two parameters, the lightest Dirac neutrino mass  $m_0$  and the radius of large extra dimension  $R_{\text{ED}}$ . We have shown in Figure 2.6 the regions with sizable muon neutrino disappearance probability and electron neutrino appearance probability in the presence of LED, for either normal or inverted hierarchy of active states. The typical values that we can test are  $P(\nu_\mu \rightarrow \nu_\mu) \sim 0.90$  and  $P(\nu_\mu \rightarrow \nu_e) \sim 10^{-4} - 10^{-3}$  for a  $L/E_\nu = 1.2$  km/GeV.

We showed in Figure 2.7 the sensitivity plot for the LED scenario that is the main result of this work, based on the simulation details described in Section 2.2. The solid green curve is the sensitivity of LED scenario, the other dashed curves are the constraints/sensitivities from other experiments to the LED scenario and the pink region is the allowed region to explain the reactor neutrino anomaly. We notice that SBN sensitivity curve has, for normal ordering, *the strongest bound* for almost all parameter region, with exception of the values of  $m_0 > 2 \times 10^{-1}$  eV and  $1/R_{\text{ED}} > 3$  eV. From Figure 2.7, we have learned that all sensitivity to LED scenario came from the muon disappearance channel and that electron neutrino appearance channel plays a marginal role.

Any positive signal of a neutrino oscillation in the SBN facility will be a departure of the present three neutrino paradigm. The main goal of the SBN facility is to test the hint of neutrino oscillation from LSND, MiniBoone and reactor anomaly. This hint is more usually discussed in the context of the 3+1 scenario with one additional sterile neutrino. Then, we first reproduced the sensitivity region for both channels considered in this Thesis, under the 3+1 framework with the assumptions described in detail in Section 2.2. Then, we computed the sensitivity region and compared it with the official sensitivity region of the SBN proposal, reaching a good agreement as shown in Figure 2.9. In Figure 2.10, we showed the precision that we can have for a given choice of the parameters in a true 3+1 oscillation scenario. We found that the two channels provide sufficient information to get a few percent of accuracy in the oscillation parameters.

Finally, regarding the discrimination power of the SBN facility, the remaining question: Can the SBN be able to discriminate different physics scenarios when it has a clear departure from the three-neutrino paradigm in the data?, was answered. Table 2.3 summarizes our results. It is possible to discriminate between both models at  $3\sigma - 10\sigma$ . The worst scenario was shown in Figure 2.11, where we get a  $2\sigma - 3\sigma$  discrimination using the muon disappearance channel only. For other choices of parameters, as detailed in Table 2.3, we can easily discriminate the source of new physics in the SBN experiment, either the large extra dimension or the 3+1 scenario.

## Chapter 3

# A Heavy Neutrino Decay

Over the last several decades, a variety of revolutionary neutrino puzzles evolved into our current understanding of the neutrino sector of fundamental particle physics. A few of these puzzles, however, remain unresolved. Among them are data from the Liquid Scintillator Neutrino Detector (LSND) and MiniBooNE experiments. LSND observes a very significant excess of  $\bar{\nu}_e$ -candidate events [20], while the MiniBooNE collaboration reported a combined 4.7 sigma excess of  $\nu_e$ - [59, 61] and  $\bar{\nu}_e$ -candidate events [60]. If both the LSND and MiniBooNE data are a consequence of the same unexplained phenomenon, the combined evidence is at the 6 sigma level [61].

Under the assumption that there are no unaccounted for “mundane” explanations to these two excesses – unidentified background processes, problems with modelling the neutrino scattering process, detector-related effects, etc – these so-called short-baseline anomalies (see Subsec. 1.3)<sup>1</sup> translate into new more physics – on top of nonzero active neutrino masses – in the neutrino sector. The simplest new physics interpretation to the data from LSND and MiniBooNE is to postulate that a  $\nu_\mu$  ( $\bar{\nu}_\mu$ ) produced at the experiment beam complexes has nonzero probability of being detected as a  $\nu_e$  ( $\bar{\nu}_e$ ). Neutrino oscillations can lead to this phenomenon by introducing the 3+1 Model (see Subsec. 1.3.1), in which a fourth eV-scale neutrino mass eigenstate  $\nu_4$  associated to a mass-squared difference  $\Delta m^2 \sim 1 \text{ eV}^2$ . The data point to new mixing parameters such that  $|U_{e4}|^2|U_{\mu4}|^2 \sim 10^{-3}$  [61]. In this scenario, the new flavor eigenstate is postulated to have no gauge quantum numbers and is hence dubbed a sterile neutrino  $\nu_s$ .

While the 3+1 hypothesis fits all data associated with searches for  $\nu_\mu \rightarrow \nu_e$  appearance, it is in conflict with other data, including neutrino disappearance data at short-baselines once there is no incontrovertible evidence for neutrino disappearance at short-baselines. These failed searches constrain  $|U_{e4}|^2$  and  $|U_{\mu4}|^2$  to be less than several percent and hence fail to satisfy  $|U_{e4}|^2|U_{\mu4}|^2 \sim 10^{-3}$  from appearance searches. More quantitatively, global fits to the world’s neutrino data indicate that the 3+1 hypothesis is not a satisfactory explanation for the short-baseline anomalies. See, for example, Refs. [123, 90, 124, 125] for recent analyses and discussions.

In this Chapter, we revisit a different solution to the LSND and MiniBooNE puzzle,

---

<sup>1</sup>The short-baseline anomalies also include the reactor and gallium anomalies. For recent summaries of these data, see, for example, Refs. [123, 90, 124, 125]. We will not account for either of them in this work.

presented in Ref [126]. Instead of assuming that a fourth eV-scale neutrino is produced coherently in the neutrino source, we postulate that a heavier fourth neutrino mass eigenstate is produced and that this new neutrino state decays into an electron-type neutrino and a new, effectively massless scalar particle [127]. The decay is prompt enough such that, a significant portion of the time the daughter neutrino can interact in the detector and lead to an excess of  $\nu_e$ - and  $\bar{\nu}_e$ -candidate events. We perform the analysis of the LSND and MiniBooNE experiments, and ask whether the heavy-neutrino decay hypothesis is a good fit to the data. We explore two different decay scenarios with Majorana neutrinos and Dirac neutrinos. We comment the heavy-neutrino decay hypothesis constraints from disappearance searches and precision measurements of leptonic meson decays, that constraints the new interaction. Finally, we also perform the Short-Baseline Neutrino Program (SBN) sensitivity under this heavy-neutrino decay hypothesis.

### 3.1 Formalism

We postulate the existence of a fourth neutrino mass eigenstate. Since we want to explain the data from LSND and MiniBooNE, the fourth neutrino must have a nonzero  $\nu_\mu$  component. We don't need a nonzero  $\nu_\tau$  or  $\nu_e$  component so we set these to zero. A very small  $\nu_e$  or  $\nu_\tau$  component would not modify our results in a significant way. In other words,  $U_{e4} = U_{\tau4} = 0$  and  $\nu_\mu = U_{\mu l} \nu_l$ ,  $l = 1, 2, 3, 4$ ,  $U_{\mu4} \neq 0$ .

We further introduce a new interaction that allows  $\nu_4$ , with mass  $m_4$ , to decay into a new, very light scalar field  $\phi$  and a light neutrino  $\nu_i$ , with mass  $m_i$  ( $i = 1, 2, 3$ ). We will assume that the new scalar field  $\phi$  is a standard model gauge singlet and that it carries zero lepton number. We will also assume that the new interaction violates parity maximally and, like the weak-interactions, only couples to left-chiral light neutrinos. At low-energies, the interaction that mediates the heavy neutrino decay is

$$\mathcal{L} = - \sum_{i=1}^3 g_{4i} \overline{\nu_{4L}^c} \nu_{iL} \phi + \text{H.c.} . \quad (3.1)$$

where  $g_{4i}$  ( $i = 1, 2, 3$ ) are the coupling constants between  $\nu_4$  and the each one of the active neutrinos  $\nu_i$ ,  $\nu_{4L}^c = \mathcal{C} (\gamma^0)^T \nu_{4L}^*$  and  $\mathcal{C}$  is the charge-conjugation matrix. In the Dirac representation of gamma matrices,  $\mathcal{C} = i\gamma_2\gamma^0$ . If neutrinos are Dirac particles, the interaction in Eq. 3.1 enables the process  $\nu_{4L} \rightarrow \nu_{iL} + \phi$ , while for Majorana particles, it is possible to have both  $\nu_{4L} \rightarrow \nu_{iL} + \phi$  and  $\nu_{4L} \rightarrow \bar{\nu}_{iR} + \phi$ . Since we are interested in the limit where the light neutrino masses are negligible, it is meaningful and convenient to talk about  $\nu_i$  – always left-handed – and  $\bar{\nu}_i$  – always right-handed.

The decay amplitude  $\mathcal{M}$  for the considered interaction can be given by

$$\mathcal{M} = g_{4i} \overline{\nu_4^c}(p_4, s_4) \nu_i(p_i, s_i) , \quad (3.2)$$

where  $p_4, s_4$  and  $p_i, s_i$  are the four momenta and the spin of  $\nu_4$  and  $\nu_i$ , respectively. The squared module of the amplitude in Eq. 3.2 is

$$|\mathcal{M}|^2 = |g_{4i}|^2 \overline{\nu_i}(p_i, s_i) \nu_4^c(p_4, s_4) \overline{\nu_4^c}(p_4, s_4) \nu_i(p_i, s_i). \quad (3.3)$$

Taking into account that  $\nu_4^c(p_4, s_4) \overline{\nu_4^c}(p_4, s_4) = \nu_4(p_4, s_4) \overline{\nu_4}(p_4, s_4)$  [128], we proceed with  $|\mathcal{M}|^2$  calculation in the following:

$$\begin{aligned} |\mathcal{M}|^2 &= |g_{4i}|^2 \text{Tr} \left[ (\not{p}_4 + m_4) \frac{(1 + \gamma^5 \not{s}_4)}{2} (\not{p}_i + m_i) \frac{(1 + \gamma^5 \not{s}_i)}{2} \right] \\ &= |g_{4i}|^2 [(p_4 \cdot p_i + m_4 m_i)(1 - s_4 \cdot s_i) + (p_4 \cdot s_i)(p_i \cdot s_4)] . \end{aligned} \quad (3.4)$$

Considering that all the neutrinos taking part in this decay are relativistic, we can define the neutrino chiral states in terms of the helicity states. In this way, if a neutrino is produced in the final state,  $s_4^\mu = s_i^\mu$  and if a antineutrino is produced in the final state (only for the Majorana case),  $s_4^\mu = -s_i^\mu$  ( $\mu = 0, 1, 2, 3$ ), where

$$s_j^\mu = \frac{1}{m_j \beta_j} p_j^\mu - \frac{\sqrt{1 - \beta_j^2}}{\beta_j} \eta^{\mu 0} \quad (j = i, 4) \quad (3.5)$$

where  $\beta_j = p_j/E_j$  and  $\sqrt{1 - \beta_j^2} = m_j/E_j$ ,  $E_j$  being the particle energy and  $\eta^{\mu 0}$  being the first column elements of the metric tensor  $\eta$ . The squared amplitude in Eq. 3.4 when  $\nu_4 \rightarrow \nu_i + \phi$  ( $|\mathcal{M}(\nu_4 \rightarrow \nu_i + \phi)|^2$ ) and when  $\nu_4 \rightarrow \bar{\nu}_i + \phi$  ( $|\mathcal{M}(\nu_4 \rightarrow \bar{\nu}_i + \phi)|^2$ ) are given, respectively, by

$$\begin{aligned} |\mathcal{M}(\nu_4 \rightarrow \nu_i + \phi)|^2 &= |g_{4i}|^2 \frac{1}{\beta_4 \beta_i} \left[ (p_4 \cdot p_i) \left( \beta_i \beta_4 - 1 - \frac{m_i m_4}{E_i E_4} \right) + m_i m_4 \beta_i \beta_4 \right. \\ &\quad \left. - \frac{m_i^2 m_4^2}{E_i E_4} + m_i m_4 + m_4^2 \frac{E_i}{E_4} + m_i^2 \frac{E_4}{E_i} \right] \end{aligned} \quad (3.6)$$

and

$$\begin{aligned} |\mathcal{M}(\nu_4 \rightarrow \bar{\nu}_i + \phi)|^2 &= |g_{4i}|^2 \frac{1}{\beta_4 \beta_i} \left[ (p_4 \cdot p_i) \left( \beta_i \beta_4 + 1 + \frac{m_i m_4}{E_i E_4} \right) + m_i m_4 \beta_i \beta_4 \right. \\ &\quad \left. + \frac{m_i^2 m_4^2}{E_i E_4} - m_i m_4 - m_4^2 \frac{E_i}{E_4} - m_i^2 \frac{E_4}{E_i} \right] \end{aligned} \quad (3.7)$$

In the relativistic approximation,  $\beta_4 \approx \beta_i \rightarrow 1$  and  $m_4 \ll E_4$ . Also, doing  $p_4 \cdot p_i = m_4^2/2$  ( $m_i, m_\phi = 0$ ), we finally obtain

$$|\mathcal{M}(\nu_4 \rightarrow \nu_i + \phi)|^2 = |g_{4i}|^2 m_4^2 \frac{E_i}{E_4} \quad (3.8)$$

and

$$|\mathcal{M}(\nu_4 \rightarrow \bar{\nu}_i + \phi)|^2 = |g_{4i}|^2 m_4^2 \left(1 - \frac{E_i}{E_4}\right) \quad (3.9)$$

The transition rates for the considered decay channels is determined by the amplitudes obtained in Eq. 3.8 and Eq. 3.9 and the phase space according to Fermi's "Golden Rule" [129]. Therefore, the differential decay rates of the  $(\nu_4 \rightarrow \nu_i + \phi)$  and  $(\nu_4 \rightarrow \bar{\nu}_i + \phi)$  processes are, respectively

$$\frac{d\Gamma_{(\nu_4 \rightarrow \nu_i + \phi)}(E_4)}{dE_i} = \frac{1}{16\pi E_4^2} |\mathcal{M}(\nu_4 \rightarrow \nu_i + \phi)|^2 \quad (3.10)$$

and

$$\frac{d\Gamma_{(\nu_4 \rightarrow \bar{\nu}_i + \phi)}(E_4)}{dE_i} = \frac{1}{16\pi E_4^2} |\mathcal{M}(\nu_4 \rightarrow \bar{\nu}_i + \phi)|^2 \quad (3.11)$$

For relativistic neutrinos and  $m_i = 0$ , the integration limits of the final neutrino energy are  $0 < E_i < E_4$ , and hence, the total decay width for  $(\nu_4 \rightarrow \nu_i + \phi)$  and  $(\nu_4 \rightarrow \bar{\nu}_i + \phi)$  in the laboratory reference frame are

$$\Gamma_{(\nu_4 \rightarrow \nu_i + \phi)}(E_4) = \Gamma_{(\nu_4 \rightarrow \bar{\nu}_i + \phi)}(E_4) = \frac{|g_{4i}|^2 m_4^2}{32\pi E_4}. \quad (3.12)$$

The same expressions, of course, holds for the decay of  $\bar{\nu}_4$ . In this way, the total decay width is, respectively, for Dirac and Majorana neutrinos

$$\Gamma_4^{\text{Dirac}} = \sum_{i=1}^3 \Gamma_{(\nu_4 \rightarrow \nu_i + \phi)} \quad (3.13)$$

$$\Gamma_4^{\text{Majorana}} = \sum_{i=1}^3 \Gamma_{(\nu_4 \rightarrow \nu_i + \phi)} + \Gamma_{(\nu_4 \rightarrow \bar{\nu}_i + \phi)}. \quad (3.14)$$

Notice that  $\Gamma_4^{\text{Majorana}} = 2 \Gamma_4^{\text{Dirac}}$ . The relation between massive and flavor neutrinos can be parameterized in terms of the 3+1 mixing. Thus, a given neutrino mass state  $\nu_l$  ( $l = 1, 2, 3, 4$ ) can be written as a linear combination of the flavor states  $\nu_\alpha$  as follows

$$\nu_l = \sum_{\alpha=e,\mu,\tau,s} U_{l\alpha} \nu_\alpha. \quad (3.15)$$

If we plug the mass eigenstates from Eq. 3.15 into the Lagrangian in Eq. 3.1, we can redefine the coupling constants  $g_{4l}$  in the flavor basis  $g_{\alpha\beta}$  ( $\alpha, \beta = e, \mu, \tau, s$ ) according to the relation

$$g_{\alpha\beta} = U_{\alpha 4} \sum_{l=1}^4 g_{4l} U_{l\beta} = U_{\alpha 4} g_\beta, \quad (3.16)$$

in which we defined

$$g_\beta = \sum_{l=1}^4 g_{4l} U_{l\beta}. \quad (3.17)$$

As we mentioned in the beginning, we set  $U_{e4} = U_{\tau 4} = 0$ , in such a way that

$$g_e = \sum_{i=1}^3 g_{4i} U_{ie} \quad \text{and} \quad g_\tau = \sum_{i=1}^3 g_{4i} U_{i\tau} \quad (3.18)$$

The squared module of  $g_{\alpha\beta}$  in Eq. 3.16 is given by

$$|g_{\alpha\beta}|^2 = |U_{\alpha 4}|^2 |g_\beta|^2 = |U_{\alpha 4}|^2 \sum_{l=1}^4 \sum_{k=1}^4 g_{4l} U_{l\beta} g_{4k}^* U_{k\beta}^*. \quad (3.19)$$

Summing  $|g_{\alpha\beta}|^2$  in Eq. 3.19 in  $\beta$  for all flavors, we have

$$\sum_{\beta=e,\mu,\tau,s} |g_{\alpha\beta}|^2 = |U_{\alpha 4}|^2 \sum_{\beta=e,\mu,\tau,s} |g_\beta|^2 = |U_{\alpha 4}|^2 \sum_{l=1}^4 \sum_{k=1}^4 g_{4l} g_{4k}^* \sum_{\beta=e,\mu,\tau,s} U_{l\beta} U_{\beta k}^* \quad (3.20)$$

$$= |U_{\alpha 4}|^2 \sum_{l=1}^4 \sum_{k=1}^4 g_{4l} g_{4k}^* \delta_{lk} \quad (3.21)$$

$$= |U_{\alpha 4}|^2 \sum_{l=1}^4 |g_{4l}|^2. \quad (3.22)$$

where in Eq. 3.20 we used the unitary relation of the U matrix. Comparing Eq. 3.20 with Eq. 3.22, we finally obtain

$$\sum_{\beta=e,\mu,\tau,s} |g_\beta|^2 = \sum_{l=1}^4 |g_{4l}|^2 \equiv |g|^2. \quad (3.23)$$

As we are working with decay, the energy distributions of the daughter particles are not the same than mother particles, in the way we need to work with the differential probability of transition per daughter particle energy interval. From this point, we will discriminate the calculations for Dirac and Majorana neutrinos. Therefore, we will have two cases:

- **Dirac neutrinos:** The differential probability that a (anti)neutrino of flavour  $\nu_\alpha$  with energy  $E_{\nu_\alpha}$  is converted into an (anti)neutrino of flavor  $\nu_\beta$  with energy in the interval  $[E_{\nu_\beta}, E_{\nu_\beta} + dE_{\nu_\beta}]$  after travelling a distance  $L$  is:

$$\begin{aligned}
\frac{dP_{\nu_\alpha \rightarrow \nu_\beta}^{\text{Dirac}(-)(-)}(E_{\nu_\alpha})}{dE_{\nu_\beta}} &= \left| \sum_{i=1}^3 U_{\alpha i} U_{\beta i}^* \exp\left(-i \frac{m_i^2 L}{2E_{\nu_\alpha}}\right) + \right. \\
&\quad \left. + U_{\alpha 4} U_{\beta 4}^* \exp\left(-i \frac{m_4^2 L}{2E_{\nu_\alpha}}\right) \exp\left(-\frac{\Gamma_4^{\text{Dirac}} L}{2}\right) \right|^2 \delta(E_{\nu_\alpha} - E_{\nu_\beta}) + \\
&\quad + G^{\text{Dirac}}(E_{\nu_\alpha}, E_{\nu_\beta}) \left(1 - e^{-\Gamma_4^{\text{Dirac}} L}\right)
\end{aligned} \tag{3.24}$$

The first two terms in Eq. 3.24 describe the oscillations among neutrino mass states. Notice that the oscillation term of the heavy neutrino is weighted by the probability that they do not decay. The third term describes the appearance of decay products, where  $G^{\text{Dirac}}(E_{\nu_\alpha}, E_{\nu_\beta})$  is the normalized energy distribution of the daughter particles  $\nu_\beta$ , given explicitly by

$$G^{\text{Dirac}}(E_{\nu_\alpha}, E_{\nu_\beta}) = 2 |U_{\alpha 4}|^2 \frac{|g_\beta|^2}{\sum_{\beta=e,\mu,\tau,s} |g_\beta|^2} \frac{E_{\nu_\beta}}{E_{\nu_\alpha}^2} = 2 |U_{\alpha 4}|^2 R_\beta \frac{E_{\nu_\beta}}{E_{\nu_\alpha}^2}, \tag{3.25}$$

where  $R_\beta \equiv \frac{|g_\beta|^2}{\sum_{\beta=e,\mu,\tau,s} |g_\beta|^2}$  is the branching ratio of the decay resulting in a neutrino with flavor beta. The expression in Eq. 3.25 is valid only in the case the daughter particles are stable and do not oscillate along the distance  $L$ . To ensure this condition, we will impose the short-baseline (SB) regime where  $L/E_{\nu_\alpha} \sim 1$  MeV/m (GeV/km) such that ordinary neutrino oscillations, driven by  $m_2^2 - m_1^2$  and  $m_3^2 - m_1^2$ , do not have time to modify neutrino flavor evolution (see Subsec. 1.2.1). With this assumption and also evidencing that  $m_4 \gg m_1, m_2, m_3$ , the oscillation probability in Eq. 3.24 becomes

$$\begin{aligned}
\left[ \frac{dP_{\nu_\alpha \rightarrow \nu_\beta}^{\text{Dirac}(-)(-)}(E_{\nu_\alpha})}{dE_{\nu_\beta}} \right]_{\text{SB}} &= \left( |U_{\alpha 4}|^2 |U_{\beta 4}|^2 \quad (\alpha \neq \beta) \quad \text{or} \quad (1 - |U_{\alpha 4}|^2)^2 \quad (\alpha = \beta) + \right. \\
&\quad \left. + |U_{\alpha 4}|^2 |U_{\beta 4}|^2 e^{-\Gamma_4^{\text{Dirac}} L} \right) \delta(E_{\nu_\alpha} - E_{\nu_\beta}) + \\
&\quad + G^{\text{Dirac}}(E_{\nu_\alpha}, E_{\nu_\beta}) \left(1 - e^{-\Gamma_4^{\text{Dirac}} L}\right), \tag{3.26}
\end{aligned}$$

which we will explicitly write

$$\Gamma_4^{\text{Dirac}}(E_{\nu_\alpha}) = \sum_{\beta=e,\mu,\tau,s} |g_\beta|^2 \frac{m_4^2}{32\pi E_{\nu_\alpha}} = |g|^2 \frac{m_4^2}{32\pi E_{\nu_\alpha}}. \tag{3.27}$$

- **Majorana neutrinos:** There are four decay options for Majorana neutrinos:  $\nu_\alpha \rightarrow \nu_\beta$ ,  $\bar{\nu}_\alpha \rightarrow \bar{\nu}_\beta$ , which we will point with a ‘+’ index in the probability expression, and

$\nu_\alpha \rightarrow \bar{\nu}_\beta$ ,  $\bar{\nu}_\alpha \rightarrow \nu_\beta$ , which we will point with a ‘-’ index. Assuming the same conditions of energy and baseline described in the previous item, the differential probabilities that an (anti)neutrino of flavour  $\nu_\alpha$  with energy  $E_{\nu_\alpha}$  is converted into an (anti)neutrino of flavor  $\nu_\beta$  with energy in the interval  $[E_{\nu_\beta}, E_{\nu_\beta} + dE_{\nu_\beta}]$  after travelling a distance  $L$  is:

$$\left[ \frac{dP_{\nu_\alpha \rightarrow \nu_\beta}^{(-)(-)\text{Majorana}}(E_{\nu_\alpha})}{dE_{\nu_\beta}} \right]_{\text{SB}}^+ = \left( |U_{\alpha 4}|^2 |U_{\beta 4}|^2 \quad (\alpha \neq \beta) \text{ or } (1 - |U_{\alpha 4}|^2)^2 \quad (\alpha = \beta) + \right. \\ \left. + |U_{\alpha 4}|^2 |U_{\beta 4}|^2 e^{-\Gamma_4^{\text{Majorana}} L} \right) \delta(E_{\nu_\alpha} - E_{\nu_\beta}) + \\ + G_+^{\text{Majorana}}(E_{\nu_\alpha}, E_{\nu_\beta}) \left( 1 - e^{-\Gamma_4^{\text{Majorana}} L} \right) \quad (3.28)$$

or

$$\left[ \frac{dP_{\nu_\alpha \rightarrow \nu_\beta}^{(-)(-)\text{Majorana}}(E_{\nu_\alpha})}{dE_{\nu_\beta}} \right]_{\text{SB}}^- = G_-^{\text{Majorana}}(E_{\nu_\alpha}, E_{\nu_\beta}) \left( 1 - e^{-\Gamma_4^{\text{Majorana}} L} \right) \quad (3.29)$$

where

$$G_+^{\text{Majorana}}(E_{\nu_\alpha}, E_{\nu_\beta}) = 2 |U_{\alpha 4}|^2 \frac{1}{2} R_\beta \frac{E_{\nu_\beta}}{E_{\nu_\alpha}^2} = \frac{1}{2} G^{\text{Dirac}}(E_{\nu_\alpha}, E_{\nu_\beta}) \quad (3.30)$$

and

$$G_-^{\text{Majorana}}(E_{\nu_\alpha}, E_{\nu_\beta}) = 2 |U_{\alpha 4}|^2 \frac{1}{2} R_\beta \frac{E_{\nu_\alpha} - E_{\nu_\beta}}{E_{\nu_\alpha}^2}, \quad (3.31)$$

explicitly writing

$$\Gamma_4^{\text{Majorana}}(E_{\nu_\alpha}) = \sum_{\beta=e,\mu,\tau,s} |g_\beta|^2 2 \frac{m_4^2}{32\pi E_{\nu_\alpha}} = |g|^2 \frac{m_4^2}{16\pi E_{\nu_\alpha}}. \quad (3.32)$$

Figure 3.1 illustrates the behavior of the energy distributions described in  $G_\pm^{\text{Majorana}}$  functions. If we have a helicity-conserving process (left panel), the energy spectrum will be proportional to  $E_{\nu_\beta}/E_{\nu_\alpha}$ , leading the daughter particles to populate energies around the mother particle one. Notice this also happens in  $G^{\text{Dirac}}$ . If we have a helicity-flipping process (right panel), the energy spectrum will be proportional to  $1 - E_{\nu_\beta}/E_{\nu_\alpha}$ , which means the daughter particles will populate very low energies (around zero). The suppression of helicity-flipping process, mainly in the relativistic regime, is due to the angular momentum conservation.

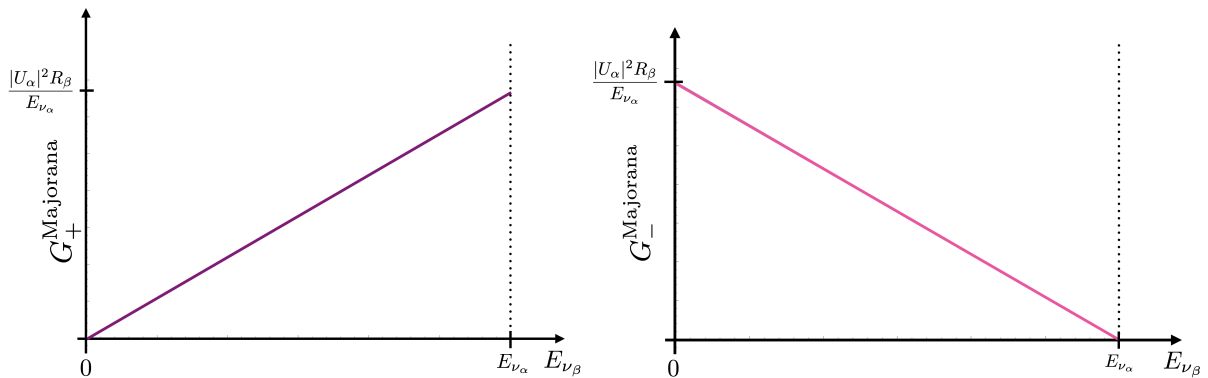


Figure 3.1: Behavior of the energy distribution functions described in  $G_{\pm}^{\text{Majorana}}$ . The helicity-conserving process (left panel) is described by  $G_+^{\text{Majorana}}$ , while helicity-flipping process (right panel) is described by  $G_-^{\text{Majorana}}$ .

As we mentioned before, the transition probabilities in Eq. 3.26, Eq. 3.28 and Eq. 3.29 work in short-baseline regime, in which LSND and MiniBooNE experiments operate. In order to maximize the effect of the heavy-neutrino decay at these experiments, we choose  $R_e = 1$ , i.e., all the decay products from  $\nu_4$  decay are electron (anti)neutrinos. We are also interested in  $\nu_4$  masses below a few MeV and neutrino energies characteristic of the MiniBooNE and LSND experiments. This means that all produced and the decay neutrinos are relativistic and emitted in the forward direction and inherit the angular distributions of the parent.

## 3.2 Heavy-Decay versus 3+1 Model

Qualitatively, it is easy to see why this hypothesis can outperform the standard (3+1)-oscillation hypothesis [123, 90, 124, 125]. In the (3+1)-oscillation scenario, considering the short-baseline limit:

$$\left[ P_{\nu_\mu \rightarrow \nu_e}^{3+1} \right]^{\text{SB}} = 4|U_{\mu 4}|^2 |U_{e4}|^2 \sin^2 \left( \frac{\Delta m_{41}^2 L}{4E_\nu} \right) \quad (3.33)$$

$$\left[ P_{\nu_\mu \rightarrow \nu_\mu}^{3+1} \right]^{\text{SB}} = 1 - 4|U_{\mu 4}|^2 (1 - |U_{\mu 4}|^2) \sin^2 \left( \frac{\Delta m_{41}^2 L}{4E_\nu} \right), \quad (3.34)$$

$$\left[ P_{\nu_e \rightarrow \nu_e}^{3+1} \right]^{\text{SB}} = 1 - 4|U_{e4}|^2 (1 - |U_{e4}|^2) \sin^2 \left( \frac{\Delta m_{41}^2 L}{4E_\nu} \right), \quad (3.35)$$

where  $\Delta m_{41}^2 \equiv m_4^2 - m_1^2$ . A sizable  $P_{\nu_\mu \rightarrow \nu_e}$  requires both a non-negligible  $|U_{\mu 4}|^2$  and  $|U_{e4}|^2$  which, in turn, are constrained by disappearance searches [119, 86, 87, 88, 89]. In the heavy-decay (HD) scenario (with  $R_e = 1$ ,  $R_\mu = 0$  and  $U_{e4} = 0$ ),

$$\left[ P_{\nu_\mu \rightarrow \nu_e}^{\text{HD}} \right]^{\text{SB}} = \int G(E_{\nu_e}) (1 - e^{-\Gamma_4 L}) dE_{\nu_e} \quad (3.36)$$

$$\left[ P_{\nu_\mu \rightarrow \nu_\mu}^{\text{HD}} \right]^{\text{SB}} = (1 - |U_{\mu 4}|^2)^2 + (|U_{\mu 4}|^2)^2 e^{-\Gamma_4 L} \quad (3.37)$$

$$\left[ P_{\nu_e \rightarrow \nu_e}^{\text{HD}} \right]^{\text{SB}} = 1 . \quad (3.38)$$

In the limit where  $\nu_4$  is very long-lived,  $\Gamma_4 L \ll 1$ ,  $P_{\nu_\mu \rightarrow \nu_\mu}^{\text{HD}} = 1 - 2|U_{\mu 4}|^2(1 - |U_{\mu 4}|^2)$ . This agrees with the  $\nu_\mu$  survival probability assuming there is a stable  $\nu_4$  and it is produced incoherently or, equivalently for the purposes of this setup, the new mass-squared difference is very large,  $\Delta m_{41}^2 L/E \gg 1$ , and the oscillations average out. Instead, in the limit where the decay is fast  $\Gamma_4 L \gg 1$ ,  $P_{\nu_\mu \rightarrow \nu_\mu}^{\text{HD}} = (1 - |U_{\mu 4}|^2)^2$ .

In terms of electron neutrino appearance, the role of  $|U_{e4}|^2$  in Eq.3.33 is played by  $G(1 - e^{-\Gamma_4 L})$ , with  $G \propto |U_{\mu 4}|^2$  in the heavy-decay scenario. It is important to mention that even for small values of  $|U_{\mu 4}|^2$  it is possible to produce enough electron neutrino appearance in SB (see Sec. 3.3). So, limits on muon neutrino disappearance will not necessarily put strong constraints in electron neutrino appearance searches. In addition,  $\Gamma_4$  is not constrained by  $\nu_e$ -disappearance. Instead, it is constrained by non-oscillation experiments, as we quickly summarize in the Subsection 3.2.1, and we find that reasonably large values of  $\Gamma_4 L$  are allowed for the  $L/E_\nu$  values of interest.

### 3.2.1 Constraints on New Neutrinos and Neutrino–Scalar Interactions

There are several bounds on the new-physics parameters we are introducing here:  $m_4$ ,  $g$  and  $|U_{\mu 4}|$ . We will discuss oscillation-related bounds in the Section 3.3 and here we summarize non-oscillation results.

Searches for neutral heavy leptons constrain  $|U_{\mu 4}|^2$  as a function of  $m_4$ . Keeping in mind that we are interested in constraints assuming  $\nu_4$  decays, as far as non-neutrino-oscillation experiments are concerned, invisibly,  $|U_{\mu 4}|^2 \lesssim 10^{-2}$  for  $m_4 \gtrsim 1$  MeV (see Refs. [130, 131] for recent quantitative analyses). The bounds are significantly weaker for smaller values of the  $m_4$ . For  $m_4 \simeq 1$  MeV, the strongest bounds come from precision measurements of pion ( $\pi \rightarrow \mu + \nu$ ) and kaon ( $K \rightarrow \mu + \nu$ ) decays. Bounds from  $\nu_\mu$  disappearance, as we will discuss in Sec. 3.3, are around  $|U_{\mu 4}|^2 \lesssim 10^{-2}$  for  $m_4 \gtrsim 10$  eV and hence will dominate for  $m_4 \lesssim 1$  MeV.

The couplings  $g$  of neutrinos to other neutrinos and a scalar particle, in the region of parameter space of interest here, are also best constrained by leptonic meson decays, especially the decays of pions and kaons (e.g.  $K \rightarrow \mu \nu \phi$ ). The bound on  $g$  depends on both the nature of the decay and on  $|U_{\mu 4}|^2$ . Here, conservatively, we use the results from Ref. [132], which translate into

$$g^2 |U_{\mu 4}|^2 < 1.9 \times 10^{-7}. \quad (3.39)$$

As far as short-baseline experiments, we are sensitive to  $|U_{\mu 4}|^2$  and  $\Gamma_4 \propto (gm_4)^2$ , see

Eq. 3.13 and Eq. 3.14. As will be discussed in great detail in the next couple of sections, we will be interested in  $(gm_4)^2|U_{\mu 4}|^2 \sim 1\text{eV}^2$  or

$$g^2|U_{\mu 4}|^2 \sim \left(\frac{1\text{ eV}}{m_4}\right)^2, \quad (3.40)$$

so the constrain in Eq. 3.39 can be easily satisfied for  $m_4 \gtrsim 10\text{ keV}$ . In summary, for  $1\text{ MeV} \gtrsim m_4 \gtrsim 10\text{ keV}$ , we expect to avoid all non-oscillation bounds with relative ease. We return to these in Sec. 3.3.

### 3.3 Simulations and Results

Here we provide details of the data we analyse and discuss how well they fit the heavy-neutrino decay hypothesis. We also discuss the details of our simulation of data from the SBN program and how sensitive it is to the heavy-decaying-neutrino hypothesis.

#### 3.3.1 LSND

The Liquid Scintillator Neutrino Detector, or LSND experiment [133] ran at the Los Alamos Neutron Science Center (LASCE) from 1993 to 1998. The experiment was designed to look for  $\bar{\nu}_e$  from a pion-decay-at-rest neutrino source [20]. LSND consisted of a cylindrical tank filled with 167 tons of mineral oil doped with a low concentration of liquid scintillator. This combination allows the detection of both Cherenkov and scintillation light, which are collected by 1220 photo-multiplier tubes (PMT) that surround the detector inner wall. Neutrinos are produced by the interaction of a 798 MeV proton beam with a production target, where positive pions stop at the beam dump and decay at rest into positive muons ( $\pi^+ \rightarrow \mu^+ + \nu_\mu$ ). The distance between the beam dump and the longitudinal center of LSND is 30 meters. The positive muons also decay at rest ( $\mu^+ \rightarrow e^+ + \nu_e + \bar{\nu}_\mu$ ). The Michel  $\bar{\nu}_\mu$  would lead to a  $\bar{\nu}_e$  signal in the presence of neutrino oscillations or other flavor-changing mechanism. The  $\bar{\nu}_e$  are detected via inverse beta decay (IBD),  $\bar{\nu}_e + p \rightarrow n + e^+$ , where the positron leads to Cherenkov and scintillation light inside mineral oil. The outgoing neutron manifests itself as subsequent scintillation light as it is captured on proton ( $n + p \rightarrow d + \gamma$ ) and a 2.2 MeV photon is emitted [118]. LSND makes use of this two-component signal to select a  $\bar{\nu}_e$ -candidate event sample. Figure 3.2 summarizes LSND layout, neutrino beam production and expected signal of  $\bar{\nu}_e$  event from flavor transition.

In 2001, LSND collaboration reported an excess of  $87.9 \pm 22.4$  (statistical uncertainties)  $\pm 6.0$  (systematical uncertainties) events above the expected background [20]. In the point of view of 3+1 Model (see Subsec. 1.3.1), those events are consistent with neutrino oscillations in the  $0.2 - 10\text{ eV}^2 \Delta m_{41}^2$  range. In order to validate our analysis procedure, we first fit the same 3+1 oscillation hypothesis and compare our results with those presented by the LSND collaboration [20]. In the same way as described in Section 2.3, we computed the expected number of events at the LSND detector implementing it in the GLoBES [112, 113] c-library. We calculate the event rates using the same compo-

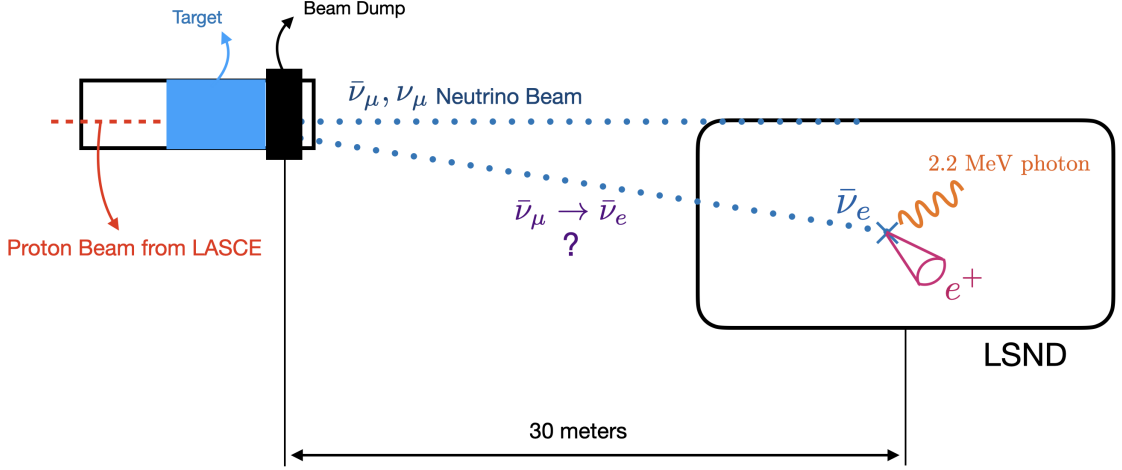


Figure 3.2: Layout of LSND and scheme of the neutrino beam production and the expected  $\bar{\nu}_e$  event signal from flavor transition mechanism inside the detector.

nents from Eq. 2.27. The LSND experiment only searches for neutrino flavor transition in the electron neutrino appearance channel. We will define the components of Eq. 2.27 as follows

- *Signal:* electron antineutrinos coming from muon antineutrino conversion ( $\bar{\nu}_\mu \rightarrow \bar{\nu}_e$ ) which interacts through IBD producing positrons in the detectors. Notice that for the heavy-decay neutrino hypothesis, we also need to consider the reaction ( $\nu_\mu \rightarrow \bar{\nu}_e$ ) in case of Majorana neutrinos. For 3+1-oscillation, the event rate per energy bin  $a$  for this channel sign is given by

$$[n_a^{\bar{\nu}_\mu \rightarrow \bar{\nu}_e}]_{3+1} = N_e \epsilon_a^e \int_{E_a - \Delta E_a/2}^{E_a + \Delta E_a/2} dE' \int_0^\infty dE \phi_{\bar{\nu}_\mu}(E) P_{\bar{\nu}_\mu \rightarrow \bar{\nu}_e}^{3+1}(E) \times \sigma_{\bar{\nu}_e + p \rightarrow n + e^+}(E) R^e(E, E'), \quad (3.41)$$

where ( $a = 1, \dots, 11$ ), the flux  $\phi_{\bar{\nu}_\mu}(E)$  from muon decay at rest in LSND was taken from Ref. [20], and we use the IBD cross-section from Ref. [134].  $P_{\bar{\nu}_\mu \rightarrow \bar{\nu}_e}^{3+1}(E)$  is given in Eq. 3.33 (with  $\sin^2 2\theta = 4|U_{\mu 4}|^2|U_{e 4}|^2$ ) and the energy resolution function  $R^e(E, E')$  is a Gaussian in the form

$$R^e(E, E') = \frac{1}{\sigma'(E)\sqrt{2\pi}} e^{-\frac{(E-E')^2}{2\sigma'^2(E)}} \quad (3.42)$$

with width of  $\sigma'(E) = 17\%/E[\text{MeV}]$ . The energy range for the neutrino event reconstruction extends from 20 MeV to 75 MeV with bin widths  $\Delta E_a$  as described below. After event reconstruction, we included an efficiency factor in order to mimic best-fit spectrum obtained by the LSND collaboration (Figure 24 of Ref. [20]) as follows

Detector	LSND
$N_e$	$1.92 \times 10^{-4}$
$\epsilon^e$	0.42
$\Delta E_a$ (MeV)	[1.4, 1.7, 1.9, 2.3, 2.7, 3.3, 4.2, 5.3, 7.2, 10, 15]

- *Background:* The LSND background sources come mainly from intrinsic beam  $\bar{\nu}_e$  and  $\bar{\nu}_\mu$  events and are summarized in Table VIII of Ref. [20]. We considered these fixed values for background composition.

In order to perform the statistical test between the events we expected in LSND from 3+1 model and the LSND data, we will perform the Log Likelihood Ratio  $\ell$  calculation. The function  $\ell$  we used for LSND is given by

$$\ell_{\text{LSND}} = \sum_{a=1}^{11} 2 \left[ \left( [(1+s)S_a^{\bar{e}} + (1+b)B_a^{\bar{e}}] - D_a^{\text{LSND}} \right) - D_a^{\text{LSND}} \log \frac{D_a^{\text{LSND}}}{[(1+s)S_a^{\bar{e}} + (1+b)B_a^{\bar{e}}]} \right] + \frac{s^2}{\rho_s^2} + \frac{b^2}{\rho_b^2} \quad (3.43)$$

where  $D_a^{\text{LSND}}$  represents the LSND data and  $S_a^{\bar{e}}$  is the the simulated signal for a chosen set of parameters from a *test* hypothesis (in our case, the 3+1 model) in the  $a$ -th energy bin. The  $B_a^{\bar{e}}$  is the estimated background by the LSND collaboration and was taken from Figure 24 of Ref. [20]. The nuisance parameters  $s, b$  denotes, respectively, signal and background fluctuations due to systematic errors in the flux normalization. Finally,  $\rho_s$  and  $\rho_b$  are, respectively, the signal and background standard deviations. Table 3.1 summarizes the LSND data and background expectation.

<b>LSND data</b>	[1.28, 0.02, -0.53, 4.55, 3.43, 6.39, 7.80, 8.24, 6.67, 9.64, 3.51]
<b>LSND background</b>	[0.06, 0.47, 0.93, 1.57, 1.72, 1.20, 2.59, 2.78, 2.54, 1.77, 0.46]

Table 3.1: LSND antineutrino neutrino events data and background expectation. The numbers were taken from Figure 24 of Ref. [20].

We perform a likelihood  $\ell$  analysis, including an overall normalisation error of 25% for signal and background. Our best-fit oscillation spectrum (green histogram), in 11 bins of  $L/E_\nu$ , is depicted in Fig. 3.3, along with the data and backgrounds published by the collaboration; the best-fit point for the oscillation analysis is  $(\sin^2 2\theta, \Delta m^2) = (0.0063, 7.2 \text{ eV}^2)$  and the minimum value of  $\chi^2$  is  $\chi_{\text{min}}^2 = 10.19$ . Given the eleven bins we included in our analysis (and hence nine degrees of freedom), we conclude that two-flavor-oscillations are a good fit to the LSND data, as expected. The allowed regions of the  $(\sin^2 2\theta, \Delta m^2)$  parameter space match well with those published by the LSND collaboration. With this agreement, we are confident we are capable of faithfully reproducing the data-analysis of LSND well enough to repeat the procedure for the heavy-decaying-neutrino hypothesis.

In the case of heavy-neutrino decay (HD), the parameters of the event rate expression will be the same as previously described, except with the transition probability. Therefore,

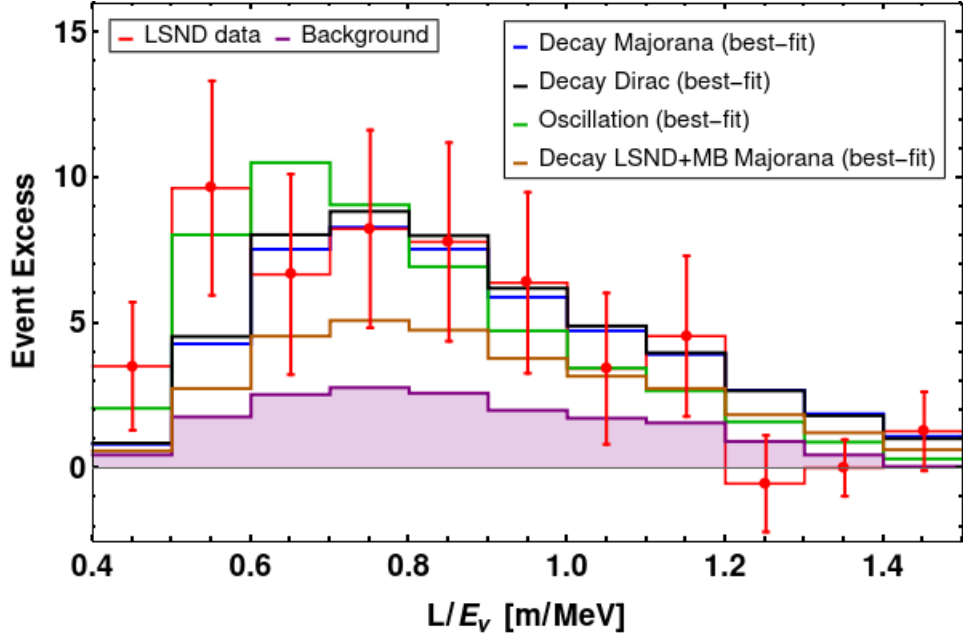


Figure 3.3: Best-fit  $\bar{\nu}_e$  spectra at LSND as a function of  $L/E_\nu$  for the oscillation hypothesis and for the different heavy-decaying-neutrino scenarios discussed here. The data points and the background spectrum are from the LSND collaboration report, presented in Ref. [20].

the neutrino event rate per energy bin  $a$  for LSND considering HD model will be given by

$$[n_a^{\bar{\nu}_\mu \rightarrow \bar{\nu}_e}]_{\text{HD}}^{\text{Dirac}} = N_e \epsilon_a^{\bar{\nu}_e} \int_{E_a - \Delta E_a/2}^{E_a + \Delta E_a/2} dE' \int_0^\infty dE \sigma_{\bar{\nu}_e + p \rightarrow n + e^+}(E) R^e(E, E') \times \int_E^\infty dE_{\bar{\nu}_\mu} \phi_{\bar{\nu}_\mu}(E_{\bar{\nu}_\mu}) \left[ \frac{dP_{\bar{\nu}_\mu \rightarrow \bar{\nu}_e}^{\text{Dirac}}(E_{\bar{\nu}_\mu})}{dE} \right]_{\text{SB}}, \quad (3.44)$$

for Dirac neutrinos and

$$[n_a^{(\bar{\nu}_\mu \rightarrow \bar{\nu}_e)}]_{\text{HD}}^{\text{Majorana}} = N_e \epsilon_a^{\bar{\nu}_e} \int_{E_a - \Delta E_a/2}^{E_a + \Delta E_a/2} dE' \int_0^\infty dE \sigma_{\bar{\nu}_e + p \rightarrow n + e^+}(E) R^e(E, E') \left( \int_E^\infty dE_{\bar{\nu}_\mu} \phi_{\bar{\nu}_\mu}(E_{\bar{\nu}_\mu}) \left[ \frac{dP_{\bar{\nu}_\mu \rightarrow \bar{\nu}_e}^{\text{Majorana}}(E_{\bar{\nu}_\mu})}{dE} \right]_{\text{SB}}^+ + \int_E^\infty dE_{\nu_\mu} \phi_{\nu_\mu}(E_{\nu_\mu}) \left[ \frac{dP_{\nu_\mu \rightarrow \bar{\nu}_e}^{\text{Majorana}}(E_{\nu_\mu})}{dE} \right]_{\text{SB}}^- \right) \quad (3.45)$$

for Majorana neutrinos. Notice that Eq. 3.44 and Eq. 3.45 have an extra integration on the mother particle energies. The fluxes  $\phi_{\nu_\mu}(E_{\nu_\mu})$  and  $\phi_{\bar{\nu}_\mu}(E_{\bar{\nu}_\mu})$  come, respectively, from pion and muon decays at rest. We generate neutrino event spectra for each set of decay parameters ( $|U_{\mu 4}|^2$ ,  $gm_4$ ) and attempt to fit them to the LSND data, using a Log Likelihood Ratio fit. The best-fit spectra in the case of Dirac and Majorana neutrinos are depicted, respectively, in black and blue in Fig. 3.3. We will denote  $g_M$  for Majorana

neutrinos and  $g_D$  for Dirac ones in the allowed region plots. The results for the two hypotheses are very similar. The Majorana and Dirac cases are, in practice, identical, except for the fact that  $G_+^{\text{Majorana}} = 0.5 G^{\text{Dirac}}$  (see Eq. 3.30). In the Majorana case, there is an antineutrino signal from  $\nu_4 \rightarrow \bar{\nu}_e \phi$  decays, but these are too low-energy and do not contribute significantly to the number of events. Since the effect of the decay is proportional to  $G$ , the Majorana case can compensate Dirac case by changing  $|U_{\mu 4}|^2$  by a factor of two. The  $\nu_4$  produced in DAR are monochromatic, with energy around 30 MeV. Hence, the  $\bar{\nu}_e$  produced in  $\nu_4 \rightarrow \bar{\nu}_e \phi$  have very low energies and only populate the highest  $L/E_\nu$ -bins. The situation is made worse by the fact that the energy spectrum of the daughter  $\bar{\nu}_e$  from the neutrino decay is soft, peaking (linearly) at zero energy (see Fig. 3.1). The overall result is that most  $\bar{\nu}_e$  from  $\nu_4 \rightarrow \bar{\nu}_e \phi$  have too low energy to significantly contribute to the LSND excess.

The best fit point falls in the region where the decay is fast so that, to zeroth order, all  $\nu_4$  decay between production and detection. We estimate the goodness-of-fit by comparing  $\chi_{\text{min}}^2 = 19.53$  (20.17) in the Dirac (Majorana) cases with nine degrees of freedom and conclude the fit is acceptable (p-value around two percent). The quality of this fit is worse than that of the oscillation fit. This is due to fact that the energy spectrum of the daughter  $\bar{\nu}_e$  is distorted towards lower energies compared with the energy spectrum of the parent  $\bar{\nu}_4$ . The allowed regions of the parameter space, along with the best-fit points, are depicted in Fig. 3.4. Solid, dashed and dotted lines represent, respectively, the 99%, 95% and 68% C.L. curves. As advertised, the results of the two decay scenarios are similar once one rescales the value of  $|U_{\mu 4}|^2$  by a factor of 2.

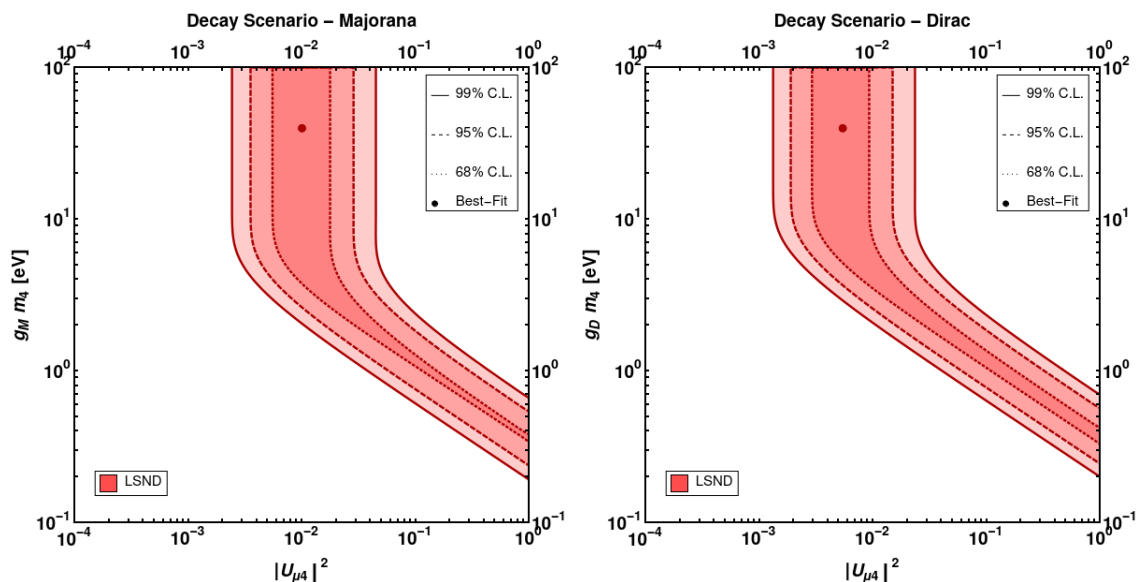


Figure 3.4: Allowed regions of the  $(|U_{\mu 4}|^2, g m_4)$  parameter space when the heavy-neutrino decay hypothesis is matched against the LSND data assuming Majorana (left) or Dirac neutrinos (right). The dots indicate the best-fit-point and the lines represent the 99% (solid), 95% (dashed) and 68% (dotted) confidence level (C.L.) curves.

### 3.3.2 MiniBooNE

The MiniBooNE experiment was designed to test the oscillation interpretation of the LSND data [135]. It consisted of a spherical tank filled with 800 tons of mineral oil and internally covered with 1280 PMTs to collect, mostly, Cherenkov light. The MiniBooNE detector is located 540 meters downstream from the neutrino source. In order to generate a neutrino flux, the booster neutrino beam (BNB), located at Fermilab, delivers 8.89 GeV protons that interact with a beryllium target. Charged mesons, like pions and kaons, are then produced and decay predominantly into muon neutrinos and antineutrinos. A magnetic focusing horn was used to sign-select the charged mesons, allowing, depending on the polarity of the horn, two neutrino-beam configurations: 1) *neutrino mode*: positively-charged mesons are focused to create a high-intensity flux of neutrinos; 2) *antineutrino mode*: negatively-charged mesons are focused to create a high-intensity flux of antineutrinos. MiniBooNE measures both  $\nu_e$  and  $\nu_\mu$ , plus their antiparticles, and is sensitive to  $\nu_e$  and  $\bar{\nu}_e$  appearance and  $\nu_\mu$  and  $\bar{\nu}_\mu$  disappearance.  $\nu_{\mu,e}$  and  $\bar{\nu}_{\mu,e}$  are identified as they scatter through the charged-current quasielastic (CCQE) process, yielding  $\mu^\pm, e^\pm$ , respectively. These particles emit Cherenkov and scintillation light inside the detector, and muon-candidates are distinguished well from electron-candidates due to the light topology of the events inside MiniBooNE detector: muon-like events form solid ring patterns, while electron-like events form ‘smeared’ rings. This occurs because electron trajectory suffers deflections while it propagates through mineral oil.

A summary of neutrino production in *neutrino mode* configuration and the topologies of  $\mu^\pm$  and  $e^\pm$  events inside MiniBooNE detector can be found in Figure 3.5. Since 2007, MiniBooNE collaboration has reported the searches of electron (anti)neutrino appearance and muon (anti)neutrino disappearance [59, 136, 137, 60, 138, 61, 120] in which a total excess of  $638.0 \pm 132.8$  (statistical and systematical errors) electron-like events were recorded in the detector. Although MiniBooNE excess can support LSND results in terms of signs of electron (anti)neutrino appearance, the absence of significant muon (anti)neutrino disappearance reported in Ref. [136] put limits in the disappearance searches.

We analyse MiniBooNE appearance data collected when the neutrino-beam was running in both neutrino and antineutrino modes [61, 139]. The MiniBooNE data set corresponds to  $12.84 \times 10^{20}$  protons on target (POT) in neutrino mode and  $11.27 \times 10^{20}$  POT in the antineutrino mode. We analyse the different data sets separately and combined. As in the LSND case, we first fit the MiniBooNE neutrino-mode and antineutrino-mode data with the 3+1 oscillation hypothesis, although we will skip this analysis description and directly describe the event rates and analysis using the heavy decay scenario. We simulate MiniBooNE events in GloBES, where we calculate the event rates with the same components from Eq. 2.27. For both beam configurations, we define the signal and background constituents for MiniBooNE as follows

- *Signal*: electron (anti)neutrinos coming from muon (anti)neutrino conversion ( $\nu_\mu \rightarrow \nu_e$ ) which interacts through CCQE producing electrons and positrons in the detector. The event rate for this channel signal per energy bin  $a$  is given by

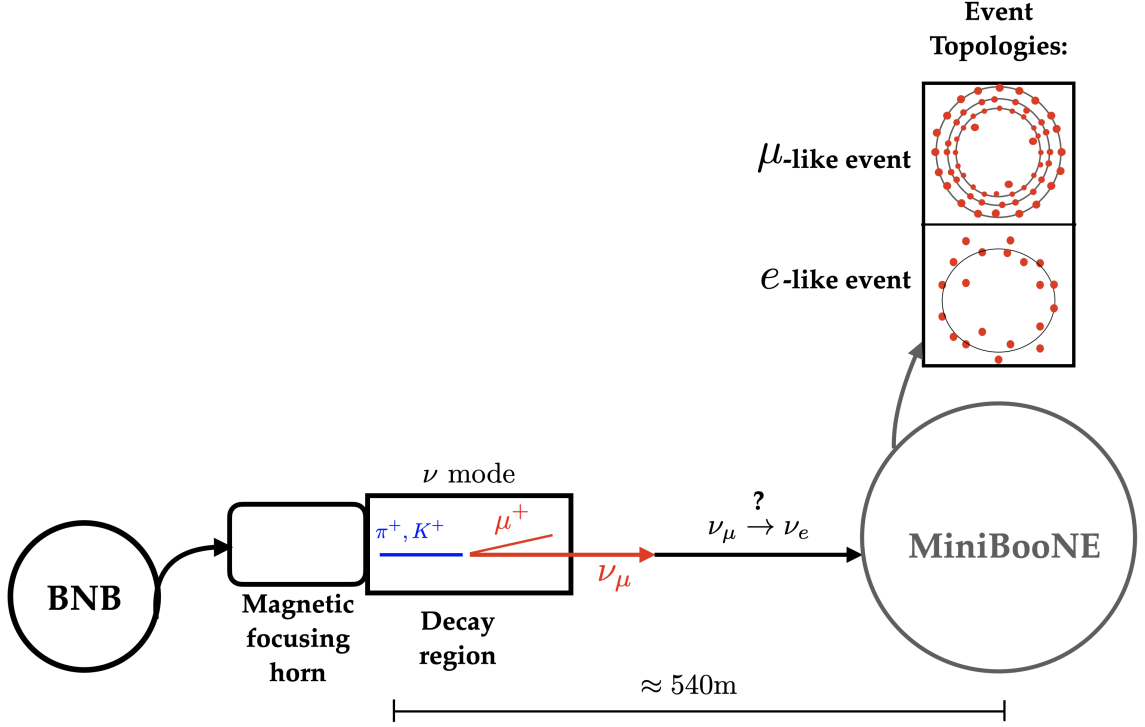


Figure 3.5: Illustration of neutrino production in BNB facility for *neutrino mode* configuration and event topologies inside MiniBooNE detector. After colliding with Beryllium target, positive charged mesons are selected by the magnetic focusing horn and they decay into muon neutrinos in Decay region.  $\mu^-$  and  $e^-$  from CCQE neutrino interactions in mineral oil produce Cherenkov light which is recorded by PMTs that surround MiniBooNE detector.

$$[n_a^{\nu_\mu \rightarrow \nu_e}]_{\text{HD}}^{\text{Dirac}} = N'_e \epsilon'_e \int_{E_a - \Delta E_a/2}^{E_a + \Delta E_a/2} dE' \int_0^\infty dE \sigma_{\nu_e \rightarrow \text{oil}}^{\text{CCQE}}(E) R'^e(E, E') \times \int_E^\infty dE_{\nu_\mu} \phi_{\nu_\mu}(E_{\nu_\mu}) \left[ \frac{dP_{\nu_\mu \rightarrow \nu_e}^{\text{Dirac}}(E_{\nu_\mu})}{dE} \right]_{\text{SB}}, \quad (3.46)$$

and

$$[n_a^{\bar{\nu}_\mu \rightarrow \bar{\nu}_e}]_{\text{HD}}^{\text{Dirac}} = N'_e \epsilon'_e \int_{E_a - \Delta E_a/2}^{E_a + \Delta E_a/2} dE' \int_0^\infty dE \sigma_{\bar{\nu}_e \rightarrow \text{oil}}^{\text{CCQE}}(E) R'^e(E, E') \times \int_E^\infty dE_{\bar{\nu}_\mu} \phi_{\bar{\nu}_\mu}(E_{\bar{\nu}_\mu}) \left[ \frac{dP_{\bar{\nu}_\mu \rightarrow \bar{\nu}_e}^{\text{Dirac}}(E_{\bar{\nu}_\mu})}{dE} \right]_{\text{SB}}, \quad (3.47)$$

for Dirac neutrinos and

$$\begin{aligned}
\left[ n_a^{(\nu_\mu \rightarrow \nu_e)} \right]_{\text{HD}}^{\text{Majorana}} &= N'_e \epsilon'^e \int_{E_a - \Delta E_a/2}^{E_a + \Delta E_a/2} dE' \int_0^\infty dE \sigma_{\nu_e \rightarrow \text{oil}}^{\text{CCQE}}(E) R'^e(E, E') \left( \int_E^\infty dE_{\nu_\mu} \right. \\
&\times \left. \phi_{\nu_\mu}(E_{\nu_\mu}) \left[ \frac{dP_{\nu_\mu \rightarrow \nu_e}^{\text{Majorana}}(E_{\nu_\mu})}{dE} \right]_{\text{SB}}^+ + \int_E^\infty dE_{\bar{\nu}_\mu} \phi_{\bar{\nu}_\mu}(E_{\bar{\nu}_\mu}) \left[ \frac{dP_{\bar{\nu}_\mu \rightarrow \nu_e}^{\text{Majorana}}(E_{\bar{\nu}_\mu})}{dE} \right]_{\text{SB}}^- \right)
\end{aligned} \tag{3.48}$$

and

$$\begin{aligned}
\left[ n_a^{(\bar{\nu}_\mu \rightarrow \bar{\nu}_e)} \right]_{\text{HD}}^{\text{Majorana}} &= N'_e \epsilon'^e \int_{E_a - \Delta E_a/2}^{E_a + \Delta E_a/2} dE' \int_0^\infty dE \sigma_{\bar{\nu}_e \rightarrow \text{oil}}^{\text{CCQE}}(E) R'^e(E, E') \left( \int_E^\infty dE_{\bar{\nu}_\mu} \right. \\
&\times \left. \phi_{\bar{\nu}_\mu}(E_{\bar{\nu}_\mu}) \left[ \frac{dP_{\bar{\nu}_\mu \rightarrow \bar{\nu}_e}^{\text{Majorana}}(E_{\bar{\nu}_\mu})}{dE} \right]_{\text{SB}}^+ + \int_E^\infty dE_{\nu_\mu} \phi_{\nu_\mu}(E_{\nu_\mu}) \left[ \frac{dP_{\nu_\mu \rightarrow \bar{\nu}_e}^{\text{Majorana}}(E_{\nu_\mu})}{dE} \right]_{\text{SB}}^- \right)
\end{aligned} \tag{3.49}$$

for Majorana neutrinos, where ( $a = 1, \dots, 11$ ). The fluxes  $\phi_{\nu_\mu}(E_{\nu_\mu})$  and  $\phi_{\bar{\nu}_\mu}(E_{\bar{\nu}_\mu})$  were taken from Ref. [140], the CCQE cross-section information was pre-implemented in GLOBES and the energy resolution function  $R'^e(E, E')$  is a Gaussian in the form of Eq. 3.42 with width of  $\sigma'(E) = 30\%/\sqrt{E[\text{GeV}]}$ . The energy range for the neutrino event reconstruction extends from 0.2 GeV to 3 GeV with bin widths  $\Delta E_a$  as described below. After event reconstruction, we included the signal detection efficiencies for electron-like events from Ref. [141] and a normalisation factor as follows

Detector	MiniBooNE
$N'_e$	$8.87 \times 10^{16}$
$\epsilon'^e$	Ref. [141]
$\Delta E_a$ (GeV)	[0.1, 0.075, 0.125, 0.125, 0.15, 0.15, 0.15, 0.15, 0.15, 0.25, 1.5]

- *Background:* Background events are summarized in Table 1 and Figure 1 of Ref. [61]. Neutral current events are, strictly speaking, impacted by the  $\nu_4$  decay, but the effect is negligible in the region of the parameter space in which we are interested. Changes to the neutral current (NC) event rate in this scenario are proportional to the maximum muon neutrino to sterile neutrino transition probability  $P_{\nu_\mu \rightarrow \nu_s}^{\text{max}}$ , i.e when  $\Gamma_4 L \gg 1$ , given by

$$P_{\nu_\mu \rightarrow \nu_s}^{\text{max}} \leq 1 - \left[ P_{\nu_\mu \rightarrow \nu_\mu}^{\text{HD}} \right]_{\text{SB}} - \left[ P_{\nu_\mu \rightarrow \nu_e}^{\text{HD}} \right]_{\text{SB}} - \left[ P_{\nu_\mu \rightarrow \bar{\nu}_e}^{\text{HD}} \right]_{\text{SB}} \sim |U_{\mu 4}|^2 (1 - |U_{\mu 4}|^2) \tag{3.50}$$

using Eq. (3.37) and (3.36). This is small when  $|U_{\mu 4}|^2$  or  $1 - |U_{\mu 4}|^2$  is small which, as we discuss in subsequent sections, is constrained to be small. Hence, we do not include decay effects in the background events.

## Details on the MiniBooNE analysis

In our  $\chi^2$  analysis for neutrinos and anti-neutrinos, we take statistical and systematic errors into account by using the official MiniBooNE covariance matrices, available in Ref. [139]. These include correlations among  $\nu_e$  ( $\bar{\nu}_e$ ) signal and background events and  $\nu_\mu$  ( $\bar{\nu}_\mu$ ) events for the neutrino (antineutrino) mode. In the combined analysis, the correlations among all neutrino and antineutrino samples are considered. Here, we are going to describe the neutrino-only analysis, but the step works to antineutrino-only and combined analysis as well. In order to perform MiniBooNE analysis to heavy-neutrino decay model (or 3+1 model, to validate our implementation), we generated an event spectrum correspondent to each set of parameters of the model. After simulating the events, we analyse our ‘‘pseudo’’ data with the  $\chi^2$  function defined by

$$\chi_{\text{MiniBooNE}}^2 = \sum_{i,j=1}^{N_e+N_\mu} (D_i - P_i) \mathcal{M}_{ij}^{-1} (D_j - P_j) \quad (3.51)$$

where:

- $N_e$  is the number of the energy bins related to the observed electron neutrino CCQE events;
- $N_\mu$  is the number of the energy bins related to the observed muon neutrino CCQE events;
- $D_i$  is the element of a vector  $D$  that contains  $N_e + N_\mu$  entries. The first  $N_e$  entries correspond to the number of observed electron neutrino CCQE events in each of the  $N_e$  energy bins. The followed  $N_\mu$  entries correspond to the number of observed muon neutrino CCQE events in each of the  $N_\mu$  energy bins;
- $P_i$  is the element of a vector  $P$  that contains  $N_e$  entries of our predicted signal  $S_i$  plus the estimated background  $B_i$  for the electron neutrino events, followed by  $N_\mu$  entries of the estimated muon neutrino events  $M_i$  at MiniBooNE detector;
- $\mathcal{M}_{ij}^{-1}$  is the inverse of the total  $(N_e + N_\mu) \times (N_e + N_\mu)$  covariance matrix  $\mathcal{M}_{ij}$ , which includes all systematic and statistical uncertainties for the predicted events at vector  $P$ , and bin-to-bin systematic correlations.

The information about the number of the energy bins, the full content of the vector  $D$ , and the estimated electron neutrino background  $B_i$  as well as muon neutrino CCQE events  $M_i$  presented in vector  $P$  were given by MiniBooNE collaboration at Ref. [139]. The covariance matrix  $\mathcal{M}_{ij}$  must be obtained from vectors  $D$  and  $P$  and from the available *fractional systematics-only covariance matrix* also given by the collaboration at Ref. [139].

To derive  $\mathcal{M}_{ij}$ , we followed the step-by-step description available in Ref. [142]. We are going to define the *fractional systematics-only covariance matrix* as  $\mathcal{M}_{kl}^{\text{frac}}$ . It consists of a  $(N_e + N_e + N_\mu) \times (N_e + N_e + N_\mu)$  block matrix which has the form (full  $\nu_\mu \rightarrow \nu_e$  conversion,  $\nu_e$  BG,  $\nu_\mu$ ), where

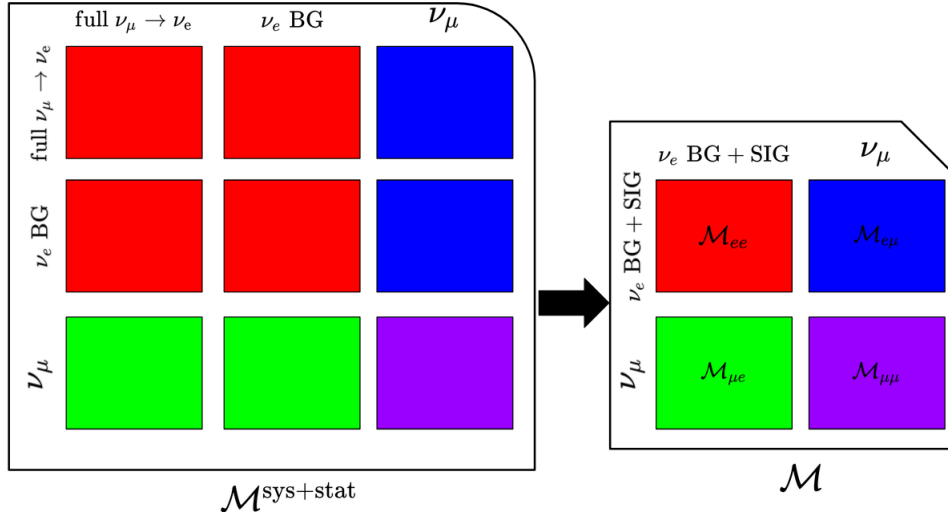


Figure 3.6: Color scheme to collapse the matrix  $\mathcal{M}^{\text{sys+stat}}$  (left) into the matrix  $\mathcal{M}$  (right) by overlapping blocks with the same color. Observe that the final matrix  $\mathcal{M}$  is divided in the sub-blocks  $\mathcal{M}_{ee}$ ,  $\mathcal{M}_{\mu\mu}$ ,  $\mathcal{M}_{e\mu}$  and  $\mathcal{M}_{\mu e}$ , which will be useful in the performance of electron neutrino appearance analysis.

- **full  $\nu_\mu \rightarrow \nu_e$  conversion:** full  $\nu_e$  transmutation events from  $\nu_\mu$  flux. It consists of the initial  $\nu_\mu$  a hundred percent converted in  $\nu_e$  and then reconstructed and selected according to  $\nu_e$  selection cuts;
- $\nu_e$  **BG:** estimated background  $B_i$  for the electron neutrino events.;
- $\nu_\mu$ : estimated muon neutrino CCQE events  $M_i$ .

First, we need to scale the matrix  $\mathcal{M}_{kl}^{\text{frac}}$  bin-by-bin to include the conversion probability correspondent to our signal. The resulting matrix  $\mathcal{M}_{kl}^{\text{sys}}$  is given by:

$$\mathcal{M}_{kl}^{\text{sys}} = \mathcal{M}_{kl}^{\text{frac}} \cdot (P'_k \cdot P'_l), \quad (3.52)$$

with  $k, l = 1, \dots, (N_e + N_e + N_\mu)$ . The vector  $P'$  contains  $N_e$  entries of our signal events  $S_i$ , followed by  $N_e$  entries of the estimated electron neutrino background  $B_i$  and  $N_\mu$  entries of the estimated  $\nu_\mu$  events  $M_i$ . Note that while  $P'$  has dimension  $(N_e + N_e + N_\mu)$ ,  $P$  has dimension  $(N_e + N_\mu)$ .

The statistical error from our signal prediction is included by adding the elements  $S_i$  to the diagonal elements of the  $\mathcal{M}_{k'l}^{\text{sys}}$  for  $k' = 1, \dots, N_e$ :

$$\mathcal{M}_{k'l}^{\text{sys+stat}} = \mathcal{M}_{k'l}^{\text{sys}} + \delta_{k'l} P'_k \quad (3.53)$$

Finally, we need to collapse the matrix  $\mathcal{M}_{kl}^{\text{sys+stat}}$  into  $\mathcal{M}_{ij}$  and invert it to  $\mathcal{M}_{ij}^{-1}$ . In order to collapse  $\mathcal{M}_{kl}^{\text{sys+stat}}$ , we follow the color pattern presented in Figure 3.6, where we have  $\mathcal{M}^{\text{sys+stat}}$  in the left and  $\mathcal{M}$  in the right. Each block with the same color has the same dimension. The collapse of the matrix  $\mathcal{M}^{\text{sys+stat}}$  means to overlap the blocks with the same color by *summing* the elements with the correspondent positions among the blocks.

Once we obtained the correct covariance matrix to perform our analysis, we want to select the portion of the  $\chi^2$  function that is related with the electron neutrino sample. Here, we are ultimately interested in the region of the parameter space where the impact of the new physics on  $\nu_\mu$ -disappearance is very small, thanks to strong bounds from other experiments, discussed in Sec. (3.3.4). Hence, the only impact of the  $\nu_\mu$  part of the data is to provide information concerning the neutrino flux and the neutrino scattering parameters. In other words, we are interested in gauging the impact of fitting the  $\nu_e$  and  $\bar{\nu}_e$  appearance data assuming the same new physics does not impact the  $\nu_\mu$  and  $\bar{\nu}_\mu$  data. In order to achieve this, we followed the prescription, discussed in Appendix E.4 of Ref. [143], of considering only the contribution of electron neutrino and antineutrino events (signal and background) in the fit, along with an extra component related to the uncertainty in the overall normalization of the spectrum. To do this, we define the appearance  $\chi_{\text{app}}^2$  function as:

$$\chi_{\text{app}}^2 = \chi^2 - C \quad (3.54)$$

where  $\chi^2$  contains all the information of matrix  $\mathcal{M}$  and  $C = (D_\mu - P_\mu)\mathcal{M}_{\mu\mu}^{-1}(D_\mu - P_\mu)$  includes only the systematic and statistical errors among muon neutrino events. The sub-block matrix  $\mathcal{M}_{\mu\mu}$  is defined in Figure 3.6 (purple sub-block). The quantity  $\chi_{\text{app}}^2$  is what we consider as a final result to our analysis and removes the “pure” muon neutrino correlations, although it is important to mention that correlation among electron and muon neutrino events is still taken into account in our MiniBooNE appearance analysis. We will use the minimum value of the  $\chi^2$  in order to gauge the goodness-of-fit, using the 11 bins to compute the number of degrees of freedom.

For the neutrino-mode data, our best-fit 3+1 oscillation spectrum (green histogram), in bins of  $E_\nu$ , is depicted in Fig. 3.7, along with the excess data published by the collaboration; the best-fit point for the oscillation analysis is  $(\sin^2 2\theta, \Delta m^2) = (0.83, 0.036 \text{ eV}^2)$  and the minimum value of  $\chi^2$  is  $\chi_{\text{min}}^2 = 9.46$ . Given the eleven bins we included in our analysis (and hence nine degrees of freedom), we conclude that 3+1 oscillations are a good fit to the MiniBooNE neutrino data, as expected. The allowed regions of the  $(\sin^2 2\theta, \Delta m^2)$  parameter space match very well those published by the MiniBooNE collaboration. We obtain similarly satisfactory results with the MiniBooNE antineutrino-mode data. With this agreement, we are confident we are capable of faithfully reproducing the data-analysis of MiniBooNE well enough to repeat the procedure for the heavy-neutrino decay hypothesis.

We generate neutrino event spectra for each set of decay parameters  $(|U_{\mu 4}|^2, gm_4)$  and attempt to fit them to the MiniBooNE data, using a  $\chi^2$ -fit. The best-fit spectra to neutrino-mode data, in the case of Dirac and Majorana neutrinos are depicted, respectively, in black and blue in Fig. 3.7.

For both neutrino-mode and antineutrino-mode data, the best fit point falls in the region where the decay is relatively slow. Hence, to zeroth order, a lower-energy  $\nu_4$  decay more often than a higher-energy  $\nu_4$ . For the neutrino mode, we estimate the goodness-

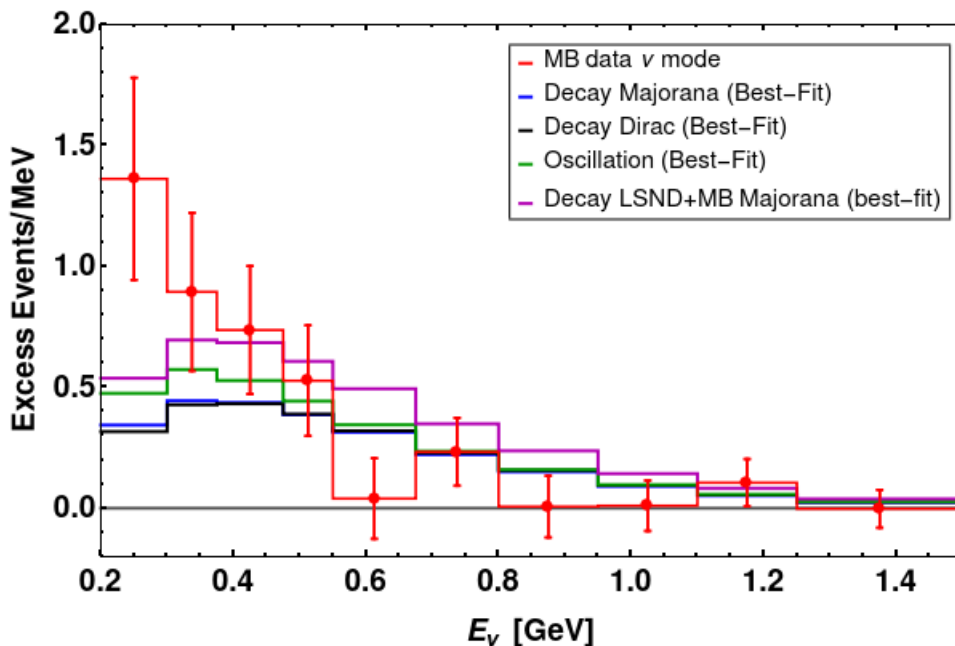


Figure 3.7: Best-fit  $\nu_e$  spectra at MiniBooNE, neutrino-mode, as a function of  $E_\nu$  for the oscillation hypothesis and for the different heavy-neutrino decay scenarios discussed here. The data points are from the MiniBooNE collaboration report, presented in Ref. [61]. The last bin corresponding to [1.5, 3.0] GeV is not shown here.

of-fit by comparing  $\chi^2_{\min}=11.08$  (11.56) in the Dirac (Majorana) cases with nine degrees of freedom and conclude the fit is acceptable. For the antineutrino-mode, we estimate the goodness-of-fit by comparing  $\chi^2_{\min}=7.71$  (6.66) in the Dirac (Majorana) cases with nine degrees of freedom and conclude the fit is also acceptable. The quality of these fits is similar to that of the oscillation fit. The allowed regions of the parameter space are depicted in Figs. 3.8 (neutrino mode), 3.9 (antineutrino mode), and 3.10 (neutrino and antineutrino modes combined).

Unlike the LSND case, as advertised, the results of the two decay scenarios are similar for roughly similar values of  $|U_{\mu 4}|^2$ . There is no obvious factor of two map between the Dirac and Majorana hypotheses, especially in the case of the antineutrino mode. This can be understood from the following. For the Majorana case, the channels which can in principle contribute to the observed event rates, for both neutrino and antineutrino runnings, are  $\nu_\mu \rightarrow \nu_e$ ,  $\nu_\mu \rightarrow \bar{\nu}_e$ ,  $\bar{\nu}_\mu \rightarrow \nu_e$  and  $\bar{\nu}_\mu \rightarrow \bar{\nu}_e$  (keeping in mind the facts that there is wrong-sign contamination<sup>2</sup> in both the fluxes and that the MiniBooNE detector cannot distinguish an  $e^-$  from an  $e^+$ ). For the Dirac neutrinos, the helicity-flipping channels are irrelevant. For Majorana neutrinos, in the case of neutrino-running, the wrong-sign contamination in the neutrino flux is tiny and therefore, there is negligible  $\bar{\nu}_\mu \rightarrow \nu_e$  or  $\bar{\nu}_\mu \rightarrow \bar{\nu}_e$  contribution to the event rates even if the transition probabilities for the helicity-flipping channel in Eq. (3.29) is comparable to the helicity-conserving one Eq. (3.28). For the antineutrino running, all four channels are relevant as the wrong-sign contamination in the antineutrino fluxes is rather large. In addition to the above arguments, one needs to take into account that the helicity-flipped daughter neutrinos peak softly; and the

<sup>2</sup>Presence of  $\bar{\nu}_\mu$  in  $\nu_\mu$ -flux and  $\nu_\mu$  in  $\bar{\nu}_\mu$ -flux.

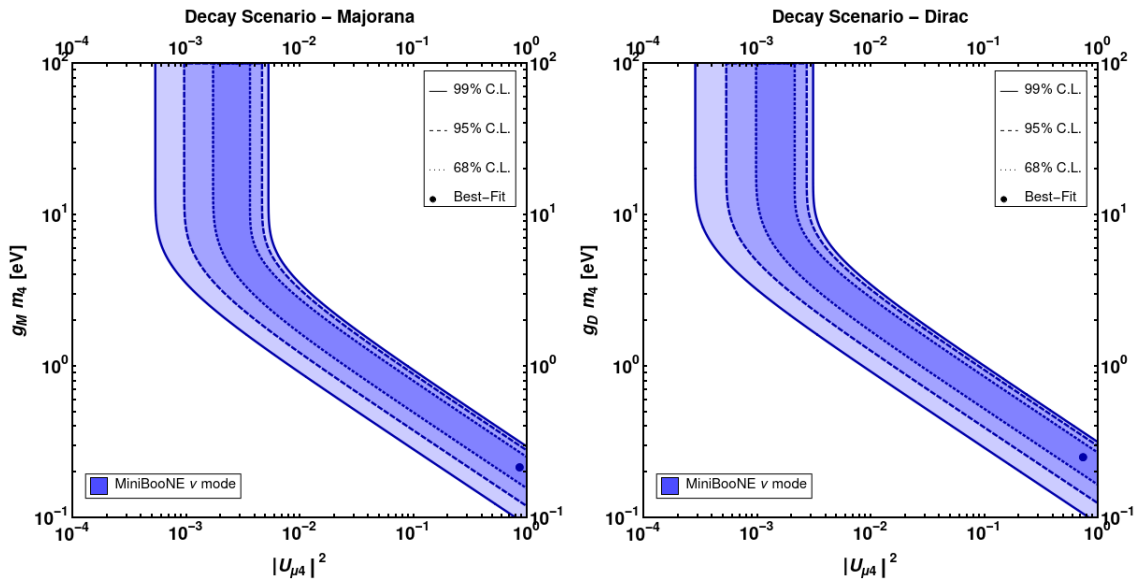


Figure 3.8: Allowed regions of the  $(|U_{\mu 4}|^2, g m_4)$  parameter space when the heavy-neutrino decay hypothesis is matched against the MiniBooNE neutrino-mode data assuming Majorana (left) or Dirac neutrinos (right). The dots indicate the best-fit-point and the lines represent the 99% (solid), 95% (dashed) and 68% (dotted) C.L. curves.

scattering cross-sections are different for neutrinos and antineutrinos. Thus, although  $G^{\text{Dirac}} = 2G_+^{\text{Majorana}}$ , the Majorana case surplus decay channels and/or increased scattering cross-sections balance-out the situation and ultimately, we observe that similar values of the parameters yield similar-quality fits for the Majorana and Dirac hypothesis, especially in the case of antineutrino-mode data.

### 3.3.3 LSND and MiniBooNE Combined

Next, we evaluate how well the heavy-neutrino decay hypothesis fits both LSND and MiniBooNE data by summing the  $\chi_{\text{MiniBooNE}}^2$  and  $\ell^{\text{LSND}}$  obtained in the two independent analyses. The LSND-only and MiniBooNE-only allowed regions of the parameter space are depicted in Fig. 3.11 to facilitate comparisons, along with the combined LSND+MiniBooNE allowed regions of the parameter space. The combined best-fit point, for the Dirac-neutrino scenario, is at  $(|U_{\mu 4}|^2, g_D m_4) = (0.063, 1.17 \text{ eV})$  and  $\chi_{\text{min}}^2 = 45.33$ . For 31 degrees of freedom (11+11+11-2), we estimate a p-value of several percent, which we deem to be reasonable. The event rates corresponding to the combined best-fit, for the Majorana-neutrino case are depicted in Figs. 3.3, for LSND (gold color) and 3.7, for MiniBooNE (neutrino-mode) (magenta). Note that the best-fit slightly undershoots the LSND data, and slightly overshoots those from MiniBooNE. The situation of the Majorana-neutrino scenario is similar; the quality of the fit is a little worse:  $\chi_{\text{min}}^2 = 48.34$ .

### 3.3.4 Disappearance searches: KARMEN and MINOS/MINOS+

Among the null-results presented in muon neutrino disappearance searches, the experiments KARMEN and MINOS/MINOS+ offer the most restrictive results in the parameter

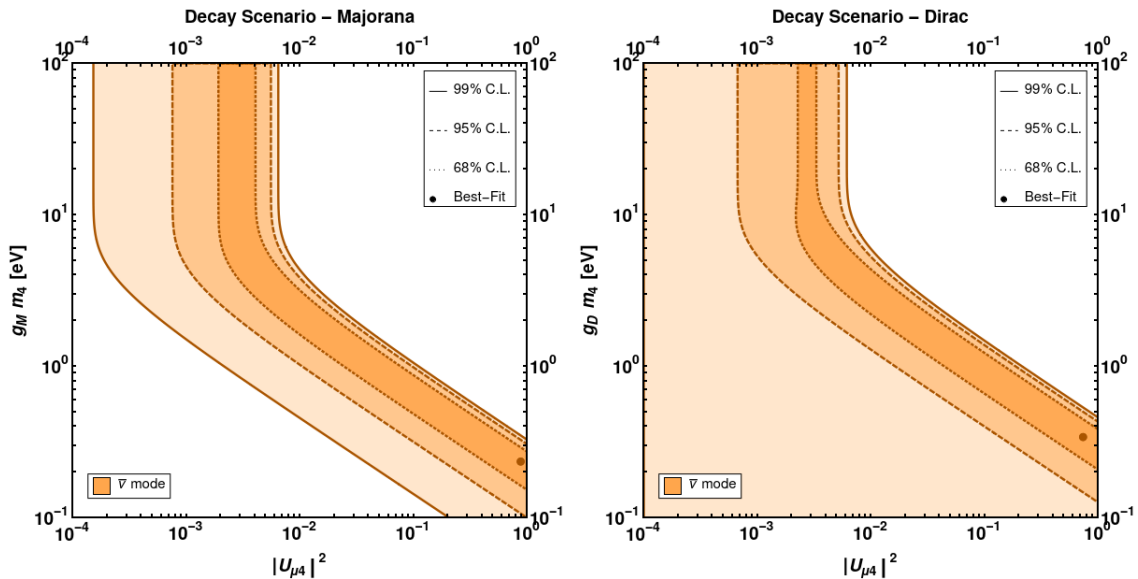


Figure 3.9: Allowed regions of the  $(|U_{\mu 4}|^2, g m_4)$  parameter space when the heavy-neutrino decay hypothesis is matched against the MiniBooNE antineutrino-mode data assuming Majorana (left) or Dirac neutrinos (right). The dots indicate the best-fit-point and the lines represent the 99% (solid), 95% (dashed) and 68% (dotted) C.L. curves

space of interest. We will briefly comment about the KARMEN and MINOS/MINOS+ experimental features and their impact in the analysis of the heavy-neutrino decay hypothesis.

The Karlsruhe Rutherford Medium Energy Neutrino, or KARMEN, ran at the spallation neutrino source ISIS of the Rutherford Laboratory in the UK. The experiment impinges 800 MeV protons on a water-cooled Ta – D<sub>2</sub>O target where  $\pi^+$  per incident proton are produced. These  $\pi^+$  are stopped completely and decay with a lifetime of  $\tau_\pi = 26$  ns within the heavy target producing  $\mu^+$  and  $\nu_\mu$ . The  $\mu^+$  produced also decays at rest within the target with a lifetime  $\tau_\mu = 2.2$   $\mu$ s giving  $e^+, \nu_e, \bar{\nu}_\mu$ . Due to this large time separation the  $\nu_\mu$  induced events can be cleanly separated from the  $\bar{\nu}_\mu$  or  $\nu_e$  induced events. The  $\bar{\nu}_\mu$  and  $\nu_e$  from the muon decay have a continuous spectra with the endpoint energy of 52.8 MeV. The data set corresponds to the experimental run from February 1997 to March 2001 [144], which gives a total of  $N_\nu = 2.71 \times 10^{21}$  neutrinos for each flavor. The KARMEN detector consists of a liquid scintillation calorimeter situated at a mean distance of 17.7 m from the ISIS target and has a high energy resolution of  $11.5\%/\sqrt{E(\text{MeV})}$ . KARMEN observed a total of 15 inverse beta decay events compared against a background expectation of 15.8. Thus, it observed a null result for the  $\bar{\nu}_\mu \rightarrow \bar{\nu}_e$  oscillations for  $L/E_\nu \sim 0.3 - 0.9$  m/MeV.

The analysis of the KARMEN data for the heavy-neutrino decay scenario is presented in Ref. [126] for both Dirac and Majorana case. The results were compiled in Fig. 3.11. KARMEN data set put constraints on the helicity-conserving  $\bar{\nu}_\mu \rightarrow \bar{\nu}_e$  decay channel as the events due to the helicity-flipping  $\nu_\mu \rightarrow \bar{\nu}_e$  channel are not included in this sample due to a precise information regarding the timing of the events.

MINOS [145] is a long-baseline superbeam experiment based at Fermilab. The source

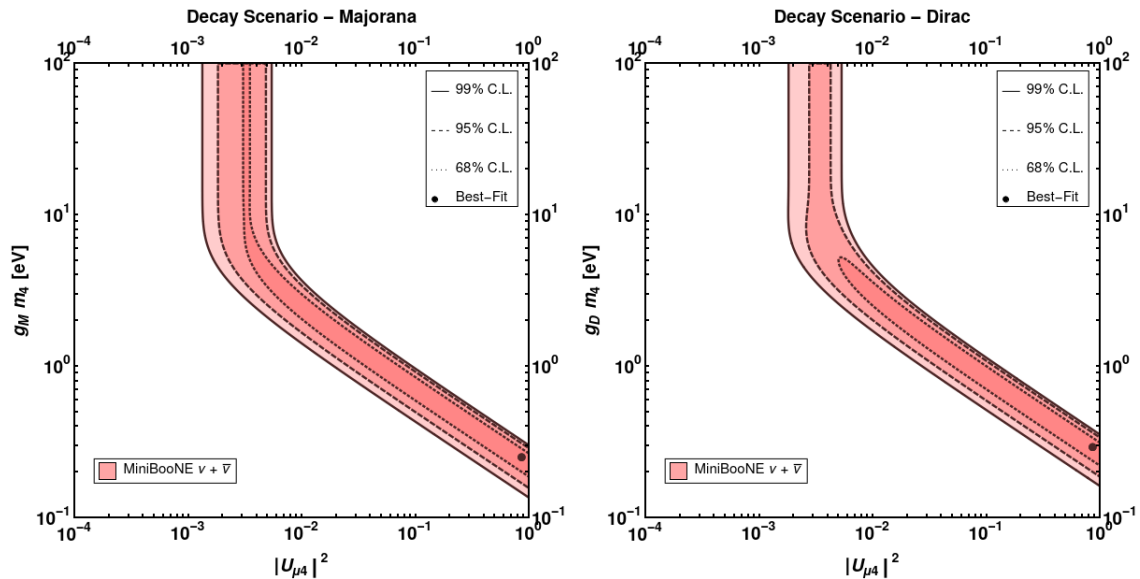


Figure 3.10: Allowed regions of the  $(|U_{\mu 4}|^2, g_M m_4)$  parameter space when the heavy-neutrino decay hypothesis is matched against the combined MiniBooNE neutrino-mode and antineutrino-mode data assuming Majorana (left) or Dirac neutrinos (right). The dots indicate the best-fit-point and the lines represent the 99% (solid), 95% (dashed) and 68% (dotted) C.L. curves.

of neutrinos is the NuMI beam facility at Fermilab [146]. The experimental setup consists of a 1 kton near detector situated 1.04 km downstream and a 5.4 kton far detector situated 735 km away, on-axis in the Soudan underground laboratory. The primary goal of the MINOS experiment was to confirm, with an accelerator-based  $\nu_\mu$ -beam, the evidence for  $\nu_\mu$ -disappearance first seen in atmospheric experiments, measure the oscillation parameters  $\sin^2 2\theta_{23}$  and  $|\Delta m_{32}^2|$ , and look for the subleading long-baseline  $\nu_e$ -appearance signal. For these purposes, MINOS looked at charged-current  $\nu_\mu$ -disappearance and  $\nu_e$ -appearance events in both neutrino and antineutrino modes [147]. It also measures neutral current events that are helpful in sterile-neutrino searches. Initially, MINOS operated with the low-energy tune of the NuMI beam that peaks at neutrino energies around 3 GeV. This was followed by running, referred to as MINOS+, with the medium-energy tune of the NuMI beam, where the flux peaks at neutrino energies around 7 GeV. The most recent sterile neutrino searches were presented in [86]. These results correspond to an exposure of  $10.56 \times 10^{20}$  POT for MINOS and  $5.80 \times 10^{20}$  POT for the MINOS+ experiment. Assuming the neutrino mass-eigenstates are stable, for  $m_4 \gg 10$  eV, the collaboration claims that the data constrain  $|U_{\mu 4}|^2 < 2.3 \times 10^{-2}$  at the 90% C.L. Here, we take this result at face value and apply it to the heavy-neutrino decay scenarios of interest.

Strictly speaking, the analysis presented in [86] does not apply if the  $\nu_4$  is unstable, for two reasons. One was already discussed in Sec. 3.2. If one ignores the daughters of the neutrino decay, the  $\nu_\mu$  survival probability depends on the  $\nu_4$  lifetime, see Eq. (3.37). However, the difference between a stable ( $\Gamma_4 L \ll 1$ ) and unstable  $\nu_4$ , as far as this contribution is concerned, is proportional to  $|U_{\mu 4}|^4$ , a factor  $|U_{\mu 4}|^2$  smaller than the leading contribution. Since MINOS(+) is sensitive to  $|U_{\mu 4}|^2$  values of order  $10^{-2}$ , the fact that  $\nu_4$  can decay is irrelevant for this contribution to the disappearance analysis. The other

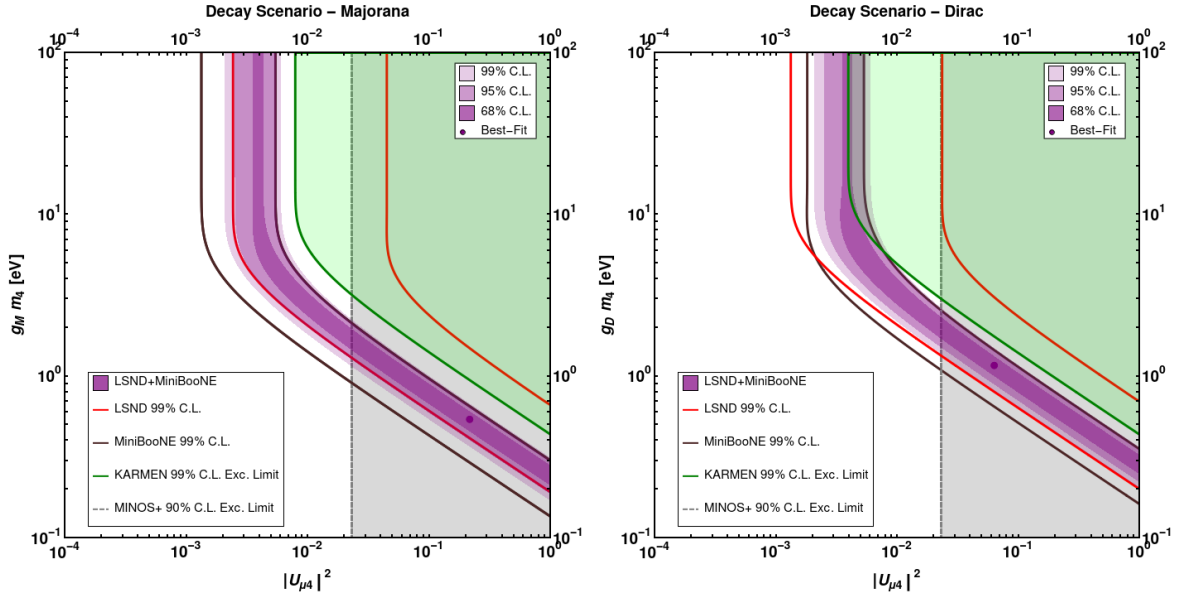


Figure 3.11: Allowed regions at 99% (lighter purple), 95% (medium purple) and 68% (darker purple) C.L. of the  $(|U_{\mu 4}|^2, gm_4)$  parameter space when the heavy-neutrino decay hypothesis is matched against the combined LSND data and MiniBooNE neutrino-mode and antineutrino-mode data assuming Majorana (left) or Dirac neutrinos (right). The dots indicate the best-fit-point. The region to the right of the vertical line is excluded by MINOS+ at the 90% C.L. [86]. The green shaded region on the top-right of the green line is excluded by KARMEN at the 99% C.L.

potential impact of the decay is that the daughter  $\nu_e$  of the  $\nu_4$  decay can oscillate into a  $\nu_\mu$  by the time it reaches the far detector. This extra contribution to the  $\nu_\mu$  survival probability is, relative to the leading  $|U_{\mu 4}|^2$ -effect, suppressed by  $|U_{e3}|^2 \sim 0.02$  and hence very small (see Sec. 1.2.1).

For the reasons discussed above, we take the constraint from the  $\nu_\mu$  disappearance data to be  $|U_{\mu 4}|^2 < 2.3 \times 10^{-2}$  at the 90% C.L. for all values of  $gm_4$  of interest. This is represented by a vertical line in Fig. 3.11. This constraint rules out the region of parameter corresponding to small  $gm_4$  but leaves behind a healthy portion of the parameter space, including values of  $gm_4$  small enough that the decay of  $\nu_4$  is not necessarily prompt for the energies of interest. Since the Dirac hypothesis points to relatively smaller values of  $|U_{\mu 4}|^2$ , the allowed region of parameter space is “larger” in this case.

One final note before proceeding. Given that, for large  $gm_4$ , we require  $|U_{\mu 4}|^2 \lesssim 10^{-2}$  (and independent of  $gm_4$ ), the bounds from meson leptonic decays on  $g$  and  $|U_{\mu 4}|^2$ , discussed in Sec. 3.2.1, translate into  $gm_4 \lesssim 1$  keV, saturated as  $m_4$  approaches 1 MeV.

Finally, we joined the null-disappearance results obtained by MINOS and KARMEN with the appearance results by LSND and MiniBooNE in one combined fit. The analysis was done by summing the  $\chi^2$  functions of LSND, MiniBooNE and KARMEN and adding an penalty factor of  $\chi_{\text{penalty}}^2 = 4.6 (|U_{\mu 4}|^2 / 2.3 \times 10^{-2})^2$  to describe the MINOS/MINOS+ constraint. The combined LSND+MiniBooNE+KARMEN+MINOS allowed regions of the parameter space are shown in Fig. 3.12. The combined best-fit point for Dirac case is at  $(|U_{\mu 4}|^2, g_D m_4) = (0.0086, 3.41 \text{ eV})$  with  $\chi_{\text{min}}^2 = 56.42$  and for Majorana case is at

$(|U_{\mu 4}|^2, g_M m_4) = (0.0086, 2.93 \text{ eV})$  with  $\chi_{\min}^2 = 58.45$ . Considering we have 40 degrees of freedom  $(11+11+11+9-2)$ , we estimate a reasonable fit for both physics scenarios.

### 3.3.5 SBN

Finally, we want to explore the potential of the Short-Baseline Neutrino (SBN) Program (see Sec. 2.2) to test the heavy-decay neutrino model scenarios discussed here. According to the proposal [111], the SBN Program is designed to address several anomalies in neutrino physics and will test, with the most sensitivity, the oscillation-interpretation to LSND and MiniBooNE data.

We performed a sensitivity analysis considering only the neutrino-mode running for the BNB. The decay rates for heavy-neutrino decay in SBN have the same format of Eq. 3.46 and Eq. 3.48, and all the components of SBN signal and background are described in Sec. 2.2 as well as the  $\chi_{\text{SBN}}^2$  function. We are considering only the  $\nu_e$ -appearance channel in order to estimate the sensitivity of the SBN Program. The uncertainty related to the flux normalization was set to 15%.

The sensitivity of the SBN Program is depicted in Fig. 3.12. The regions of the parameter space preferred by combined LSND and MiniBooNE are also depicted in order to facilitate comparisons. The SBN program can definitively test the heavy-neutrino to the LSND and MiniBooNE data.

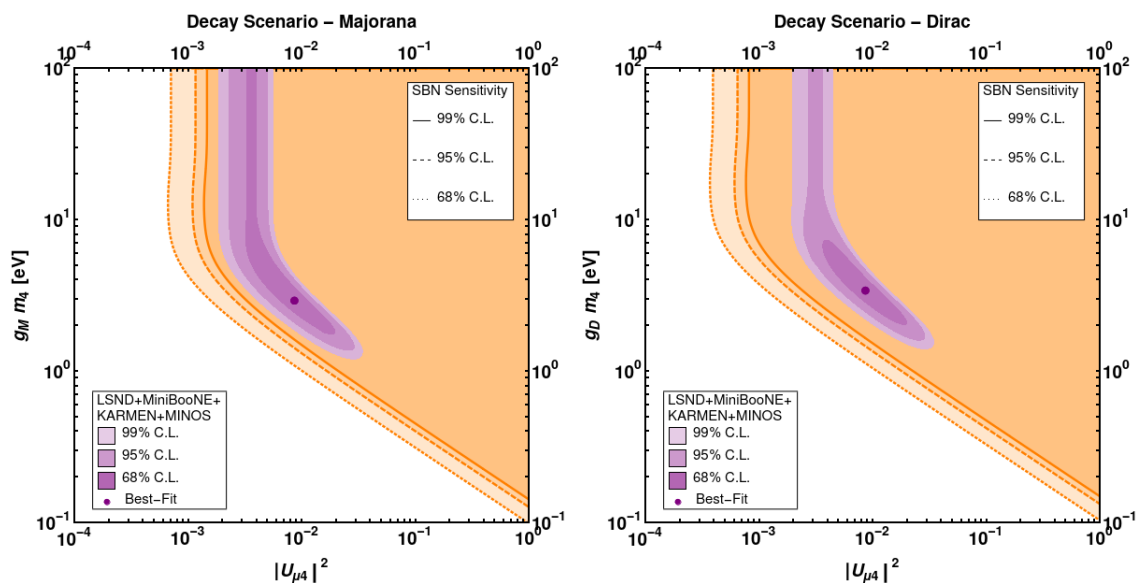


Figure 3.12: Allowed regions at 99% (lighter purple), 95% (medium purple) and 68% (darker purple) C.L. of the  $(|U_{\mu 4}|^2, g_M m_4)$  parameter space when the heavy-neutrino decay hypothesis is matched against the combined LSND, MiniBooNE and KARMEN data and MINOS constrains assuming Majorana (left) or Dirac neutrinos (right). The dots indicate the best-fit-point. In the same context, the orange regions indicate the sensitivity of the SBN Program at 99% (solid line), 95% (dashed line) and 68% (dotted line) C.L. for Majorana (left) and Dirac neutrinos (right).

### Sensitivity to non-zero neutrino decay effect on SBN

Assuming the considered heavy-neutrino decay model has a positive signal in SBN Program, we want to investigate now the capability of the experiment to measure the decay parameters ( $|U_{\mu 4}|^2, g m_4$ ). To perform this analysis, we generated neutrino events in the same “experimental” configuration of SBN previous sensitivity analysis (see Sec. 2.2), but assuming now the data is given by non-zero values to ( $|U_{\mu 4}|^2, g m_4$ ) parameters. For convenience, we will set the true values of the parameters at the correspondent best-fit points from LSND, MiniBooNE, KARMEN and MINOS combined analysis for Majorana and Dirac cases. The results we obtained are shown in Figure 3.13: we have the allowed regions consistent with the computed events at the best-fit point for both Majorana (left panel) and Dirac (right panel) assumptions at 68.3% of C. L. (dotted curve), 95% of C. L. (dashed curve) and 99% of C. L. (solid curve).

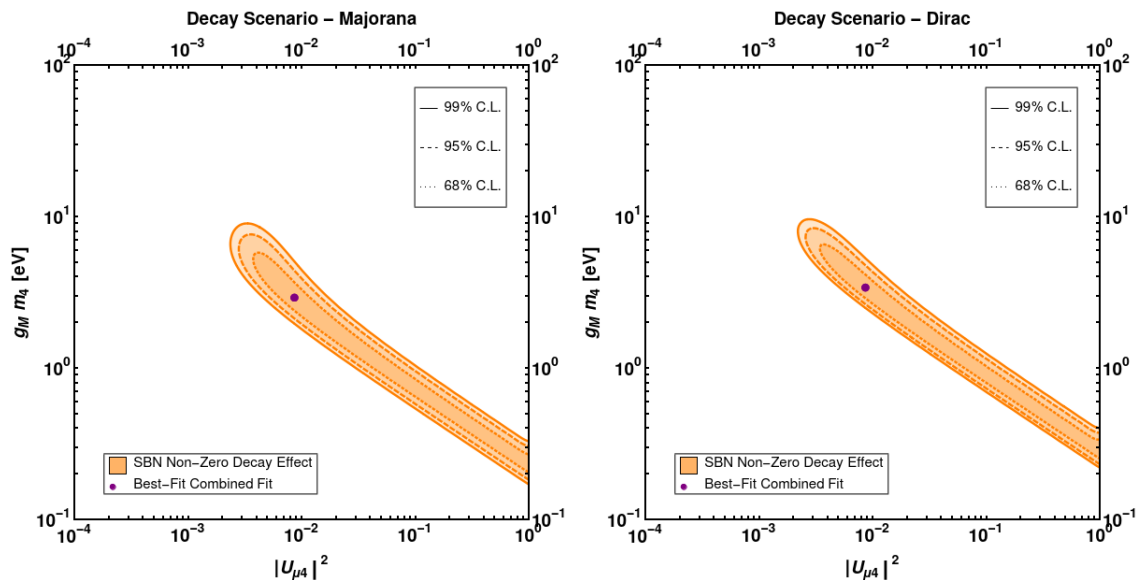


Figure 3.13: SBN allowed regions for non-zero decay scenario parameters ( $|U_{\mu 4}|^2, g m_4$ ) at 99% (solid line), 95% (dashed line) and 68% (dotted line) C.L. for Majorana (left) and Dirac neutrinos (right). The dots indicate the best-fit-point from the LSND, MiniBooNE, KARMEN and MINOS combined analysis.

## 3.4 Conclusions

The excess of  $\nu_e$ - and  $\bar{\nu}_e$ -candidate events at MiniBooNE and LSND remains unexplained. The, arguably, simplest solution – 3+1 neutrino-oscillation with a new mass-squared difference around  $1 \text{ eV}^2$  – is, however, severely constrained. If these data are indeed pointing to more new physics in the neutrino sector, it is likely that the new physics contains more ingredients than new neutrino mass-eigenstate that mix slightly with the active neutrinos. Here, we explored the hypothesis that there is a new neutrino mass-eigenstate  $\nu_4$  and a new very light scalar particle  $\phi$ .  $\nu_4$  and  $\phi$  interact in such a way that  $\nu_4 \rightarrow \nu_e \phi$ . Here, the excess of  $\nu_e$ - and  $\bar{\nu}_e$ -candidate events at MiniBooNE and LSND

are the daughter  $\nu_e$  and  $\bar{\nu}_e$  from  $\nu_4$  and  $\bar{\nu}_4$  decay. This hypothesis was first proposed in Ref. [127] in order to address the LSND anomaly.

We find a reasonable fit to the data of MiniBooNE and LSND, albeit the quality of the fit to only MiniBooNE and LSND data is not as good as the one obtained with the 3+1 neutrino-oscillations hypothesis. The heavy-neutrino decay hypothesis, however, can cleanly evade data from  $\nu_\mu$ -disappearance searches, which constrain  $|U_{\mu 4}|^2 \lesssim 10^{-2}$ , and is immune to searches involving  $\nu_e$ -disappearance. We find that precision measurements of meson leptonic decays can also be satisfied as long as  $1 \text{ MeV} \gtrsim m_4 \gtrsim 10 \text{ keV}$ . The SBN program at Fermilab should be able to definitively test the heavy-neutrino decay hypothesis. We considered two different decay scenarios, one with Majorana neutrinos, one with Dirac neutrinos. The MiniBooNE and LSND data are such that both models fit the data with very similar efficacy.

While the heavy-neutrino decay hypothesis explored here is not an excellent fit to both data sets – especially the LSND data – it seems to provide an interesting possibility. We hope the results presented here will inspire the collaborations – they are the only ones capable of performing a proper fit to their data – to investigate this possibility.

Other manifestations of the sterile-neutrino decay hypothesis have been, very recently, discussed in the literature, including [148, 149, 150]. The work presented here share several similarities with these efforts but we explore, for the most part, a different region of the – very large – space of heavy-neutrino decay models.

## Chapter 4

# Final Conclusions

The short-baseline experiments are very interesting tools to explore physics beyond the three neutrino oscillation scenario and beyond Standard Model. The introduction to a sterile neutrino in the neutrino mixing, enables a new oscillation phase that can handle with the short-baseline anomalies. However, severe constraints from muon neutrino disappearance in the short-baseline experiments challenge the consistence of the dubbed 3+1 model. In this Thesis, we look for models that also predict sterile neutrinos, but in other contexts.

First, we search for the manifestation of large extra dimension in the neutrino mixing. As right handed neutrinos are Standard Model singlets, they can freely propagate in the extra, compacted dimension. The consequences of having a 5-dimensional fermion field is the production of an infinite number of neutrino mass terms. These new mass states mix with the active flavors and interfere in the usual oscillation. We showed that the Short-Baseline Neutrino Program can entirely test the presence of large extra dimension in neutrino oscillations.

Second, we postulated that the fourth neutrino mass eigenstate of the 3+1 model mixing is unstable and decay into the three usual light neutrinos plus a massless scalar. We added an effective Yukawa interaction that leads this decay and test the model under the data of the LSND and MiniBooNE short-baseline detectors. We assume Dirac or Majorana nature for the neutrinos. We obtained reasonable fits for both cases and evaluate the constraints from precise leptonic decay measurements and from muon neutrino disappearance searches. We obtained a healthy region of parameters from the decay model that are consistent and can address the short-baseline anomalies. Finally, we could see that the SBN can fully test the allowed parameter region from decay model in the future.

# Bibliography

- [1] ICECUBE, *All about neutrinos*, 2013, Available at <http://icecube.wisc.edu/info/neutrinos>.
- [2] L. M. Brown, *The idea of the neutrino*, *Phys. Today* **31N9** (1978) 23–28.
- [3] W. Pauli, *Dear radioactive ladies and gentlemen*, *Phys. Today* **31N9** (1978) 27.
- [4] F. Reines and C. L. Cowan, *Detection of the free neutrino*, *Phys. Rev.* **92** (Nov, 1953) 830–831.
- [5] G. Danby, J. M. Gaillard, K. A. Goulianos, L. M. Lederman, N. B. Mistry et al., *Observation of High-Energy Neutrino Reactions and the Existence of Two Kinds of Neutrinos*, *Phys.Rev.Lett.* **9** (1962) 36–44.
- [6] M. L. Perl, G. S. Abrams, A. Boyarski, M. Breidenbach, D. Briggs et al., *Evidence for Anomalous Lepton Production in  $e^+ - e^-$  Annihilation*, *Phys.Rev.Lett.* **35** (1975) 1489–1492.
- [7] DONUT collaboration, K. Kodama et al., *Observation of tau neutrino interactions*, *Phys.Lett.* **B504** (2001) 218–224, [[hep-ex/0012035](https://arxiv.org/abs/hep-ex/0012035)].
- [8] B. Pontecorvo, *Mesonium and anti-mesonium*, *Sov.Phys.JETP* **6** (1957) 429.
- [9] Z. Maki, M. Nakagawa and S. Sakata, *Remarks on the Unified Model of Elementary Particles*, *Progress of Theoretical Physics* **28** (11, 1962) 870–880, [<https://academic.oup.com/ptp/article-pdf/28/5/870/5258750/28-5-870.pdf>].
- [10] L. Wolfenstein, *Neutrino oscillations in matter*, *Phys. Rev. D* **17** (May, 1978) 2369–2374.
- [11] S. P. Mikheev and A. Y. Smirnov, *Resonant amplification of neutrino oscillations in matter and solar-neutrino spectroscopy*, *Nuovo Cimento C* **9** (Feb., 1986) 17–26.
- [12] MINOS collaboration, P. Adamson et al., *Measurement of neutrino and antineutrino oscillations using beam and atmospheric data in minos*, *Phys.Rev.Lett.* **110** (2013) 251801, [[1304.6335](https://arxiv.org/abs/1304.6335)].
- [13] SUPER-KAMIOKANDE collaboration, Y. Fukuda et al., *Evidence for oscillation of atmospheric neutrinos*, *Phys.Rev.Lett.* **81** (1998) 1562–1567, [[hep-ex/9807003](https://arxiv.org/abs/hep-ex/9807003)].

- [14] LBNE collaboration, C. Adams et al., *The Long-Baseline Neutrino Experiment: Exploring Fundamental Symmetries of the Universe*, 2013, arXiv:1307.7335, <http://www.osti.gov/scitech/biblio/1128102>.
- [15] R. Davis, D. S. Harmer and K. C. Hoffman, *Search for neutrinos from the sun*, *Phys. Rev. Lett.* **20** (May, 1968) 1205–1209.
- [16] K. S. Hirata, T. Kajita, T. Kifune, K. Kihara, M. Nakahata, K. Nakamura et al., *Observation of  $^8\text{B}$  solar neutrinos in the kamiokande-ii detector*, *Phys. Rev. Lett.* **63** (Jul, 1989) 16–19.
- [17] P. Anselmann, W. Hampel, G. Heusser, J. Kiko, T. Kirsten, E. Pernicka et al., *Solar neutrinos observed by gallex at gran sasso*, *Physics Letters B* **285** (1992) 376–389.
- [18] SNO collaboration, Q. R. Ahmad et al., *Measurement of the rate of  $\nu_e + d \rightarrow p + p + e^-$  interactions produced by  $^8\text{B}$  solar neutrinos at the Sudbury Neutrino Observatory*, *Phys. Rev. Lett.* **87** (2001) 071301, [nucl-ex/0106015].
- [19] SNO collaboration, Q. R. Ahmad et al., *Direct evidence for neutrino flavor transformation from neutral current interactions in the Sudbury Neutrino Observatory*, *Phys. Rev. Lett.* **89** (2002) 011301, [nucl-ex/0204008].
- [20] LSND collaboration, A. Aguilar-Arevalo et al., *Evidence for neutrino oscillations from the observation of anti-neutrino(electron) appearance in a anti-neutrino(muon) beam*, *Phys. Rev.* **D64** (2001) 112007, [hep-ex/0104049].
- [21] DOUBLE-CHOOZ collaboration, Y. Abe et al., *Indication for the disappearance of reactor electron antineutrinos in the Double Chooz experiment*, *Phys.Rev.Lett.* **108** (2012) 131801, [1112.6353].
- [22] DAYA BAY collaboration, F. P. An et al., *Observation of electron-antineutrino disappearance at daya bay*, *Phys. Rev. Lett.* **108** (2012) 171803, [1203.1669].
- [23] RENO collaboration, S.-B. Kim et al., *Observation of reactor electron antineutrino disappearance in the reno experiment*, *Phys. Rev. Lett.* **108** (2012) 191802, [1204.0626].
- [24] S. L. Glashow, *Partial symmetries of weak interactions*, *Nucl. Phys.* **22** (1961) 579–588.
- [25] S. Weinberg, *A model of leptons*, *Phys. Rev. Lett.* **19** (1967) 1264–1266.
- [26] A. Salam, *Elementary particle theory, relativistic groups and analyticity*, *Proc. of the 8th Nobel Symposium* (1969) .
- [27] PARTICLE DATA GROUP collaboration, P. Zyla et al., *Review of Particle Physics*, *PTEP* **2020** (2020) 083C01.

- [28] *The standard model of elementary particles*, Available at [https://en.wikipedia.org/wiki/File:Standard\\_Model\\_of\\_Elementary\\_Particles.svg#file](https://en.wikipedia.org/wiki/File:Standard_Model_of_Elementary_Particles.svg#file).
- [29] F. Englert and R. Brout, *Broken symmetry and the mass of gauge vector mesons*, *Phys. Rev. Lett.* **13** (Aug, 1964) 321–323.
- [30] P. W. Higgs, *Broken symmetries and the masses of gauge bosons*, *Phys. Rev. Lett.* **13** (Oct, 1964) 508–509.
- [31] G. S. Guralnik, C. R. Hagen and T. W. B. Kibble, *Global conservation laws and massless particles*, *Phys. Rev. Lett.* **13** (Nov, 1964) 585–587.
- [32] S. Eliezer and A. R. Swift, *Experimental consequences of  $\nu_e - \nu_\mu$  mixing in neutrino beams*, *Nuclear Physics B* **105** (1976) 45–51.
- [33] H. Fritsch and P. Minkowski, *Vectorlike weak currents, massive neutrinos, and neutrino beam oscillations*, *Physics Letters B* **62** (1976) 72–76.
- [34] S. Bilenky and B. Pontecorvo, *Lepton mixing and neutrino oscillations*, *Physics Reports* **41** (1978) 225–261.
- [35] S. Eidelman et al., *Review of particle physics*, *Physics Letters B* **592** (2004) 1–5.
- [36] SUPER-KAMIOKANDE collaboration, J. Hosaka et al., *Solar neutrino measurements in Super-Kamiokande-I*, *Phys. Rev. D* **73** (2006) 112001, [hep-ex/0508053].
- [37] SUPER-KAMIOKANDE collaboration, J. Cravens et al., *Solar neutrino measurements in Super-Kamiokande-II*, *Phys. Rev. D* **78** (2008) 032002, [0803.4312].
- [38] SUPER-KAMIOKANDE collaboration, K. Abe et al., *Solar neutrino results in Super-Kamiokande-III*, *Phys. Rev. D* **83** (2011) 052010, [1010.0118].
- [39] SNO collaboration, B. Aharmim et al., *Combined Analysis of all Three Phases of Solar Neutrino Data from the Sudbury Neutrino Observatory*, *Phys. Rev. C* **88** (2013) 025501, [1109.0763].
- [40] BOREXINO collaboration, G. Bellini et al., *Measurement of the solar  $8B$  neutrino rate with a liquid scintillator target and 3 MeV energy threshold in the Borexino detector*, *Phys. Rev. D* **82** (2010) 033006, [0808.2868].
- [41] G. Bellini et al., *Precision measurement of the  $7Be$  solar neutrino interaction rate in Borexino*, *Phys. Rev. Lett.* **107** (2011) 141302, [1104.1816].
- [42] BOREXINO collaboration, G. Bellini et al., *Neutrinos from the primary proton–proton fusion process in the sun*, *Nature* **512** (2014) .

- [43] SUPER-KAMIOKANDE collaboration, K. Abe et al., *Solar neutrino measurements in super-kamiokande-iv*, *Phys. Rev. D* **94** (Sep, 2016) 052010.
- [44] KAMLAND collaboration, A. Gando et al., *Reactor on-off antineutrino measurement with kamland*, *Phys. Rev. D* **88** (Aug, 2013) 033001.
- [45] I. Esteban, M. C. Gonzalez-Garcia, M. Maltoni, T. Schwetz and A. Zhou, *The fate of hints: updated global analysis of three-flavor neutrino oscillations*, *JHEP* **09** (2020) 178, [2007.14792].
- [46] DAYA BAY collaboration, D. Adey et al., *Measurement of the Electron Antineutrino Oscillation with 1958 Days of Operation at Daya Bay*, *Phys. Rev. Lett.* **121** (2018) 241805, [1809.02261].
- [47] DOUBLE CHOOZ collaboration, Y. Abe et al., *Measurement of  $\theta_{13}$  in Double Chooz using neutron captures on hydrogen with novel background rejection techniques*, *JHEP* **01** (2016) 163, [1510.08937].
- [48] RENO collaboration, G. Bak et al., *Measurement of reactor antineutrino oscillation amplitude and frequency at reno*, *Phys. Rev. Lett.* **121** (Nov, 2018) 201801.
- [49] X. Qian and P. Vogel, *Neutrino Mass Hierarchy*, *Prog. Part. Nucl. Phys.* **83** (2015) 1–30, [1505.01891].
- [50] ICECUBE collaboration, M. G. Aartsen et al., *Measurement of atmospheric neutrino oscillations at 6–56 gev with icecube deepcore*, *Phys. Rev. Lett.* **120** (Feb, 2018) 071801.
- [51] SUPER-KAMIOKANDE collaboration, K. Abe et al., *Atmospheric neutrino oscillation analysis with external constraints in super-kamiokande i-iv*, *Phys. Rev. D* **97** (Apr, 2018) 072001.
- [52] NOVA collaboration, M. A. Acero et al., *First measurement of neutrino oscillation parameters using neutrinos and antineutrinos by nova*, *Phys. Rev. Lett.* **123** (Oct, 2019) 151803.
- [53] T2K collaboration, K. Abe et al., *Search for  $cp$  violation in neutrino and antineutrino oscillations by the  $t2k$  experiment with  $2.2 \times 10^{21}$  protons on target*, *Phys. Rev. Lett.* **121** (Oct, 2018) 171802.
- [54] MINOS collaboration, P. Adamson et al., *Study of muon neutrino disappearance using the fermilab main injector neutrino beam*, *Phys. Rev. D* **77** (Apr, 2008) 072002.
- [55] MINOS collaboration, P. Adamson et al., *Measurement of neutrino oscillations with the minos detectors in the numi beam*, *Phys. Rev. Lett.* **101** (Sep, 2008) 131802.

- [56] DUNE collaboration, B. Abi et al., *Long-baseline neutrino oscillation physics potential of the DUNE experiment*, *Eur. Phys. J. C* **80** (2020) 978, [2006.16043].
- [57] HYPER-KAMIOKANDE collaboration, K. Abe et al., *Hyper-Kamiokande Design Report*, 1805.04163.
- [58] PARTICLE DATA GROUP collaboration, M. Tanabashi et al., *Review of particle physics*, *Phys. Rev. D* **98** (Aug, 2018) 030001.
- [59] MINIBOONE collaboration, A. A. Aguilar-Arevalo et al., *A Search for Electron Neutrino Appearance at the  $\Delta m^2 \sim 1\text{eV}^2$  Scale*, *Phys. Rev. Lett.* **98** (2007) 231801, [0704.1500].
- [60] MINIBOONE collaboration, A. A. Aguilar-Arevalo et al., *Event Excess in the MiniBooNE Search for  $\bar{\nu}_\mu \rightarrow \bar{\nu}_e$  Oscillations*, *Phys. Rev. Lett.* **105** (2010) 181801, [1007.1150].
- [61] MINIBOONE collaboration, A. A. Aguilar-Arevalo et al., *Significant Excess of ElectronLike Events in the MiniBooNE Short-Baseline Neutrino Experiment*, *Phys. Rev. Lett.* **121** (2018) 221801, [1805.12028].
- [62] F. Kaether, W. Hampel, G. Heusser, J. Kiko and T. Kirsten, *Reanalysis of the GALLEX solar neutrino flux and source experiments*, *Phys. Lett. B* **685** (2010) 47–54, [1001.2731].
- [63] W. Hampel et al., *Gallex solar neutrino observations: Results for gallex iii*, *Physics Letters B* **388** (1996) 384–396.
- [64] GALLEX collaboration, W. Hampel et al., *Final results of the Cr-51 neutrino source experiments in GALLEX*, *Phys. Lett. B* **420** (1998) 114–126.
- [65] SAGE collaboration, J. N. Abdurashitov et al., *Measurement of the solar neutrino capture rate with gallium metal. III: Results for the 2002–2007 data-taking period*, *Phys. Rev. C* **80** (2009) 015807, [0901.2200].
- [66] SAGE collaboration, J. N. Abdurashitov et al., *Measurement of the response of a Ga solar neutrino experiment to neutrinos from an Ar-37 source*, *Phys. Rev. C* **73** (2006) 045805, [nucl-ex/0512041].
- [67] SAGE collaboration, J. N. Abdurashitov et al., *Measurement of the response of the Russian-American gallium experiment to neutrinos from a Cr-51 source*, *Phys. Rev. C* **59** (1999) 2246–2263, [hep-ph/9803418].
- [68] J. N. Abdurashitov et al., *The russian-american gallium experiment (sage) cr neutrino source measurement*, *Phys. Rev. Lett.* **77** (Dec, 1996) 4708–4711.
- [69] J. Kostensalo, J. Suhonen, C. Giunti and P. C. Srivastava, *The gallium anomaly revisited*, *Phys. Lett. B* **795** (2019) 542–547, [1906.10980].
- [70] K. N. Abazajian et al., *Light Sterile Neutrinos: A White Paper*, 1204.5379.

- [71] H. Kwon, F. Boehm, A. A. Hahn, H. E. Henrikson, J. L. Vuilleumier, J. F. Cavaignac et al., *Search for neutrino oscillations at a fission reactor*, *Phys. Rev. D* **24** (Sep, 1981) 1097–1111.
- [72] G. Zacek, F. v. Feilitzsch, R. L. Mössbauer, L. Oberauer, V. Zacek, F. Boehm et al., *Neutrino-oscillation experiments at the gösgen nuclear power reactor*, *Phys. Rev. D* **34** (Nov, 1986) 2621–2636.
- [73] G. Vidyakin, V. Vyrodov, I. Gurevich, Y. Kozlov, V. Martemyanov, S. Sukhotin et al., *Detection of Anti-neutrinos in the Flux From Two Reactors*, *Sov. Phys. JETP* **66** (1987) 243–247.
- [74] G. Vidyakin et al., *Limitations on the characteristics of neutrino oscillations*, *JETP Lett.* **59** (1994) 390–393.
- [75] Y. Kozlov, S. Khalturstsev, I. Machulin, A. Martemyanov, V. Martemyanov, A. Sabelnikov et al., *Today and future neutrino experiments at krasnoyarsk nuclear reactor*, *Nuclear Physics B - Proceedings Supplements* **87** (2000) 514 – 516.
- [76] A. Afonin, S. Ketov, V. Kopeikin, L. Mikaelyan, M. Skorokhvatov and S. Tolokonnikov, *A Study of the Reaction  $\bar{\nu}_e + P \rightarrow e^+ + N$  on a Nuclear Reactor*, *Sov. Phys. JETP* **67** (1988) 213–221.
- [77] A. Kuvshinnikov, L. Mikaelyan, S. Nikolaev, M. Skorokhvatov and A. Etenko, *Measuring the  $\bar{\nu}_e + p^+ \rightarrow n + e^+$  cross-section and beta decay axial constant in a new experiment at Rovno NPP reactor. (In Russian)*, *JETP Lett.* **54** (1991) 253–257.
- [78] B. Achkar, R. Aleksan, M. Avenier, G. Bagieu, J. Bouchez, R. Brissot et al., *Search for neutrino oscillations at 15, 40 and 95 meters from a nuclear power reactor at bugey*, *Nuclear Physics B* **434** (1995) 503 – 532.
- [79] Y. Declais, H. de Kerret, B. Lefièvre, M. Obolensky, A. Etenko, Y. Kozlov et al., *Study of reactor antineutrino interaction with proton at bugey nuclear power plant*, *Physics Letters B* **338** (1994) 383 – 389.
- [80] Z. D. Greenwood, W. R. Kropp, M. A. Mandelkern, S. Nakamura, E. L. Pasierb-Love, L. R. Price et al., *Results of a two-position reactor neutrino-oscillation experiment*, *Phys. Rev. D* **53** (Jun, 1996) 6054–6064.
- [81] NEOS collaboration, Y. Ko et al., *Sterile Neutrino Search at the NEOS Experiment*, *Phys. Rev. Lett.* **118** (2017) 121802, [1610.05134].
- [82] DANSS collaboration, I. Alekseev et al., *Search for sterile neutrinos at the DANSS experiment*, *Phys. Lett. B* **787** (2018) 56–63, [1804.04046].
- [83] G. Mention, M. Fechner, T. Lasserre, T. Mueller, D. Lhuillier, M. Cribier et al., *The Reactor Antineutrino Anomaly*, *Phys. Rev. D* **83** (2011) 073006, [1101.2755].

- [84] ALEPH collaboration, D. Buskulic et al., *A Direct measurement of the invisible width of the Z from single photon counting*, *Phys. Lett. B* **313** (1993) 520–534.
- [85] S. Gariazzo, C. Giunti, M. Laveder and Y. F. Li, *Updated Global 3+1 Analysis of Short-BaseLine Neutrino Oscillations*, *JHEP* **06** (2017) 135, [1703.00860].
- [86] MINOS+ collaboration, P. Adamson et al., *Search for sterile neutrinos in MINOS and MINOS+ using a two-detector fit*, *Phys. Rev. Lett.* **122** (2019) 091803, [1710.06488].
- [87] ICECUBE collaboration, M. G. Aartsen et al., *Searching for eV-scale sterile neutrinos with eight years of atmospheric neutrinos at the IceCube Neutrino Telescope*, *Phys. Rev. D* **102** (2020) 052009, [2005.12943].
- [88] SUPER-KAMIOKANDE collaboration, R. Wendell et al., *Atmospheric neutrino oscillation analysis with sub-leading effects in Super-Kamiokande I, II, and III*, *Phys. Rev. D* **81** (2010) 092004, [1002.3471].
- [89] SUPER-KAMIOKANDE collaboration, R. Wendell, *Atmospheric Results from Super-Kamiokande*, *AIP Conf. Proc.* **1666** (2015) 100001, [1412.5234].
- [90] M. Dentler, A. Hernández-Cabezudo, J. Kopp, P. A. N. Machado, M. Maltoni, I. Martinez-Soler et al., *Updated Global Analysis of Neutrino Oscillations in the Presence of eV-Scale Sterile Neutrinos*, *JHEP* **08** (2018) 010, [1803.10661].
- [91] G. V. Stenico, D. V. Forero and O. L. G. Peres, *A Short Travel for Neutrinos in Large Extra Dimensions*, *JHEP* **11** (2018) 155, [1808.05450].
- [92] N. Arkani-Hamed, S. Dimopoulos and G. R. Dvali, *The Hierarchy problem and new dimensions at a millimeter*, *Phys. Lett.* **B429** (1998) 263–272, [arXiv:hep-ph/9803315].
- [93] N. Arkani-Hamed, S. Dimopoulos and G. R. Dvali, *Phenomenology, astrophysics and cosmology of theories with submillimeter dimensions and TeV scale quantum gravity*, *Phys. Rev.* **D59** (1999) 086004, [arXiv:hep-ph/9807344].
- [94] H. Murayama, <http://hitoshi.berkeley.edu/>, access in 05/04/2017, .
- [95] N. Arkani-Hamed, S. Dimopoulos, G. R. Dvali and J. March-Russell, *Neutrino masses from large extra dimensions*, *Phys. Rev.* **D65** (2002) 024032, [arXiv:hep-ph/9811448].
- [96] K. R. Dienes, E. Dudas and T. Gherghetta, *Neutrino oscillations without neutrino masses or heavy mass scales: A Higher dimensional seesaw mechanism*, *Nucl. Phys.* **B557** (1999) 25, [arXiv:hep-ph/9811428].
- [97] G. R. Dvali and A. Yu. Smirnov, *Probing large extra dimensions with neutrinos*, *Nucl. Phys.* **B563** (1999) 63–81, [arXiv:hep-ph/9904211].

- [98] R. Barbieri, P. Creminelli and A. Strumia, *Neutrino oscillations from large extra dimensions*, *Nucl. Phys.* **B585** (2000) 28–44, [arXiv:hep-ph/0002199].
- [99] H. Davoudiasl, P. Langacker and M. Perelstein, *Constraints on large extra dimensions from neutrino oscillation experiments*, *Phys. Rev.* **D65** (2002) 105015, [arXiv:hep-ph/0201128].
- [100] R. N. Mohapatra, S. Nandi and A. Perez-Lorenzana, *Neutrino masses and oscillations in models with large extra dimensions*, *Phys. Lett.* **B466** (1999) 115–121, [arXiv:hep-ph/9907520].
- [101] P. A. N. Machado, H. Nunokawa and R. Zukanovich Funchal, *Testing for Large Extra Dimensions with Neutrino Oscillations*, *Phys. Rev.* **D84** (2011) 013003, [1101.0003].
- [102] P. A. N. Machado, H. Nunokawa, F. A. P. dos Santos and R. Z. Funchal, *Bulk Neutrinos as an Alternative Cause of the Gallium and Reactor Anti-neutrino Anomalies*, *Phys. Rev.* **D85** (2012) 073012, [arXiv:1107.2400].
- [103] V. S. Basto-Gonzalez, A. Esmaili and O. L. G. Peres, *Kinematical Test of Large Extra Dimension in Beta Decay Experiments*, *Phys. Lett.* **B718** (2013) 1020–1023, [1205.6212].
- [104] A. Esmaili, O. L. G. Peres and Z. Tabrizi, *Probing Large Extra Dimensions With IceCube*, *JCAP* **1412** (2014) 002, [1409.3502].
- [105] A. Di Iura, I. Girardi and D. Meloni, *Probing new physics scenarios in accelerator and reactor neutrino experiments*, *J. Phys.* **G42** (2015) 065003, [arXiv:1411.5330].
- [106] J. M. Berryman, A. de Gouvêa, K. J. Kelly, O. L. G. Peres and Z. Tabrizi, *Large Extra Dimensions at the Deep Underground Neutrino Experiment*, *Phys. Rev.* **D94** (2016) 033006, [1603.00018].
- [107] MINOS collaboration, P. Adamson et al., *Constraints on Large Extra Dimensions from the MINOS Experiment*, *Phys. Rev.* **D94** (2016) 111101, [1608.06964].
- [108] I. Esteban, M. C. Gonzalez-Garcia, M. Maltoni, I. Martinez-Soler and T. Schwetz, *Updated fit to three neutrino mixing: exploring the accelerator-reactor complementarity*, *JHEP* **01** (2017) 087, [1611.01514].
- [109] I. Esteban, M. C. Gonzalez-Garcia, M. Maltoni, I. Martinez-Soler and T. Schwetz, *NuFIT*, <http://www.nu-fit.org/>.
- [110] P. F. de Salas, D. V. Forero, C. A. Ternes, M. Tortola and J. W. F. Valle, *Status of neutrino oscillations 2018:  $3\sigma$  hint for normal mass ordering and improved CP sensitivity*, *Phys. Lett.* **B782** (2018) 633–640, [1708.01186].

- [111] MICROBOONE, LAR1-ND, ICARUS-WA104 collaboration, M. Antonello et al., *A Proposal for a Three Detector Short-Baseline Neutrino Oscillation Program in the Fermilab Booster Neutrino Beam*, 1503.01520.
- [112] P. Huber, M. Lindner and W. Winter, *Simulation of long-baseline neutrino oscillation experiments with GLoBES (General Long Baseline Experiment Simulator)*, *Comput. Phys. Commun.* **167** (2005) 195, [hep-ph/0407333].
- [113] P. Huber, J. Kopp, M. Lindner, M. Rolinec and W. Winter, *New features in the simulation of neutrino oscillation experiments with GLoBES 3.0: General Long Baseline Experiment Simulator*, *Comput. Phys. Commun.* **177** (2007) 432–438, [hep-ph/0701187].
- [114] C. Adams et al., “LAR1-ND: Testing Neutrino Anomalies with Multiple LAr TPC Detectors at Fermilab.” <https://www.osti.gov/biblio/1156551/>, 2013. doi:10.2172/1156551.
- [115] DUNE collaboration, R. Acciarri et al., *Long-Baseline Neutrino Facility (LBNF) and Deep Underground Neutrino Experiment (DUNE)*, 1512.06148.
- [116] C. Andreopoulos et al., *The GENIE Neutrino Monte Carlo Generator*, *Nucl. Instrum. Meth.* **A614** (2010) 87–104, [0905.2517].
- [117] D. Cianci, A. Furmanski, G. Karagiorgi and M. Ross-Lonergan, *Prospects of Light Sterile Neutrino Oscillation and CP Violation Searches at the Fermilab Short Baseline Neutrino Facility*, *Phys. Rev.* **D96** (2017) 055001, [1702.01758].
- [118] J. M. Conrad and M. H. Shaevitz, *Sterile Neutrinos: An Introduction to Experiments*, *Adv. Ser. Direct. High Energy Phys.* **28** (2018) 391–442, [1609.07803].
- [119] O. L. G. Peres and A. Yu. Smirnov, *(3+1) spectrum of neutrino masses: A Chance for LSND?*, *Nucl. Phys.* **B599** (2001) 3, [hep-ph/0011054].
- [120] MINIBOONE collaboration, A. A. Aguilar-Arevalo et al., *Updated MiniBooNE Neutrino Oscillation Results with Increased Data and New Background Studies*, 2006.16883.
- [121] M. Carena, Y.-Y. Li, C. S. Machado, P. A. N. Machado and C. E. M. Wagner, *Neutrinos in Large Extra Dimensions and Short-Baseline  $\nu_e$  Appearance*, *Phys. Rev.* **D96** (2017) 095014, [1708.09548].
- [122] G. V. Stenico, “AEDL files for SBN to be used in GLOBES software, available under request.” Contact: gstenico@ifi.unicamp.br.
- [123] G. H. Collin, C. A. Argüelles, J. M. Conrad and M. H. Shaevitz, *First Constraints on the Complete Neutrino Mixing Matrix with a Sterile Neutrino*, *Phys. Rev. Lett.* **117** (2016) 221801, [1607.00011].

- [124] S. Böser, C. Buck, C. Giunti, J. Lesgourgues, L. Ludhova, S. Mertens et al., *Status of Light Sterile Neutrino Searches*, *Prog. Part. Nucl. Phys.* **111** (2020) 103736, [1906.01739].
- [125] A. Diaz, C. A. Argüelles, G. H. Collin, J. M. Conrad and M. H. Shaevitz, *Where Are We With Light Sterile Neutrinos?*, *Phys. Rept.* **884** (2020) 1–59, [1906.00045].
- [126] A. de Gouvêa, O. L. G. Peres, S. Prakash and G. V. Stenico, *On The Decaying-Sterile Neutrino Solution to the Electron (Anti)Neutrino Appearance Anomalies*, *JHEP* **07** (2020) 141, [1911.01447].
- [127] S. Palomares-Ruiz, S. Pascoli and T. Schwetz, *Explaining LSND by a decaying sterile neutrino*, *JHEP* **09** (2005) 048, [hep-ph/0505216].
- [128] S. M. Bilenky and S. T. Petcov, *Massive neutrinos and neutrino oscillations*, *Rev. Mod. Phys.* **59** (Jul, 1987) 671–754.
- [129] D. J. Griffiths, *Introduction to elementary particles; 2nd rev. version*. Physics textbook. Wiley, New York, NY, 2008.
- [130] A. de Gouvêa and A. Kobach, *Global Constraints on a Heavy Neutrino*, *Phys. Rev.* **D93** (2016) 033005, [1511.00683].
- [131] D. A. Bryman and R. Shrock, *Constraints on Sterile Neutrinos in the MeV to GeV Mass Range*, *Phys. Rev.* **D100** (2019) 073011, [1909.11198].
- [132] P. S. Pasquini and O. L. G. Peres, *Bounds on Neutrino-Scalar Yukawa Coupling*, *Phys. Rev.* **D93** (2016) 053007, [arXiv:1511.01811].
- [133] LSND collaboration, C. Athanassopoulos et al., *The Liquid scintillator neutrino detector and LAMPF neutrino source*, *Nucl. Instrum. Meth. A* **388** (1997) 149–172, [nucl-ex/9605002].
- [134] A. Strumia and F. Vissani, *Precise quasielastic neutrino/nucleon cross-section*, *Phys. Lett.* **B564** (2003) 42–54, [astro-ph/0302055].
- [135] MINIBOONE collaboration, A. A. Aguilar-Arevalo et al., *The MiniBooNE Detector*, *Nucl. Instrum. Meth.* **A599** (2009) 28–46, [0806.4201].
- [136] MINIBOONE collaboration, A. A. Aguilar-Arevalo et al., *A Search for muon neutrino and antineutrino disappearance in MiniBooNE*, *Phys. Rev. Lett.* **103** (2009) 061802, [0903.2465].
- [137] MINIBOONE collaboration, A. A. Aguilar-Arevalo et al., *A Search for Electron Antineutrino Appearance at the  $\Delta m^2 \sim 1 \text{ eV}^2$  Scale*, *Phys. Rev. Lett.* **103** (2009) 111801, [0904.1958].
- [138] MINIBOONE collaboration, A. A. Aguilar-Arevalo et al., *A Combined  $\nu_\mu \rightarrow \nu_e$  and  $\bar{\nu}_\mu \rightarrow \bar{\nu}_e$  Oscillation Analysis of the MiniBooNE Excesses*, 1207.4809.

- [139] MiniBooNE, “Data release for 1805.12028.”  
[https://www-boone.fnal.gov/for\\_physicists/data\\_release/nue2018/](https://www-boone.fnal.gov/for_physicists/data_release/nue2018/).
- [140] MINIBOONE collaboration, A. A. Aguilar-Arevalo et al., *The Neutrino Flux prediction at MiniBooNE*, *Phys. Rev. D* **79** (2009) 072002, [0806.1449].
- [141] MiniBooNE, “Data release for 1207.4809.”  
[https://www-boone.fnal.gov/for\\_physicists/data\\_release/nue\\_nuebar\\_2012/efficiency/MB\\_nu\\_nubar\\_combined\\_release.html](https://www-boone.fnal.gov/for_physicists/data_release/nue_nuebar_2012/efficiency/MB_nu_nubar_combined_release.html).
- [142] G. S. Karagiorgi, “Searches for New Physics at MiniBooNE: Sterile Neutrinos and Mixing Freedom.” <https://www.osti.gov/biblio/1000269>, 2010.  
 doi:10.2172/1000269.
- [143] J. Kopp, P. A. N. Machado, M. Maltoni and T. Schwetz, *Sterile Neutrino Oscillations: The Global Picture*, *JHEP* **05** (2013) 050, [1303.3011].
- [144] KARMEN collaboration, B. Armbruster et al., *Upper limits for neutrino oscillations  $\bar{\nu}_\mu \rightarrow \bar{\nu}_e$  from muon decay at rest*, *Phys. Rev. D* **65** (2002) 112001, [hep-ex/0203021].
- [145] MINOS collaboration, I. Ambats et al., “The MINOS Detectors Technical Design Report.”  
<http://lss.fnal.gov/archive/design/fermilab-design-1998-02.pdf>, 1998.
- [146] K. Anderson et al., “The NuMI Facility Technical Design Report.”  
[http://lss.fnal.gov/cgi-bin/find\\_paper.pl?design-1998-01.pdf](http://lss.fnal.gov/cgi-bin/find_paper.pl?design-1998-01.pdf), 1998.  
 10.2172/1156372.
- [147] MINOS collaboration, P. Adamson et al., *Combined analysis of  $\nu_\mu$  disappearance and  $\nu_\mu \rightarrow \nu_e$  appearance in MINOS using accelerator and atmospheric neutrinos*, *Phys. Rev. Lett.* **112** (2014) 191801, [1403.0867].
- [148] O. Fischer, A. Hernández-Cabezudo and T. Schwetz, *Explaining the miniboone excess by a decaying sterile neutrino with mass in the 250 mev range*, *Phys. Rev. D* **101** (2020) 075045, [1909.09561].
- [149] M. Moulai, C. Argüelles, G. Collin, J. Conrad, A. Diaz and M. Shaevitz, *Combining Sterile Neutrino Fits to Short Baseline Data with IceCube Data*, *Phys. Rev. D* **101** (2020) 055020, [1910.13456].
- [150] M. Dentler, I. Esteban, J. Kopp and P. Machado, *Decaying Sterile Neutrinos and the Short Baseline Oscillation Anomalies*, *Phys. Rev. D* **101** (2020) 115013, [1911.01427].